Analysis of Coarsening of Complex Structures

by

Chal-Lan Park

A dissertation submitted in partial fulfillment
of the requirements for the degree of
Doctor of Philosophy
(Materials Science and Engineering)
in The University of Michigan
2016

Doctoral Committee:

Professor Katsuyo Thornton, Chair
Professor Peter W. Voorhees, Northwestern University
Assistant Professor Liang Qi
Professor Robert Ziff

To My Savior Lord Jesus Christ

ACKNOWLEDGEMENTS

First and foremost, I would like to thank Professor Thornton for her continuous support and guidance throughout my academic endeavor. I am always grateful to her for introducing me to the field of computational materials science and training me to become a better scientist. Most importantly, I am deeply thankful of her unconditional support during the unforeseen military service that interrupted my graduate study for 21 months. I am very fortunate to have worked with Professor Thornton. I would also like to thank Professor Voorhees for his words of encouragement and invaluable feedback during our collaborative work over many years. In addition, I would like to thank Professor Ziff and Professor Qi for agreeing to serve on my committee and providing me with valuable advise.

I would also like to thank all of the past and present lab mates (Hui-Chia, Hsun-Yi, Nirand, Chloe, Nick, Victor, Steve, Larry, Bernardo, Andrea, Susan, Susanta, Candace, Alex, Beck, Jason, Min-Ju, Erik, Saeed, David, Raul, Roy) who have made this long journey more enjoyable. I would like to personally thank Hui-Chia and Victor for their helping hands and friendship over many years. I am also very grateful to my English tutor, Professor Hildinger, who has helped me tremendously with my thesis. I thoroughly enjoyed all of our editing sessions.

I would not have come this far without the love and sacrifice from my parents and grandparents. Their prayers have always guided me to the right path and I am always thankful to God for all of His blessings.

TABLE OF CONTENTS

LIST OF FIGURES

Figure

LIST OF TABLES

Table

LIST OF APPENDICES

Appendix

ABSTRACT

Analysis of Coarsening of Complex Structures

by

Chal-Lan Park

Chair: Katsuyo Thornton

Coarsening is an ubiquitous phenomenon that alters the microstructure of the material and its properties. While coarsening of spherical particles has been extensively studied over the last half century, the understanding of coarsening of complex microstructures is still at an early stage. The complex morphology and topology pose difficulty in establishing a theory of coarsening of such microstructures. In an effort to elucidate the dynamics of coarsening, we examine the morphological evolution of bicontinuous structures simulated using the phase-field method. To improve the accuracy of the calculation of interfacial characteristics of the simulated structures, we develop a numerically efficient smoothing algorithm termed "level-set smoothing." We employ statistical analyses to uncover correlations between interfacial characteristics, such as curvatures, and their rate of changes, such as interfacial velocities and rate of change of curvatures. As the framework for the coarsening theory development, we propose to consider the evolution as a consequence of (i) the interfacial velocity induced by diffusion and (ii) the resulting evolution of the interfacial curvatures. As a first step, we examine the evolution of a bicontinuous structure simulated via nonconserved dynamics, in which the interfacial velocity is proportional to the

local mean curvature, in order to focus on the second aspect of the evolution (ii). We find that, while the interfacial velocity is locally determined, the evolution of mean curvature is nonlocal and depends on the curvatures of the nearby interfaces. As a second step, we examine the evolution of bicontinuous structures simulated via conserved dynamics to investigate both aspects of the evolution, (i) and (ii). Here, we find that the interfacial velocity is correlated with both the mean curvature and the surface Laplacian of mean curvature. Based on these correlations, we employ a semi-analytical approach to predict the average rate of change of mean curvature, which is found to be consistent with the simulation results. Lastly, in an effort to develop a theory of coarsening of complex microstructures, we derive a general continuity equation of interfacial area to predict the evolution of the overall morphology of a microstructure undergoing coarsening. Simulation of rods undergoing pinching is also conducted to provide insights into the source term arising from topological singularity.

CHAPTER I

Introduction

1.1 General Background and Motivations

Coarsening is a ubiquitous phenomenon that naturally occurs in a wide range of materials, such as metallic alloys [1, 2, 3, 4, 5, 6, 7], polymers [8, 9, 10, 11, 12, 13, 14], and semiconductors [15, 16, 17, 18, 19, 20]. During coarsening, the total interfacial area of a microstructure decreases to reduce excess free energy associated with the existence of phase boundaries. Therefore, coarsening can play a key role in determining the morphology and the topology of the microstructure of a material. Coarsening is generally preceded by phase separation, where a single-phase system transforms into a two-phase system. Regardless of whether the phase transformation is initiated by spinodal decomposition or nucleation, once the concentrations of the newly formed phases are close to their equilibrium values, the microstructure begins to coarsen [21].

The study of coarsening is important because the microstructure of a material often has a strong influence on its properties. For example, during casting of metallic alloys, solid-liquid dendritic mixtures frequently form at temperatures above the eutectic temperature. If the removal of heat is sufficiently slow, the dendrites begin to coarsen [2, 22, 23, 24, 25, 26]. The resulting evolution of the shape and size distributions of the dendrites during coarsening alters the properties of the cast alloy.

In the case of an Al-Si cast alloy, as the secondary dendritic arm spacings increase, the corrosion resistance improves and the tensile strength decreases [27, 28]. In the case of nickel/yttria-stabilized zirconia (Ni/YSZ) cermet, which is a widely used anode material in solid oxide fuel cells (SOFC), the coarsening of Ni particles in the anode reduces the density of triple-phase boundaries, thus significantly diminishing the electrochemically active regions and degrading the electrochemical performance of the SOFC over time [29, 30, 31].

Coarsening is driven by the Gibbs-Thomson effect, which describes the dependence of interfacial chemical potential on interfacial curvature. Consider a two-component (A & B) system with the matrix phase α and B-rich spherical precipitate phase β as shown in Figure 1.1a. Since the interfaces between the two phases have finite curvatures, the pressure at the curved interface will be larger than its equilibrium value based on the Young-Laplace equation

$$P_{\mathrm{r}} = P_{\infty} + 2\gamma H \ , \tag{1.1}$$

where P_{r} is the pressure at the curved interface, P_{∞} is the pressure at a flat interface, γ is the interfacial energy, and H is the interfacial mean curvature [32].

Since the Gibbs free energy is a function of pressure, the increase in pressure will result in the increase in the free energy of the precipitates. This increase in free energy is represented with the upward movement of the free energy curve of the β phase in Figure 1.1b, where G^{β}_{∞} and G^{β}_{r} are the free energy curves of the β phase at a flat interface and a curved interface, respectively, while $\Delta G^{\beta}_{\gamma}$ is the amount of increase. As depicted by the free energy diagram, this upward movement of the free energy curve shifts the equilibrium solute concentration of the matrix phase from C^{α}_{∞} to C^{α}_{r}, where C^{α}_{∞} and C^{α}_{r} are the solute concentration of the matrix phase at a flat interface and a curved interface, respectively [33]. Since the shift in the free energy is dependent

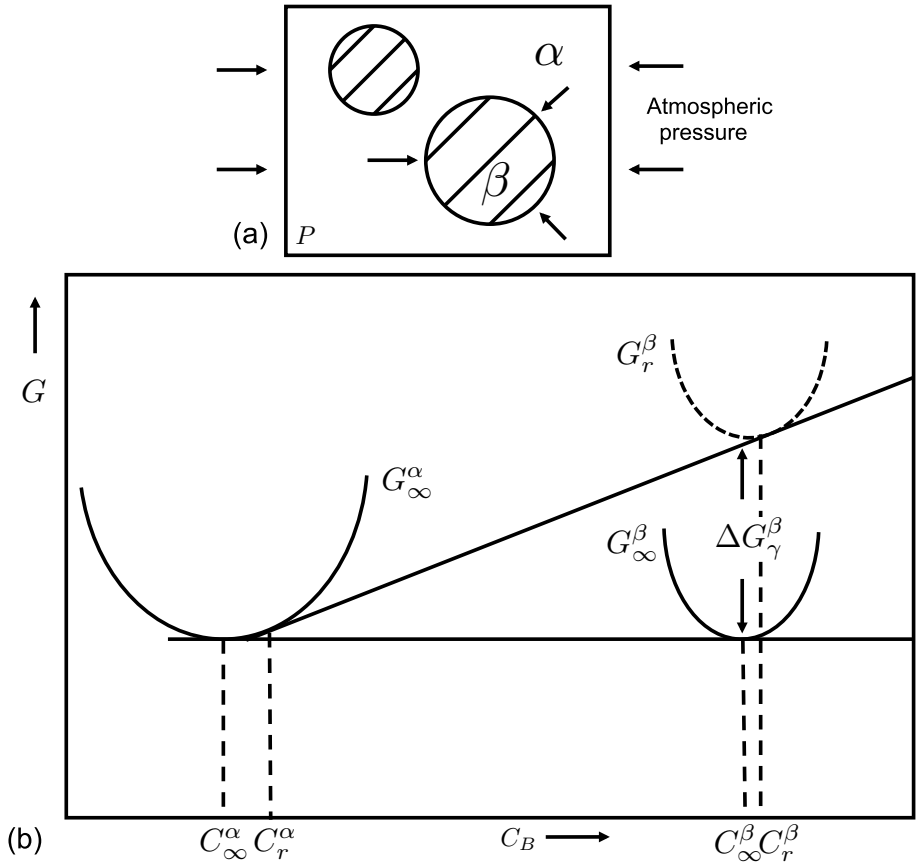

Figure 1.1: a) A schematic of the B-rich precipitate phase β embedded in the matrix phase α. b) Free energy diagram that shows the increase in the solubility of the solute in the matrix phase at the curved interface between the α matrix and the β precipitate.

on the curvature of the interface, high-curvature regions have higher concentration of solute than the low-curvature regions, as described by the Gibbs-Thomson equation,

$$C_{\mathrm{r}}^{\alpha} = C_{\infty}^{\alpha} + 2lH \ . \tag{1.2}$$

Here, the capillary length l is defined as

$$l = \frac{V_m^{\beta}\gamma}{\left(C_{\infty}^{\beta} - C_{\infty}^{\alpha}\right) G_m^{\alpha\,\prime\prime}} \ , \tag{1.3}$$

where C_{∞}^{β} and $G_m^{\alpha\,\prime\prime}$ are the equilibrium concentration of the precipitate phase and the second derivative of the molar Gibbs free energy of the matrix phase with respect to solute composition, respectively [32]. Thus, the driving force of coarsening is the solute concentration gradient, which arises from the variation of curvature along the interfaces. With this information, a theory of coarsening can be developed to elucidate how the morphology and topology of a microstructure evolves.

The simplest material system in which to develop a theory of coarsening is the spherical precipitates embedded in the matrix phase. For such systems, in the absence of interfacial misfit and other effects, the radius of a particle alone determines the interfacial chemical potential and thus interfacial concentration. As the result of the Gibbs-Thomson effect, larger particles grow at the expense of the smaller particles while the volume fraction of the particle phase remains constant. Thus, the number density of particles decreases while the average size of the particles increases, as shown in Fig. 1.2, in which the length scales of the micrographs of the solid Sn particles undergoing coarsening in the Pb-Sn liquid matrix are scaled by the average particle size.

The theory of coarsening of spherical particles has already been developed in the past. In the 1960s, Lifshitz and Slyozov [35], and Wagner [36] independently derived

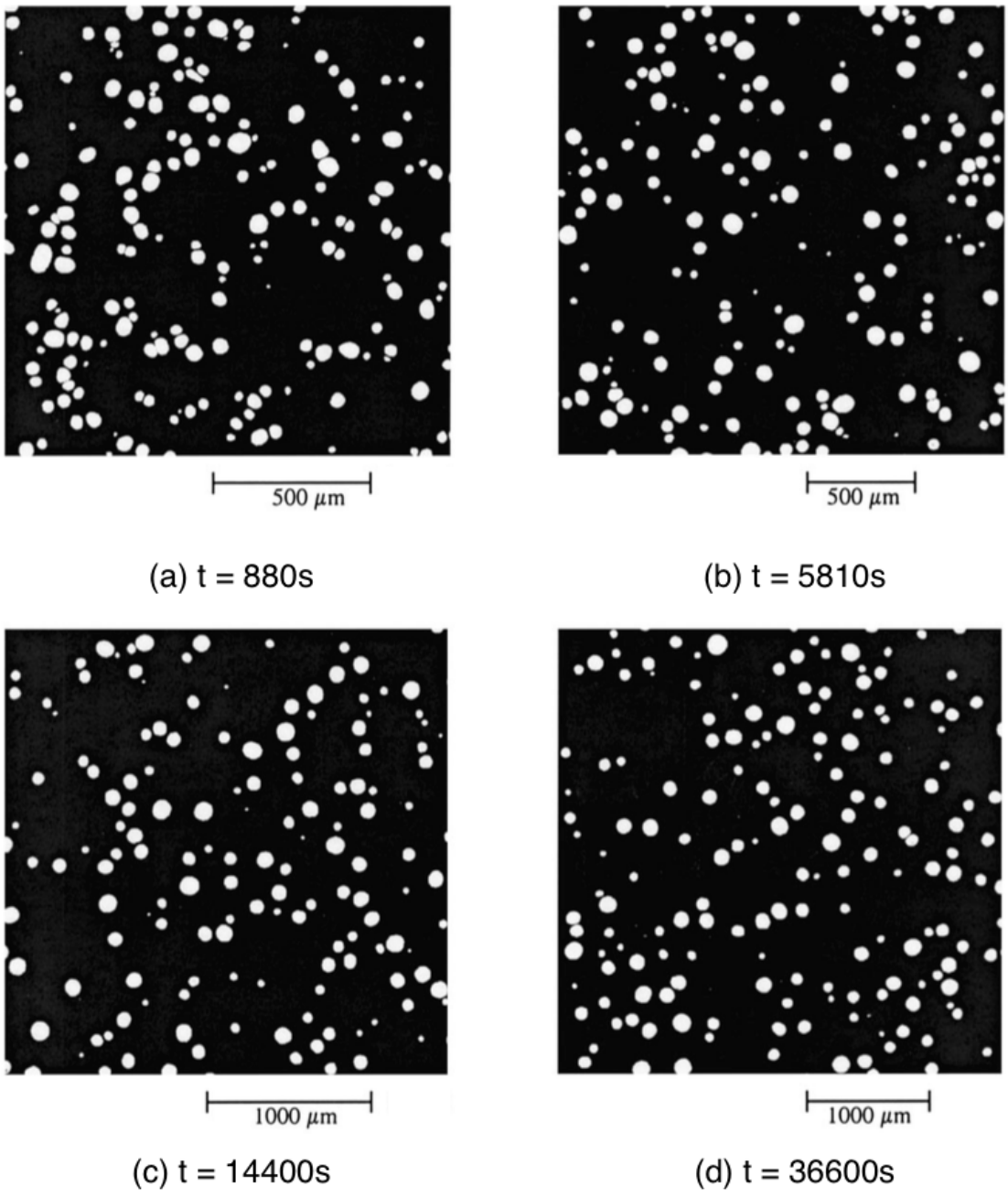

Figure 1.2: Micrographs of the solid Sn particles, shown in white, in the Pb-Sn liquid matrix, shown in black, at various coarsening times. These micrographs are scaled by the plane-section average radius at each coarsening time. Adapted with permission from [34]. Copyright 2016 by Elsevier.

an analytical theory of coarsening (now commonly referred to as the LSW theory) that describes both the local and the ensemble behavior of spherical precipitates during coarsening. Three major assumptions behind this theory are that these precipitates are spherical in geometry resulting from isotropic interfacial energy, the volume fraction of the precipitate phase is negligible (and thus the diffusion fields from individual precipitates do not overlap) and only the Gibbs-Thomson effect is considered (i.e., other effects that alter the chemical potential are neglected). In addition, it is assumed that the interfacial velocity is sufficiently small such that the concentration field remains near equilibrium (i.e., the quasi-static approximation). Thus, the concentration field of solute atoms in the matrix phase is described by the solution to the Laplace equation

$$\nabla^2 C = 0 \ , \tag{1.4}$$

with the solute concentration along the interfaces defined by Eq. (1.2) as the boundary condition. By combining the solution of Eq. (1.4) in spherical coordinates and the interfacial mass balance condition, Lifshitz, Slyozov, and Wagner derived the growth rate of a spherical particle with radius, R, in a system of particles undergoing coarsening as

$$\frac{dR}{dt} = A_0 \frac{1}{R} \left(\frac{1}{R_c} - \frac{1}{R} \right) \ , \tag{1.5}$$

where t is time, A_0 is a material parameter, and R_c is the critical radius. This growth rate indicates that particles with radii greater than R_c grow, while particles with radii smaller than R_c contract. As a result, the number of particles in the system decreases while the average particle size increases during Ostwald ripening (another terminology for coarsening). Further derivation shows R_c to be equal to $\langle R \rangle$, the average radius of particles in the system.

In addition, the LSW theory characterizes the overall morphology of the particulate system with the particle size distribution, $f(R,t)$, as a function of radius and time. The evolution of the particle size distribution is described by the continuity equation

$$\frac{\partial f}{\partial t} + \frac{\partial}{\partial R}\left(f\frac{dR}{dt}\right) = 0 \ . \tag{1.6}$$

This continuity equation does not take account discontinuous changes in particle size resulting from nucleation or coalescence. After scaling R by the time-dependent $\langle R\rangle$, the LSW theory presents the expression for the time-independent particle size distribution from the solution of Eq. (1.6), the scaled distribution is shown in Fig. 1.3. The time-independent particle size distribution implies that the particle system undergoes self-similar evolution during coarsening. Furthermore, the LSW theory predicts that this time-dependent characteristic length scale of the system, $\langle R\rangle$, obeys a temporal growth law

$$\langle R(t)\rangle^3 - \langle R(t_0)\rangle^3 = K_0 t \ , \tag{1.7}$$

where $\langle R(t_0)\rangle$ and $\langle R(t)\rangle$ are the average particle size at the onset of coarsening at time t_0 and at some following time t, respectively, and K_0 is the rate constant. Knowledge of the time-independent particle size distribution and the temporal law regarding the average particle size enables accurate prediction of the overall morphology of the microstructure during coarsening.

In contrast, the understanding of the dynamics of coarsening in materials with complex microstructures is still at an early stage. An attempt to derive the theory of coarsening based solely on an analytical approach in these materials is extremely challenging, if not impossible. This is because, unlike the simple spherical geometry used in the LSW theory, their complex morphology and topology pose difficulties in

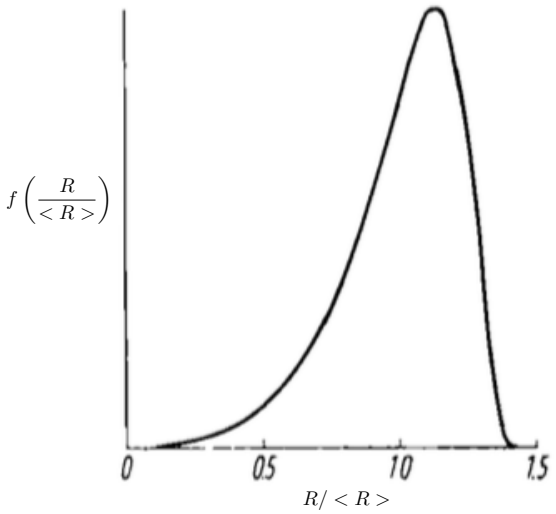

Figure 1.3: The time-independent particle size distribution $f(R/\langle R\rangle)$ of spherical particles presented in Wagner's analysis. Adapted with permission from [36]. Copyright 2016 by John Wiley and Sons.

solving the free-boundary problem of the interfacial motion. Therefore, one must rely on experimental and computational approaches to gather insights into the kinetics of interfacial motion during coarsening.

The development of theory of coarsening requires accurate quantification of the morphology. Two types of complex microstructures that are commonly found in nature are the dendritic and bicontinuous microstructures. Dendrites often form during solidification and are observed, for example, in metal castings [37]. On the other hand, bicontinuous structures, in which two phases interpenetrate one another and each is connected to itself throughout, typically form during phase decomposition such as spinodal decomposition in polymers [38, 39]. Examples of dendritic and bicontinuous structures are shown in Fig. 1.4. The spatially varying curvatures of these structures imply that the local morphology must be characterized by interfacial curvatures, rather than a length scale associated with each region (e.g., the radius of a particle for systems containing spherical particles). In contrast, the overall morphology must be statistically quantified through a distribution function defined on the

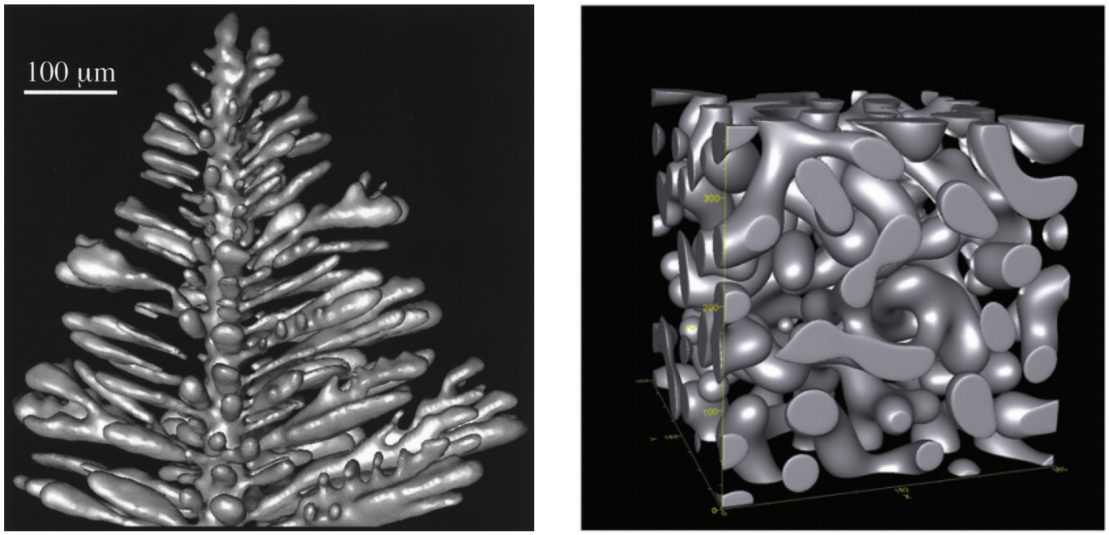

(a) **(b)**

Figure 1.4: (a) A three-dimensional reconstruction of Al dendrite in Al-15 wt.%Cu alloy. Adapted with permission from [41]. Copyright 2016 by Springer. (b) a simulated bicontinuous structure resulting from spinodal decomposition. Adapted with permission from [42]. Copyright 2016 by Taylor & Francis.

interfacial curvature space, analogous to how the overall morphology of a microstructure consisting of spherical particles is quantified by a particle size distribution as a function of radius. While the morphologies of dendritic mixtures of metallic alloys [26] and simulated bicontinuous structures [40] have been accurately quantified by interfacial curvature measurements, the development of theory of coarsening also requires understanding of the dynamics of coarsening. Thus, in this dissertation, we examine both interfacial curvatures and their rate of changes in our analysis to elucidate the complex dynamics of coarsening. *Hereafter, interfacial characteristics such as curvatures, as well as their rate of changes such as interfacial velocity and rate of change of curvatures, will be referred to as interfacial quantities.*

1.2 Overview and Outline of Dissertation

As stated above, the ultimate goal of this work is to develop the theory of coarsening of complex microstructures. This requires a simplification of the dynamics because the complex morphology and topology of the structure alone introduces complications. Therefore, we begin with a simplified mathematical description of the process, based solely on the thermodynamic driving force from interfacial free energy and excluding other effects such as elastic stress and unequal mobilities in different phases. Computational approaches can then be used to simulate the coarsening dynamics and gain insights into the process.

As the framework for the coarsening theory development, we propose to consider the evolution as a consequence of (i) the interfacial velocity induced by diffusion and (ii) the resulting evolution of the interfacial curvatures. The framework begins with the generation of microstructural data with complex morphologies and accurate quantification of interfacial quantities of the simulated structures. Based on statistical analysis, correlations between interfacial characteristics and their rate of changes are uncovered to elucidate both aspects of interfacial motion. Lastly, as in the LSW theory, a continuity equation is derived to obtain the time-independent curvature distribution that can characterize the self-similar morphology of a complex structure.

The outline of the following chapters in the dissertation is as follows:

- Chapter II discusses the interfacial curvatures and the curvature distribution that are used to quantify the interfacial morphology and the overall morphology of complex structures, respectively. In addition, a literature review on the topics of coarsening of spherical particles, dendritic microstructures, and bicontinuous structures are presented. Lastly, the chapter also contains background information of the phase-field method and the finite difference method.

- Chapter III details the development and the validation of the level-set smoothing

method, which allows accurate calculation of interfacial quantities, including both static and dynamic interfacial quantities. Numerical algorithms that can be used to calculate the aforementioned interfacial quantities are also described.

- Chapter IV examines the coarsening of a bicontinuous structure simulated via nonconserved dynamics. Examination of the evolution via nonconserved dynamics is the ideal starting point to elucidate the complex dynamics of coarsening since the kinetics is in the simplest form as it is driven by motion by mean curvature. The analysis in this chapter focuses on the second aspect of interfacial evolution, (ii) evolution of interfacial curvature given the interfacial velocity.

- Chapter V examines the coarsening of bicontinuous and nonbicontinuous structures simulated via conserved dynamics. In this chapter, we investigate the dynamics of diffusion-driven coarsening, which requires the consideration of both aspects of interfacial evolution: (i) the interfacial velocity induced by diffusion and (ii) the resulting evolution of the interfacial curvatures. In the first part of the chapter, the correlations between interfacial velocities and various static interfacial quantities are examined. In the second part, based on the aforementioned correlations, the evolution of average curvature is predicted.

- Chapter VI discusses preliminary work involving the derivation of a general continuity equation in terms of the interfacial shape distribution and the morphological evolution of a rod undergoing pinch-off, resulting in topological singularities.

- Chapter VII provides the overall summary of work, its potential application, and future work.

CHAPTER II

Background

2.1 Characterization of Morphology

The development of theory of coarsening requires accurate quantification of interfacial morphology and statistics of the overall morphology of complex microstructures. This section briefly describes the interfacial curvatures and the curvature distribution that are discussed in the subsequent literature review section and employed throughout this dissertation.

2.1.1 Interfacial Curvatures

As stated in Chapter I, the morphologies of microstructures with intricate geometries need to be examined with interfacial curvatures. In differential geometry, a smooth surface, which is at least twice differentiable in three-dimensional Euclidian space $\boldsymbol{R^3}$, can be parameterized by $\boldsymbol{r} = \boldsymbol{r}(u, v)$, where $\boldsymbol{r}$ is a vector function of two independent parameters, u and v. The partial derivatives of $\boldsymbol{r}$ with respect to u and v are denoted as $\boldsymbol{r}_u$ and $\boldsymbol{r}_v$, which lie within the tangent plane of the surface. If $\boldsymbol{r}_u$ and $\boldsymbol{r}_v$ are linearly independent, then $\boldsymbol{r}(u, v)$ is said to be parameterized regularly. Thus, the unit normal vector is given by

$$\boldsymbol{n} = \frac{\boldsymbol{r}_u \times \boldsymbol{r}_v}{|\boldsymbol{r}_u \times \boldsymbol{r}_v|} \ . \tag{2.1}$$

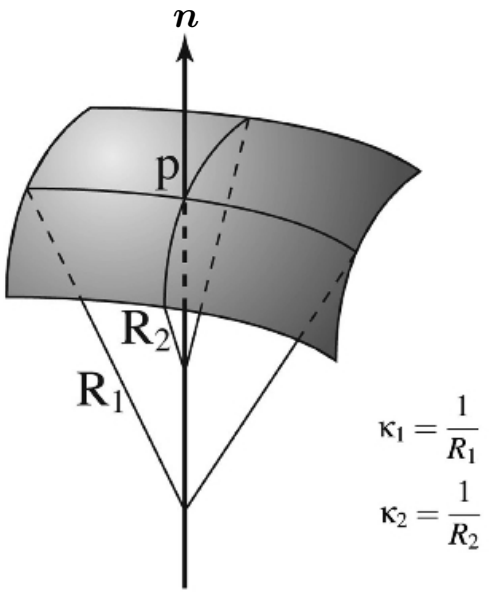

Figure 2.1: A schematic of a differentiable surface with a point P and a normal vector $\boldsymbol{n}$ pointing outwards. The variables R_1 and R_2 indicate the radii of osculating circles along the two principal coordinates. Their reciprocals κ_1 and κ_2 are the minor and major principal curvatures of the surface at point P, respectively. Adapted with permission from [41]. Copyright 2016 by Springer.

The second fundamental form of parametric surface, also known as the shape tensor, is a quadratic expression describing the tangent plane to the smooth surface, defined as

$$\mathrm{II} = L\ du^2 + M\ du\ dv + N\ dv^2\ , \tag{2.2}$$

where the coefficients are the dot products of the second-order partial derivatives of $\boldsymbol{r}$ with respect to the parameters and the normal vector: $L = \boldsymbol{r}_{uu} \cdot \boldsymbol{n}$, $M = \boldsymbol{r}_{uv} \cdot \boldsymbol{n}$, and $N = \boldsymbol{r}_{vv} \cdot \boldsymbol{n}$. If $\boldsymbol{r}_u$ and $\boldsymbol{r}_v$ are orthogonal vectors that results in $M = 0$, then the lines of curvatures which are aligned with $\boldsymbol{r}_u$ and $\boldsymbol{r}_v$ are called the lines of principal curvatures. The normal curvatures defined along the lines of principal curvatures are called the principal curvatures, κ_1 and κ_2, which represent the smallest and the largest curvatures of a surface at a given point, respectively. Figure 2.1 shows the schematic representation of the two principal curvatures defined at a point on a smooth surface.

From the principal curvatures, we can define the mean curvature, H, and the Gaussian curvature, K:

$$H = \frac{1}{2}\left(\kappa_1 + \kappa_2\right) \quad , \tag{2.3}$$

$$K = \kappa_1 \kappa_2 \quad . \tag{2.4}$$

While the principal curvatures and the mean curvature have a dimension of $1/\text{length}$, the Gaussian curvature has a unit of $1/\text{length}^2$. The interfacial morphology can be accurately described by either the two principal curvatures or the pair of mean and Gaussian curvatures. Elliptic-shape surfaces have principal curvatures with an equal sign, where the sign determines the concavity of surface. In terms of the mean and Gaussian curvatures, the elliptic shapes have positive Gaussian curvatures and the sign of the mean curvature determines the concavity. In addition, cylindrical shapes have $K = 0$ since one of the principal curvatures is zero. In contrast, hyperbolic shapes have principal curvatures with opposite signs, or equivalently, have negative Gaussian curvatures. Hyperbolic shapes with $H = 0$ represent symmetric saddle-shaped surfaces.

Neither H or K directly expresses the degree by which a surface is curved on its own. To quantify the overall curvature of an interface, we define the net curvature, d, defined as [43, 44]

$$d = \sqrt{\frac{\kappa_1^2 + \kappa_2^2}{2}} \quad . \tag{2.5}$$

The factor of $1/2$ ensures that the net curvature reduces to $1/R$ for a spherical shape [43]. The advantage of using the net curvature is that the curviness of the interface (and the inverse of the length scale of the feature) can be quantified with a single metric. Figure 2.2 shows an example of two surfaces that have $H = 0$, yet clearly the saddle-shaped surface in Fig. 2.2b has more bend to the surface than the flat surface in Fig. 2.2a. While both surfaces have $H = 0$, they have different net curvatures as the flat surface has $d = 0$ while the saddle-shaped surface has $d > 0$. A similar

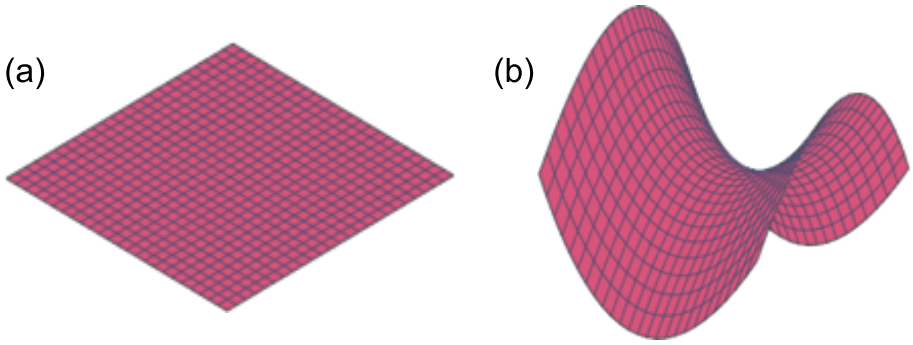

Figure 2.2: A schematic representation of (a) a flat surface with $H = 0$ and a symmetric saddle-shaped surface also with $H = 0$.

analogy can be made with cylinders with varying radii, in which both cylinders have $K = 0$ but their net curvatures will vary depending on their radii. Thus, we will use the net curvature throughout the dissertation to describe the overall curvature of a surface.

2.1.2 Statistical Distribution of Overall Curvatures

The overall morphology of a complex microstructure can be characterized by a probability distribution as a function of curvatures. While the probability distribution in terms of the mean and Gaussian curvatures can describe the overall morphology, this distribution is distorted because two curvatures have different units. An alternative approach is the probability distribution in terms of the principal curvatures, also called the interfacial shape distribution (ISD) [41]. The interfacial shape distribution is the probability, $P_{ISD}(\kappa_1, \kappa_2)$, of finding an interface with a given pair κ_1 and κ_2, which is defined as:

$$P_{ISD}(\kappa_1, \kappa_2) = \frac{A_{ISD}(\kappa_1, \kappa_2)}{A_T}, \tag{2.6}$$

where $A_{ISD}(\kappa_1, \kappa_2)$ is the total surface area of all interfaces with given principal curvatures and A_T is the total surface area of the microstructure examined. This is numerically evaluated by summing interfacial areas that have curvatures within the

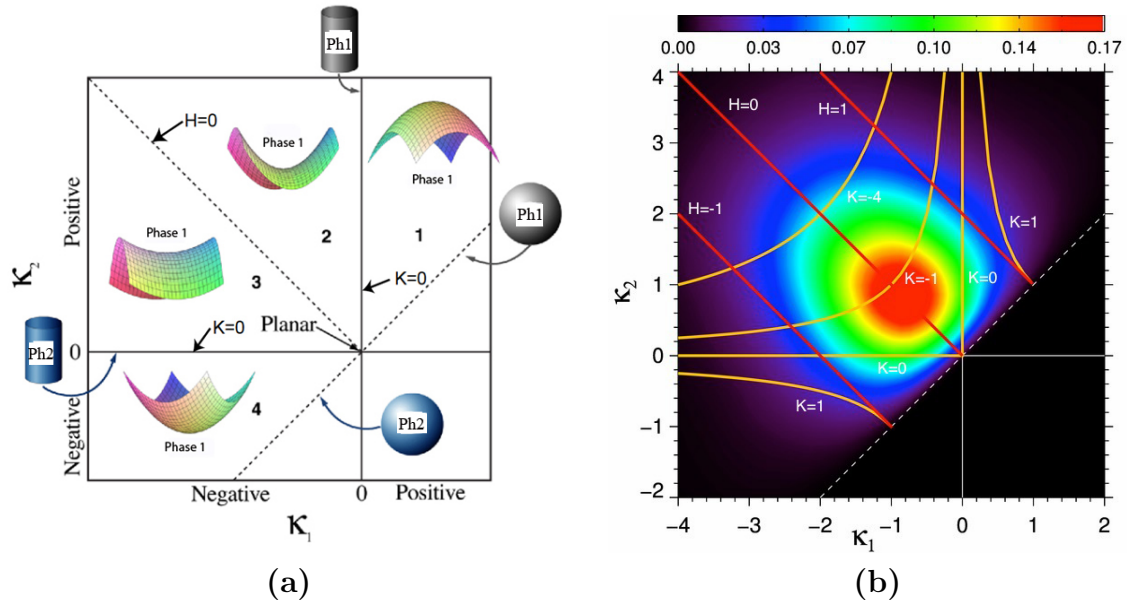

Figure 2.3: (a) A graphical representation of interfacial shapes in the principal curvature space where the interfacial shape distribution is defined. Labels 'Ph1' and 'Ph2' represent the two phases in the system. Adapted with permission from [41]. Copyright 2016 by Springer. (b) The ISD of the AC structure with isolines of constant H and K. The principal curvature coordinates are scaled with characteristic length scale S_v^{-1}.

range of $\kappa_1^i \pm \Delta\kappa_1/2$ and $\kappa_2^i \pm \Delta\kappa_2/2$, where κ_1^i and κ_2^i are the center values of the i-th bin, and $\Delta\kappa_1$ and $\Delta\kappa_2$ are the bin sizes in κ_1 and κ_2, respectively. The bin sizes are chosen such that there is sufficient statistics within the bin while providing sufficient resolution on the curvature space. Labels 1 through 4 in Fig. 2.3a mark the four regions of the ISD that represent different interfacial morphologies. Regions 1 and 4 represent elliptic interfaces and regions 2 and 3 represent saddle-shaped (hyperbolic) interfaces. Figure 2.3b shows the ISD of the AC bicontinuous structure (details of the structure are presented in Chapter IV) with isolines of constant H and K. The red color represents high probability of finding an interface with a given pair of principal curvatures and the dark color represents low probability, as shown on the color bar. It can be observed from the ISD that most of the interfaces of the AC structure are saddle-shaped (negative K). On the other hand, the net curvatures of the interfaces can be determined by the distance between the point on the ISD map and the origin, $\kappa_1 = \kappa_2 = 0$. Figure 2.4 shows the ISD map with isocurves of constant net curvatures (green). The isocurves that are farther away from the origin represent interfaces with higher net curvatures than isocurves closer to the origin.

2.2 Literature Review on the Study of Coarsening

2.2.1 Coarsening of Spherical Particles

The LSW theory presented in the previous chapter is based on the assumption of near zero volume fraction of the particle phase, in which the particle coarsens at a rate determined only by its size relative to the average particle size. Since most experiments are carried out with a finite volume fraction of the coarsening phase, their results have seldom agreed with the LSW theory. A series of subsequent theoretical investigations and experiments have been conducted to develop a theory that describes coarsening in nonzero volume fraction of the particle phase. At a

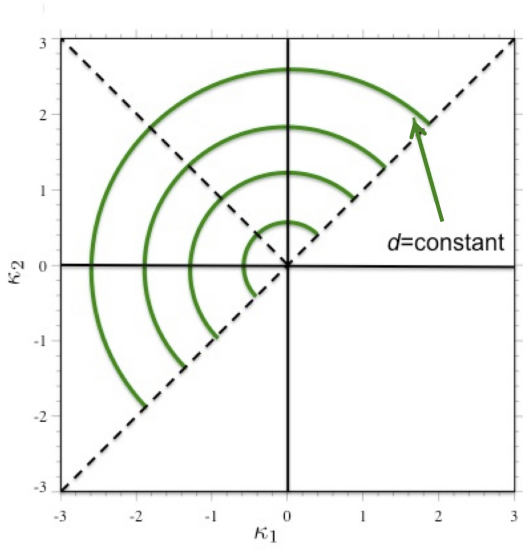

Figure 2.4: The map of the interfacial shape distribution defined in the principal curvature space, with isocurves of constant net curvature, d, displayed as green curves

finite volume fraction, the interparticle diffusional interaction plays a pivotal role in the microstructural evolution and, as a result, the size and spatial distribution of the particles influence the growth rate of individual particles [45]. For instance, two particles with unequal sizes that are close to each other will experience higher coarsening rate than two particles that have the same sizes but are farther away from each other. Thus, in nonzero volume fractions, particles with the same size can have different rates of coarsening depending on the spatial distribution of particles in the vicinity.

Experimentally, Voorhees et al. has confirmed the dependence of growth rate of individual particles on the spatial distribution of nearby particles by studying the coarsening of liquid droplets in a solid matrix in which the coarsening phase constitutes 3% of the volume fraction [46]. Figure 2.5 shows the plot of particle size versus time for select particle sizes of the liquid droplets, in which a particle with initial size of 47 microns contracts during coarsening. The contraction of a particle with a size that is larger than the average particle size is the result of the presence

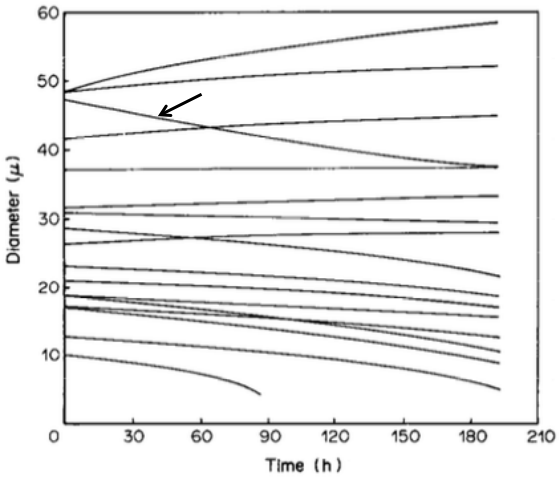

Figure 2.5: A plot of particle size versus time for select particle sizes of the acetone-rich liquid droplets in the succinonitrile matrix. A particle with initial size of 47 microns, which is larger than the average particle size, contracts over time (see the arrow). Adapted with permission from [46]. Copyright 2016 by Elsevier.

of even larger particles in close proximity. This finding contradicts the LSW theory, which states that particles with sizes larger than the average particle size always grow. Thus, the representative growth rate of particles with a given radius in a system with a finite volume fraction must be obtained by taking the average of the different growth rates of the particles with a given radius.

The interparticle diffusional interactions can also alter the morphologies of particles undergoing coarsening. While the LSW theory assumes a spherical geometry of the precipitates based on the isotropic interfacial energy, experiments have shown that isotropic interfacial energy does not always result in spherical particles. Hardy et al. have shown that, at high solid volume fraction, solid Sn particles in the Sn-Pb eutectic liquid matrix evolve into non-spherical morphologies, even though their interfacial energy is isotropic [47]. Figure 2.6 shows the micrographs of Sn particles at various coarsening times, in a system with a high volume fraction of Sn particles. The morphologies of the Sn particles are clearly non-spherical throughout the evolution. Voorhees et al. verified this observation with a two-dimensional numerical simulation

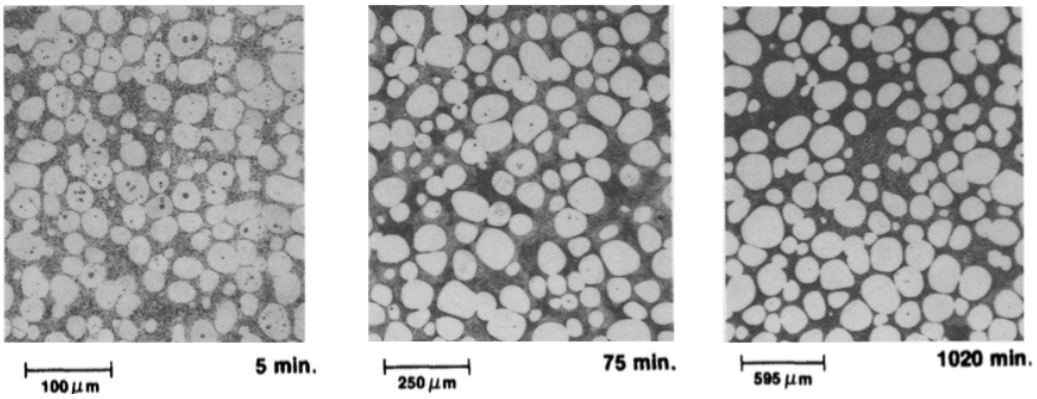

Figure 2.6: Micrographs of Sn particles in a Sn-Pb eutectic liquid matrix at various coarsening times with variable magnification, which effectively scales the size of the images with the average intercept length of the particles. Adapted with permission from [47]. Copyright 2016 by Springer.

of the coarsening of four, initially circular, particles [48]. Figure 2.7 illustrates the morphological evolution of the particle system, in which there are two particles with larger radii that are closer to each other than the other two smaller particles. As the two particles with larger radii grow and approach each other during coarsening, they evolve into non-spherical shapes with flatter interfaces in the region between the two larger particles. In addition, the same study has found that particles in a system with a high volume fraction of the coarsening phase can shift their center-of-mass positions [48].

Since large volume fractions of the coarsening phase can induce additional phenomena such as morphological changes and particle migration, most theories of coarsening have focused on microstructural systems with a low volume fraction of the coarsening phase [49, 50, 51, 52, 53]. These theories of coarsening that account for interparticle diffusional interactions represent the particles in the microstructure as monopole sources and sinks in the concentration field. The magnitude of the source/sink is determined by the size of each particle, which determines the interfacial concentration based on the Gibbs-Thomson condition. While the aforementioned theories alike represent the particles as sources and sinks to determine the growth rate of an individual

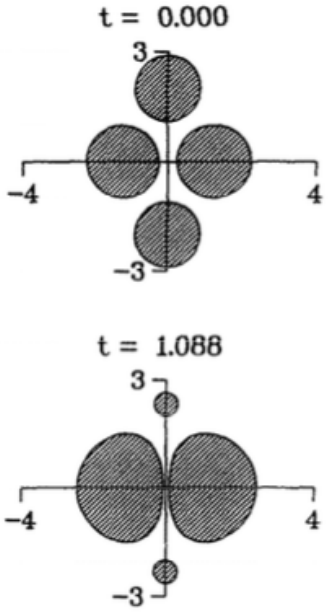

Figure 2.7: Morphological evolution of a system of four initially circular particles (top), in which there are two particles with larger radii that are closer to each other than the other two smaller particles. At the later time (bottom), the larger particles become non-spherical. Adapted with permission from [48]. Copyright 2016 by Elsevier.

particle, each theory employs different statistical averaging scheme to determine the average growth rate of particles for a given radius [45]. Nevertheless, all of the theoretical work have reported that the temporal power law of $\langle R \rangle \propto t^{1/3}$ derived from the LSW theory still holds for nonzero volume fractions, while the rate constant increases with increasing volume fraction of the coarsening phase [49, 50, 51, 52, 53]. Moreover, it has been found that the time-independent particle size distribution becomes broader and more symmetric as the volume fraction of the coarsening phase increases, as shown in Fig. 2.8 [49, 50, 51].

2.2.2 Coarsening of Dendritic Microstructures

As shown in Fig. 1.4, dendrites are tree-like structures that have side branches (secondary, and sometimes tertiary, arms) growing out of the primary arms. Initial studies of the evolution of dendritic microstructures have used the distance between the secondary dendrite arms as the measure of characteristic length scale [2, 37, 54, 55]. The secondary arm spacing, λ_2, increases with coarsening time, analogous to the average particle size for a system of spherical particles, and is also easy to measure from the two-dimensional micrographs. In the case of Al-Cu alloys with low solute concentrations (less than 11 wt.% Cu), experimental observations have shown that λ_2 increases with $t^{1/3}$, which is consistent with the temporal power law predicted by the LSW theory [22]. In addition, it has been found that λ_2 decreases with increasing solute concentration up to the eutectic composition, in which the solid volume fraction decreases and thus the solid dendrites are finer in size [22, 54].

Many theories have been developed to elucidate the morphological evolution of dendrite arms by simplifying their geometries [2, 22, 55, 56, 57]. Kattamis et al. have modeled the dendrite arms as cylinders with constant radius except for one, which has smaller radius [2]. Since the solute concentration at the interface of the thinner arm is higher than the rest due to the Gibbs-Thomson condition, the thinner arm

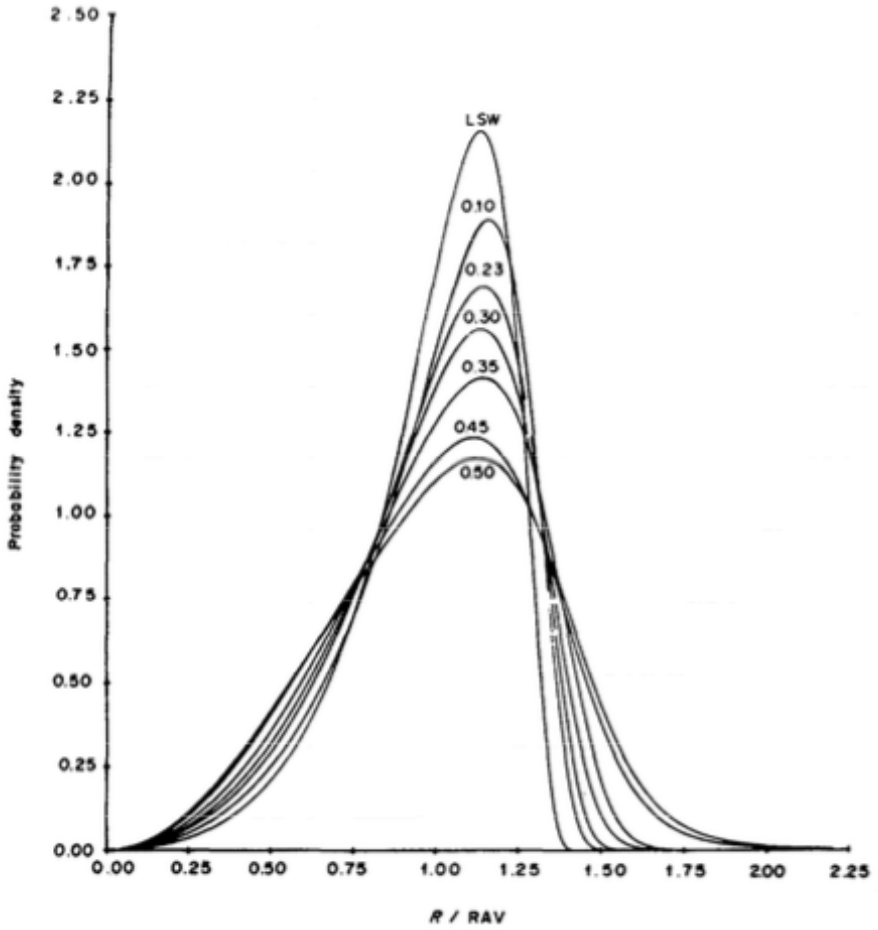

Figure 2.8: Plots of the time-independent particle size distribution for various volume fractions of the coarsening phase obtained from the simulations performed by Voorhees et al. [51]. The number just above or below each of the curve represents the volume fraction of the coarsening phase. The curve with "LSW" label represents the steady-state size particle size distribution in the limit of zero volume fraction. Adapted with permission from [51]. Copyright 2016 by Elsevier.

melts and its radius decreases (radial melting). On the other hand, Kahlweit has modeled the dendrite arms as cylinders with spherical caps at the end [55]. Since the cap has twice the mean curvature of the cylindrical part of the arm, a thinner arm melts from the cap without changing the radii of the arm (axial melting). Based on the same geometrical assumption as Ref. [55], Reeves et al. have considered two arms with different radii in which the thinner arm undergoes axial melting while the larger arm grows [57].

The assumption that dendrite arms can be modeled as cylindrical shapes is generally invalid as the arms themselves have spatially varying curvatures. Some theories have assumed that these secondary dendrite arms are tear-shaped, as shown in Fig. 2.9a [2, 41, 56]. Since the radius of the base of the arm, r_1, is smaller than the radius at the tip, r_2, material flows from the base of the arm to the tip. Thus the tip of the dendrite arm increases its diameter while the base melts away, until it detaches completely from the primary arm. This self-detachment mechanism of dendrite arms has been observed experimentally with the solid-liquid dendritic mixture of NH_4Cl [58]. On the other hand, Young et al. propose that the primary mechanism of coarsening of the dendrites is coalescence [22]. As shown in Fig. 2.9b, the material flows from the bases of the arms to the tips and, as a result, the tips of the dendrites grow, decreasing the distance between the two adjacent tips, d_2 until they coalesce. The coalescence mechanism has also been observed experimentally in the dendritic structure of succinonitrile, as shown in Fig. 2.10. The dendrite arms labeled J and I coalesce at the tips of the arms and a small liquid region is trapped in the solid dendrite [59].

While many theoretical and experimental investigations have utilized the secondary dendrite arm spacing λ_2 to describe the evolution of dendritic microstructures, in some cases, measurement of λ_2 is not practical. Marsh et al. observed that initially Sn-rich dendrites in a Sn-Bi alloy melt change their morphologies and become globu-

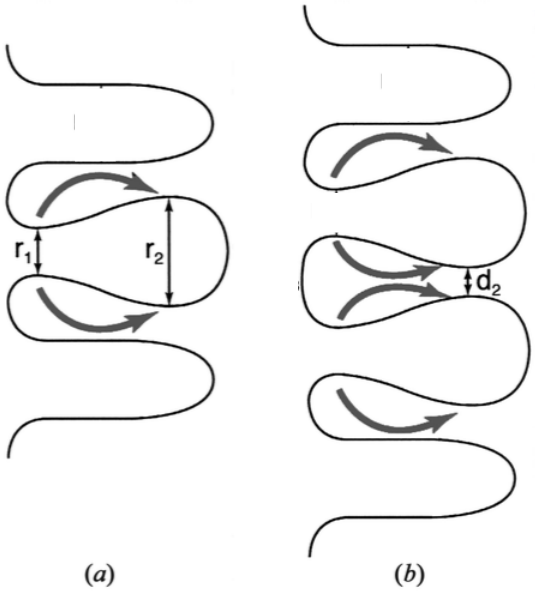

Figure 2.9: Schematics of the dendrite arms modeled as tear-shaped (a) undergoing self-detachment mechanism [56] and (b) coalescence [22]. Adapted with permission from [41]. Copyright 2016 by Springer.

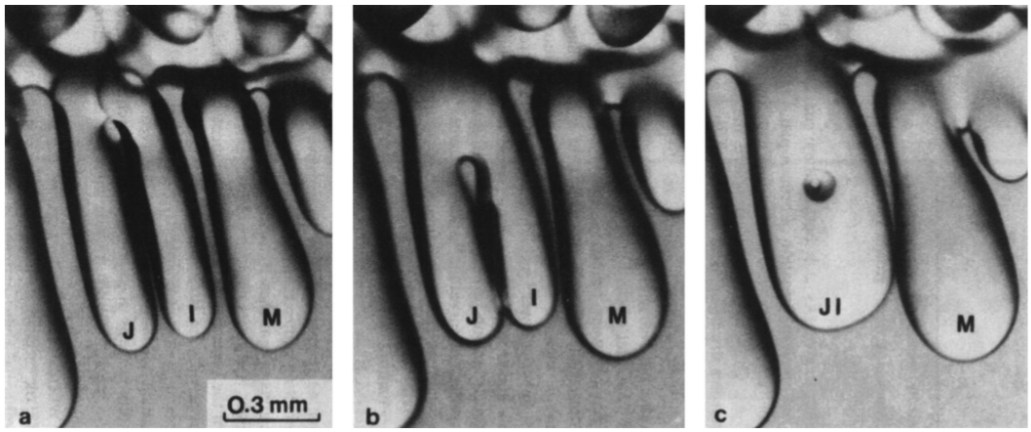

Figure 2.10: Sequential micrographs of a pure succinonitrile sample taken at time intervals of 20-30 minutes, displaying the coalescence of dendrite arms at the tips. Adapted with permission form [59]. Copyright 2016 by Elsevier.

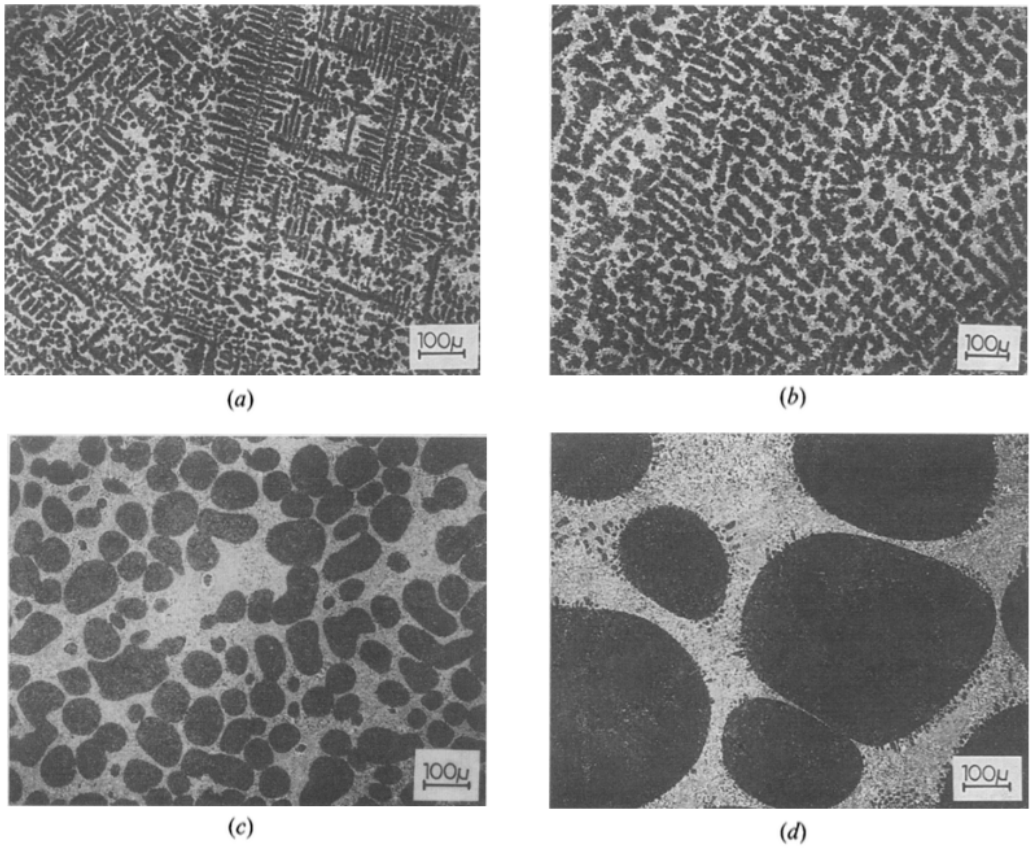

Figure 2.11: Micrographs of Sn-Bi alloy (a) as-cast and at coarsening times (b) after 10 min, (c) after 2.5 hours, and (d) after 10 days. Adapted with permission from [60]. Copyright 2016 by Springer.

lar at long coarsening times, as shown in Fig. 2.11, and thus λ_2 cannot be measured [60]. To circumvent the limitation of λ_2, a more generic measurement of the characteristic length scale in the form of inverse of surface area per unit volume, S_v^{-1}, which is independent of morphology, has been proposed [2, 60]. Marsh et al. have observed that S_v^{-1} scales linearly with $t^{1/3}$ regardless of the changes in the morphology of the microstructure during coarsening [60].

Despite the advantage of S_v^{-1} over λ_2 in the characterization of the length scale, both measurements are inadequate to describe the morphologies of the dendritic microstructures. As stated in Chapter I, such complex microstructures require interfacial curvatures to quantify their morphologies. Mendoza et al. [41] and Fife et al.

[26] have used the interfacial shape distribution defined in the principal curvature space to accurately characterize the morphologies of dendritic microstructure. In a more recent work, with advances in four-dimensional tomography (three-dimensional in space plus time), the correlation between the interfacial velocity and the mean curvature of the dendritic microstructures of Al-Cu alloys have been examined [43]

2.2.3 Coarsening of Bicontinuous Structures

Self-similar structures are ideally suited for developing theoretical understanding because they possess a single-modal distribution of features and because the governing equation becomes time independent when scaled with the characteristic length scale. Two types of complex microstructure that evolve self-similarly are the bicontinuous structures that result from phase decomposition such as spinodal decomposition [38, 39] or phase ordering [61, 62, 63]. Examples of bicontinuous structures can be found in metals [62, 64], polymers [38, 39, 65] and ceramics [66, 67]. Figure 2.12 shows the micrographs of the bicontinuous structures resulting from spinodal decomposition of a polymer mixture [39] and from phase-ordering of antiferromagnetically coupled multilayer films [62]. Similar to the dendritic microstructures, these bicontinuous structures also possess complex morphologies.

Many of the past studies have used scattering experiments such as light scattering (LS) [68, 69], small-angle X-ray scattering (SAXS) [70, 71], and small-angle neutron scattering (SANS) [39, 70, 71], to characterize the bicontinuous structures. From these scattering experiments, a structure factor, which is the Fourier transform of the correlation function, can be obtained. Jinnai et al. have characterized bicontinuous structures resulting from spinodal decomposition in the polymer blend and in the microemulsion through the structure factor [71]. Figure 2.13 shows the plot of structure factor, $S(q)$, versus scaled wave number, q/q_m, of the microemulsion and polymer blend, where q_m is the wave number at the peak of the distribution. The

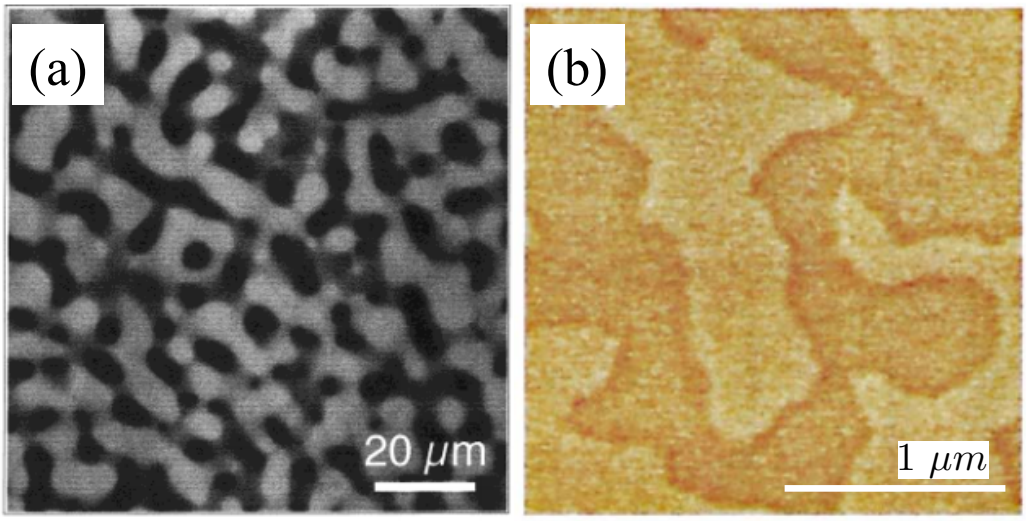

Figure 2.12: (a) A micrograph of the binary mixture of deuterated polybutadiene (DPB) and polybutadiene (PB) resulting from spinodal decomposition. Adapted with permission from [39]. Copyright 2016 by ACS Publications. (b) A micrograph of the antiferromagntically coupled Co/Pt and Co/Ru layers resulting from order-disorder transition. Adapted with permission from [62]. Copyright 2016 by American Physical Society.

plot shows that the structure factors of the microemulsion at different temperatures and the polymer blend have general similarities. The distributions have single-peak shapes and a small shoulder at about $q/q_m = 3$. The same trend has been observed in the structure factor of a bicontinuous structure resulting from spinodal decomposition in a different polymer mixture [38].

The evolution of the bicontinuous structure can also be characterized by examining the temporal evolution of the structure factor through the light scattering intensity distribution. Figure 2.14 shows the temporal evolution of the light scattering intensity distribution of a bicontinuous structure found in a binary polymer mixture with a symmetric volume fraction ratio [39]. Similar to the structure factors shown in Fig. 2.13, the intensity distributions at various times have a single peak . However, as the microstructure of the polymer mixture coarsens, the wave number corresponding to the peak location of the intensity distribution (q_m) shifts to a lower wave number,

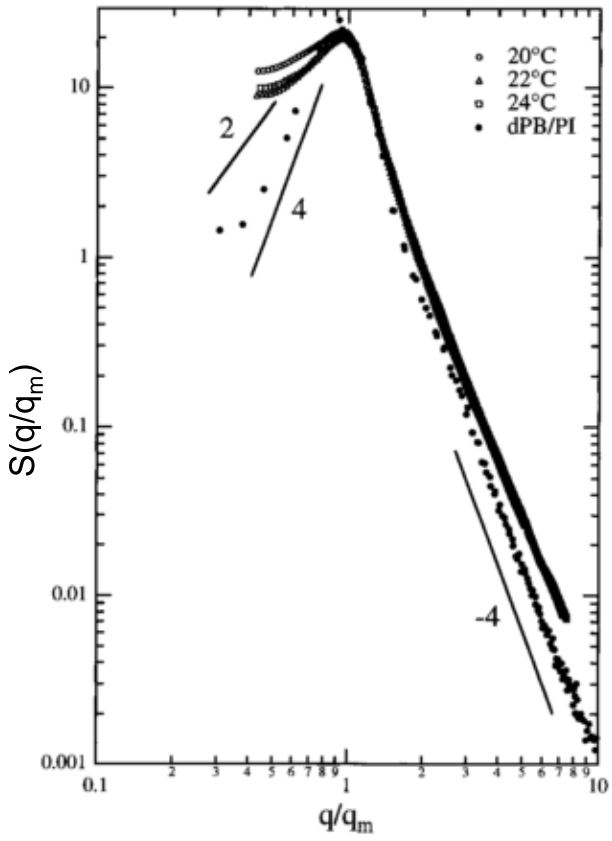

Figure 2.13: A plot of structure factor, $S(q)$, as a function of scaled wave number q/q_m of the microemulsion samples at various temperatures and of the perdeuterated polybutadiene (DPB) and polyisoprene (PI) polymer blend. The solid lines represent $S(q)\,(q/q_m)^n$, where the value of exponent n is the number marked next to the lines. Adapted with permission from [71]. Copyright 2016 by ACS Publications.

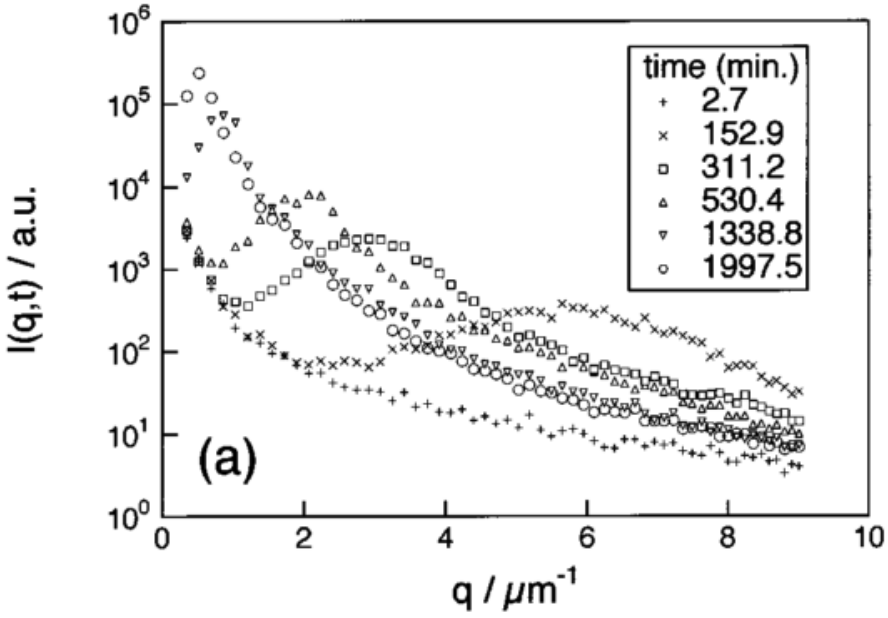

Figure 2.14: Temporal evolution of the scattering light intensity distribution, $I(q,t)$ as a function of the wave number q of a bicontinuous structure resulting from spinodal decomposition in a binary mixture of deuterated polybutadiene (DPB) and polybutadiene (PB). Adapted with permission from [39]. Copyright 2016 by ACS Publications.

which indicates that the size of the dominant length-scale feature increases. In addition, the scattering intensity distributions become narrower and the height of the peak increases at longer times, which suggests that the sizes of the features in the microstructures become more uniform.

While characteristic length scales such as the size of the dominant length scale feature can be obtained from the structure factor, it cannot accurately describe the morphology of bicontinuous structures. Similar to the study of dendritic microstructures, the morphological evolution of the bicontinuous structures needs to be characterized by interfacial curvatures. In Ref. [39], the morphological evolution of the bicontinuous structure is examined with a probability distribution in terms of the mean curvature and in terms of the Gaussian curvature. Figure 2.15 shows the probability distributions as functions of scaled mean and Gaussian curvatures at various coarsening times. The mean curvature is scaled by S_v^{-1} while the Gaussian curvature

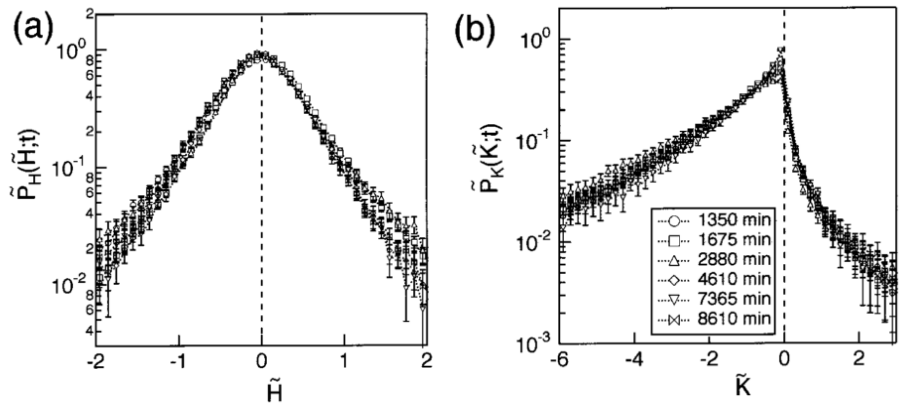

Figure 2.15: A probability distribution as a function of (a) the scaled mean curvature and (b) the scaled Gaussian curvature, at various times of evolution of a bicontinuous structure resulting from spinodal decomposition in a binary mixture of deuterated polybutadiene (DPB) and polybutadiene (PB). Adapted with permission from [39]. Copyright 2016 by ACS Publications.

is scaled by S_v^{-2}. Figure 2.15a show that the average mean curvature is zero for the bicontinuous structure with a symmetric volume fraction ratio. In contrast, Fig. 2.15b shows that the most of the interfaces of the bicontinuous structure are saddle-shaped and that the average Gaussian curvature is negative throughout the evolution. The scaling of both curvature distributions implies that the microstructure evolves in a self-similar manner.

On the other hand, Kwon et al. have examined the morphological evolution of the simulated bicontinuous structures with the interfacial shape distribution (defined in the principal curvature space) [72]. The time-independent ISDs demonstrate that the bicontinuous structures resulting from either spinodal decomposition or phase-ordering evolve self-similarly in the late stage of coarsening. In a related study, it has been found that, regardless of the volume fraction, the bicontinuous structures resulting from spinodal decomposition have characteristic length scales S_v^{-1} that obey the $t^{1/3}$ power law, as in the LSW theory [42]. In a different study, Genau et al. have examined the spatial correlations of interfacial curvatures of the bicontinuous structures resulting from spinodal decomposition. The study shows that curvatures with

equal sign show strong correlation at short distances, whereas curvatures of opposite signs show strong correlation at intermediate distances [73]. While the morphologies of the bicontinuous structures have been examined extensively with curvature, there is still limited understanding of the evolution of curvatures in these structures.

2.3 Phase-Field Method

The phase-field method is a computational technique for simulating phase transformations [74]. The phase-field method is based on the diffuse-interface theory, where the value of an order parameter, ϕ, smoothly varies across an interfacial region with a finite thickness from a value representing a phase to another representing a different phase. The diffuse-interface approach eliminates the need to explicitly track the location of interfaces since this information is embedded in ϕ, which is evolved based on the governing phase-field equation. The following section briefly explains the underlying physics behind the model.

In a two-phase heterogeneous system, the total free energy, G, of the system can be divided into

$$G = G_{\text{Phase 1}} + G_{\text{Interface}} + G_{\text{Phase 2}} \ , \tag{2.7}$$

where $G_{\text{Phase 1}}$, $G_{\text{Phase 2}}$, and $G_{\text{Interface}}$ are the free energy associated with the two bulk phases and the interface, respectively [40]. During coarsening, $G_{\text{Interface}}$ decreases as the overall interfacial area decreases while $G_{\text{Phase 1}}$ and $G_{\text{Phase 2}}$ remain constant resulting from the fixed volume fractions of the phases.

The total free energy of the system, Eq. (2.7), can be described in the functional form as

$$G = \int_{\Omega} \left\{ g\left(\phi\right) + \frac{1}{2}\epsilon^2 \left|\nabla\phi\right|^2 \right\} dV \ , \tag{2.8}$$

where Ω is the domain of the system, ϵ^2 is the gradient energy coefficient, and $g(\phi)$ is the free energy density. The free energy density for a given material system can be obtained from theoretical calculations [75] such as the first-principles density functional theory (DFT) [76, 77], atomistic molecular dynamics (MD) [78, 79], and Monte Carlo (MC) simulations [80, 81], as well as from CALPHAD approach [82, 83]. In the phase-field method, the free energy density is often simplified into a double-well potential of the form

$$g(\phi) = \frac{W}{4}\phi^2(1-\phi)^2 \quad , \tag{2.9}$$

where W is the coefficient that controls the height of the double well [84]. The two minima of the free energy density, at $\phi = 0$ and $\phi = 1$, determine the equilibrium values of the order parameter in the bulk phases. The chemical potential, μ, is derived from the variational derivative of the free energy functional, Eq. (2.8),

$$\mu = \frac{\delta G}{\delta \phi} = \frac{dg}{d\phi} - \epsilon^2 \nabla^2 \phi \ , \tag{2.10}$$

$$\frac{dg}{d\phi} = \frac{W}{2}\phi(1-\phi)(1-2\phi) \quad . \tag{2.11}$$

If the nonconserved order parameter is labeled as η and the conserved order parameter labeled as c, then the governing phase-field equations for nonconserved and conserved dynamics are

$$\frac{\partial \eta}{\partial t} = -L_\eta \frac{\delta G}{\delta \eta} = -L_\eta \left(\frac{dg}{d\eta} - \epsilon^2 \nabla^2 \eta \right) \quad , \tag{2.12}$$

$$\frac{\partial c}{\partial t} = \nabla \cdot L_c \nabla \frac{\delta G}{\delta c} = L_c \nabla^2 \left(\frac{dg}{dc} - \epsilon^2 \nabla^2 c \right) \quad , \tag{2.13}$$

respectively, where L_η and L_c are the mobility coefficients treated as a unit constant here for simplicity. Equations (2.12 & 2.13) are commonly referred to as the Allen-Cahn equation and the Cahn-Hilliard equation, respectively [84, 85, 86]. For simplicity, the order parameters will be represented by ϕ hereafter, regardless of whether conserved or nonconserved.

While both the Allen-Cahn and Cahn-Hilliard equations are expressed in terms of the chemical potential derived from the variational derivative of the energy functional, their kinetics and the resulting morphologies of the simulated structures are very different. In nonconserved dynamics, the interfacial evolution is the motion by mean curvature, and the order parameter changes such that it results in the steepest descent of the free energy functional, Eq. (2.8). Moreover, the volume fractions of the phases are not conserved, except in the symmetric microstructural system with a 50:50 volume fraction ratio. In contrast, the kinetics in conserved dynamics is determined by long-range diffusion. The Laplacian of the chemical potential in Eq. (2.13) ensures that the each species is conserved. Thus, in the absence of large concentration shift (e.g., from the Gibbs-Thomson effect), the volume fractions of the phases also remain constant.

Despite the different kinetics induced by Eqs. (2.12) & (2.13), both governing equations results in smooth interfacial profiles. At equilibrium, the Allen-Cahn equation simplifies to $\mu = 0$ while the Cahn-Hilliard equation simplifies to $\mu =$ constant. Therefore, for a planar interface centered at $x = 0$, the solutions to both governing equations yield the same interfacial profile described as

$$\phi\left(x\right) = \frac{1}{2}\left[1 + \tanh\left(\frac{2x}{\delta}\right)\right] \quad , \tag{2.14}$$

$$\delta = 4\sqrt{\frac{2\epsilon^2}{W}} \quad , \tag{2.15}$$

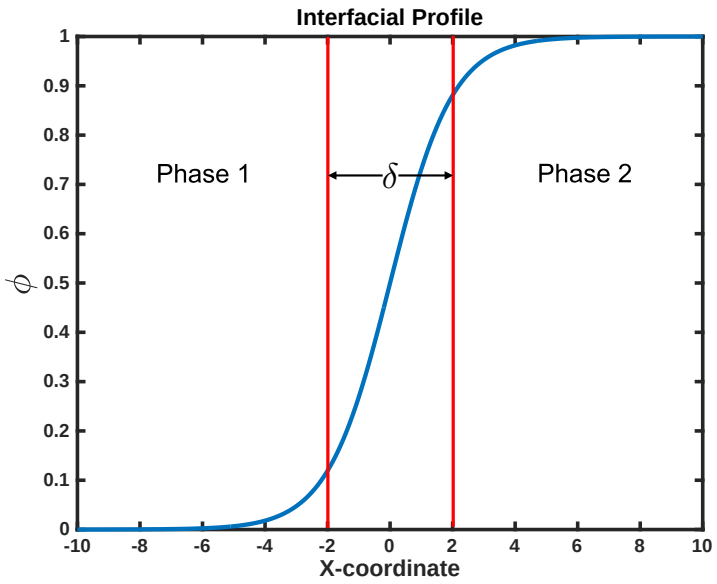

Figure 2.16: Planar interfacial profile, represented as a blue curve, based on Eq. (2.14) with $\delta = 4$.

where δ is the interfacial thickness defined as a region where ϕ varies between 0.1 and 0.9. Figure (2.16) shows the interfacial profile based on Eq. (2.14) with $\delta = 4$.

Since both governing equations are derived from the same free energy functional, Eq. (2.8), the pseudo one-dimensional interfacial energy γ derived from both governing equations is defined as [84]

$$\gamma = \int_{-\infty}^{\infty} \epsilon^2 \left(\frac{\partial \phi}{\partial x}\right)^2 dx \ . \tag{2.16}$$

At equilibrium, Eq. (2.16) can be re-written as

$$\gamma = \int_{0}^{1} \sqrt{2\epsilon^2 g\left(\phi\right)}\, d\phi \ , \tag{2.17}$$

with the change in the variable of integration. After solving the integral, Eq. (2.17)

further simplifies to

$$\gamma = \frac{1}{6}\sqrt{\frac{\epsilon^2 W}{2}}. \tag{2.18}$$

Equations (2.15) & (2.18) demonstrate that the choice of ϵ^2 and W determines the interfacial thickness and the interfacial energy of the system.

2.4 Finite Difference Method

Nonlinear partial differential equations, such as the Allen-Cahn and the Cahn-Hilliard equations, must be solved numerically. There are number of methods that can be employed, including finite difference method (FDM), finite element method (FEM), and finite volume method (FVM), to solve partial differential equations (PDE). FDM approximates the derivatives in the PDE into simple algebraic expressions (obtained via Taylor expansion) in terms of the unknown function defined at every grid point in the domain, generally in the Cartesian coordinate. The simple implementation of FDM on a uniform grid system has been applied to solve a wide variety of PDEs [87]. On the other hand, FEM divides the domain of consideration into regularly or irregularly shaped "finite elements" and determines an approximation of the solution of the PDE for each element. FEM is employed in applications that involve solving PDEs in domains with complex geometries, such as solving the heat equation in vehicle components [87]. Lastly, FVM represents each grid point as a cubic cell (in three-dimension) with a finite volume and thus the divergence operator is substituted with the surface integral using the divergence theorem. Since the divergence operator appears in the conservation equation, FVM is commonly utilized in computational fluid dynamics calculations [75]. While each method has its own advantages, we will employ FDM to numerically solve the governing phase-field equations since this method on a Cartesian grid is relatively easy to implement and computationally less

expensive in three-dimension than the other two methods discussed above.

The finite difference methods require discretization of the computational domain. The discretization of a continuous variable x defined in the range of $[X_1, X_2]$ can be represented as

$$x_i = X_1 + i\Delta x, \quad i = 0, 1, 2... \ , \tag{2.19}$$

where x_i is the discretized representation of x, and Δx is the grid spacing [88]. Similarly, the discretization of a continuous function $q(x)$ can be represented in terms of x_i as

$$q_i = q(x_i), \tag{2.20}$$

where q_i is the discretized representation of q. Since q_i is a discrete function whose values are only defined at x_i, the choice of Δx determines the accuracy of the discretization. Smaller Δx increases the accuracy of the discrete function compared to its continuous counterpart, but this is achieved at the cost of numerical efficiency.

After discretizing the variables, the spatial derivatives of the function q can be evaluated using the finite difference method, which is based on the Taylor expansion. The Taylor expansion of $q(x_{i+1})$ about the point x_i is defined as

$$q(x_{i+1}) = q(x_i) + q'(x_i)\Delta x + \frac{1}{2!}q''(x_i)\Delta x^2 + \frac{1}{3!}q'''(x_i)\Delta x^3 + ... \tag{2.21}$$

Similarly, the Taylor expansion of $q(x_{i-1})$ about the point x_i is defined as

$$q(x_{i-1}) = q(x_i) - q'(x_i)\Delta x + \frac{1}{2!}q''(x_i)\Delta x^2 - \frac{1}{3!}q'''(x_i)\Delta x^3 + ... \tag{2.22}$$

The first-order spatial derivative $q'(x_i)$ can be obtained by subtracting Eq. (2.22) from Eq. (2.21), which results in

$$q'(x_i) = \frac{q(x_{i+1}) - q(x_{i-1})}{2\Delta x} + \mathcal{O}(\Delta x^2) \ , \tag{2.23}$$

where $\mathcal{O}(\Delta x^2)$ indicates that the expression has an error in the order of Δx^2 [88]. Since the spatial derivative of q at x_i requires the values of the function at the two adjacent coordinates, x_{i-1} and x_{i+1}, Eq. (2.23) is referred to as the central differencing scheme. Similarly, the second derivative $q''(x_i)$ can also be evaluated with the central differencing scheme by first calculating $q'(x_{i+1/2})$ and $q'(x_{i-1/2})$,

$$q''(x_i) = \frac{q'(x_{i+1/2}) - q'(x_{i-1/2})}{\Delta x} = \frac{\dfrac{q(x_{i+1}) - q(x_i)}{\Delta x} - \dfrac{q(x_i) - q(x_{i-1})}{\Delta x}}{\Delta x} \tag{2.24}$$

$$= \frac{q(x_{i+1}) + q(x_{i-1}) - 2q(x_i)}{\Delta x^2} + \mathcal{O}\left(\Delta x^2\right) \ ,$$

which is also second-order accurate.

On the other hand, the temporal derivative can be evaluated using the forward Euler differencing scheme. Similar to the discretization of x, time t defined in the interval $[T_1, T_2]$ can be discretized as

$$t_p = T_1 + p\Delta t, \quad p = 0, 1, 2... \ . \tag{2.25}$$

where Δt is the time step size [88]. If the continuous function q is defined in both space and time, it can be discretized in terms of the discrete variables x_i and t_p,

$$q_i = q(x_i, t_p) \ . \tag{2.26}$$

The forward Euler scheme can be obtained from the Taylor series expansion of $q(x_i, t_{p+1})$ about x_i and t_p,

$$q(x_i,t_{p+1}) = q(x_i, t_p) + \frac{\partial q(x_i, t_p)}{\partial t}\Delta t \ , \tag{2.27}$$

where the higher-order terms are ignored [88]. Since the governing phase-field equa-

tions are in the form of

$$\frac{\partial q}{\partial t} = f(q) \ , \tag{2.28}$$

where $f(q)$ is a functional consisting of the spatial derivatives of q, Eq. (2.27) can be re-written as

$$q(x_i, t_{p+1}) = q(x_i, t_p) + f(q(x_i, t_p))\Delta t \ . \tag{2.29}$$

Equation (2.29) shows that the value of the function q at the next time step $p+1$ is explicitly determined based on values of the function at the current time step p. Therefore, this scheme is fully explicit, i.e., the unknown quantity is determined solely by known quantities [88].

CHAPTER III

Application of the Level-Set Method to the Analysis of an Evolving Microstructure

The material presented in this chapter is based on the published manuscript "C.-L. Park, P. W. Voorhees, and. K. Thornton. *Application of the Level-Set Method to the Analysis of an Evolving Microstructure*. Computational Materials Science, 85:46-58, 2014."

3.1 Introduction

The study of coarsening requires accurate quantification of the morphology of complex microstructures. In order to study microstructures to the full extent, it is often necessary to analyze three-dimensional (3-D) microstructures, rather than two-dimensional (2-D) cross-sectional images. Advances in experimental tools and computing resources have made the studies of 3-D microstructures more accessible [89, 90, 91]. Experimental techniques such as mechanical-serial-sectioning optical microscopy [24, 26, 92, 93], X-ray tomography [94, 95, 96, 97, 98], and dual-beam focused-ion-beam scanning electron microscopy [99, 100, 101, 102] can now provide detailed 3-D microstructures. In addition, computational tools such as phase-field method [42, 72, 74, 103, 104] and level-set method [105, 106, 107] can be used to

simulate the evolution of 3-D microstructures.

There are a number of 3-D characterization approaches, but, in some situations, interfacial curvatures are the preferred measure for characterizing complex microstructures due to their integral role in microstructural evolution. For example, the kinetics of coarsening is dictated by the curvature of the interface. Furthermore the rate of changes of curvatures can help elucidate the evolution of morphology and topology. It is thus clear that the ability to numerically calculate the interfacial quantities such as curvatures and their rate of changes (rates of change) from 3-D data sets is essential in developing an understanding of microstructural evolution.

Several numerical schemes for computing interfacial curvatures have been developed in the past. These numerical methods can be largely classified into two main groups: surface-mesh-based methods and voxel-based methods (voxels are 3-D counterpart of pixels, which stands for volumetric pixels). The surface-mesh-based methods compute curvatures on a 3-D network of triangulated mesh that represent interfaces using the positional information of the mesh vertices. On the other hand, voxel-based methods compute curvatures using the values of a function at voxels that are close to the interfaces, which are typically defined as regions where the values of the function at the voxels are between the two bulk phase values. Most triangulated-mesh-based methods can be further categorized as either a "surface fitting" method or a "discrete" method [108]. A surface fitting method determines the curvature at each vertex by obtaining a quadratic (or cubic for higher accuracy) equation for a parameterized surface that best fits the interface [109, 110, 111]. On the contrary, discrete methods compute curvatures directly using formulas derived from differential geometry, such as Gauss-Bonnet theorem [111, 112, 113] and Euler theorem [111, 114, 115], without analytically fitting the surface. Similarly, voxel-based methods can also be divided into two subgroups: methods that require spatial derivatives across the interface, such those involving the level-set method [116, 117], and methods that do not

require any spatial derivative [118, 119]. In this chapter, we focus on the derivative-based approach combined with the level-set method for computing curvatures since the methodology is straightforward and is also computationally efficient, which is particularly advantageous with large 3-D data sets.

However, there is one major challenge in computing interfacial quantities, such as curvatures, using the level-set method. Numerical calculations of curvatures require the evaluation of high-order derivatives across the interface, which become inaccurate when interfacial resolution is low. Experimental microstructure data often describe the microstructure through a contrast difference between two phases. In such cases, the interfaces between two phases are described by few pixels or voxels and thus the reconstructed interfaces form a "wedding cake" structure (having stepped surface rather than smooth) due to the sharp change of contrast across the interfaces. For the phase-field approach, order parameters with smooth transitions describe the phase boundaries, but they typically contain only two to five Cartesian grid points (four grid points for all order parameters simulated in this thesis), which presents problems in the quantitative analysis of the interfacial quantities.

A simple solution to the sharp transition of the microstructural data across interfaces is to apply the volume smoothing technique. This method simply averages the value of data over the neighboring Cartesian grid points with a set width. However, smoothing the data sufficiently for evaluating high-order derivatives using this approach leads to substantial shift in the interfacial position. As a result, interfacial quantities, such as curvatures, calculated from the volume-averaged data may not accurately represent the morphology of the microstructure or its evolution.

Therefore, we have developed an advanced yet computationally inexpensive smoothing algorithm, which we term "level-set smoothing," that can be applied to any voxel-based data describing a two-phase structure. The level-set smoothing method is a set of sequential data-processing schemes that consists of first generating the signed

distance function for the given microstructure using the level-set method, followed by smoothing via diffusion. The proposed smoothing method can facilitate accurate calculation of interfacial quantities with minimal displacement of interfaces during the smoothing process, enabling quantification of morphology and its evolution for a 3-D microstructure.

In this chapter, we present the algorithm for the level-set smoothing method and demonstrate its effectiveness in calculating various types of interfacial quantities through a series of validation tests. We also list numerical algorithms that can be used to calculate various interfacial quantities, including rate of change quantities. For the rate of changes of curvatures, we present two methods, advective and convective, for a comparison.

3.2 Numerical Methods

3.2.1 Level-Set Smoothing Method

The level-set iterations generate the signed distance function near the interfaces for the microstructure. Since the level-set iteration only smoothes out the noise in the first derivative, we apply diffusion smoothing as the second step to remove noise in higher derivatives. The details for each of these processes are described below. From here onwards, a "grid point" refers to a voxel on a Cartesian-grid system.

3.2.1.1 Level-Set Method

In the level-set approach, an interface is represented by a contour where a level-set function, φ, takes a predetermined value, typically zero. The level-set method has been applied to study a wide range of microstructural evolution [105, 106, 107, 120, 121]. In many cases, the level-set function is assumed to be a signed distance function, where the magnitude of the function is given by the distance from the

nearest interface, while the sign indicates one phase or another. Given a function that is positive in one phase and negative in another phase, the signed distance function can be calculated by iterating the following equation until converged:

$$\frac{\partial \varphi}{\partial \tau} = \mathrm{S}(\varphi)(1 - |\nabla \varphi|), \tag{3.1}$$

where $\mathrm{S}(\varphi)$ is a smoothed sign function, which will be defined later in this section, and the time, τ, is an iteration time that is not associated with any physical evolution. Equation (3.1) will be referred to as the level-set equation hereafter. A signed distance function representing the microstructure can be obtained from microstructural data from computer simulations or experiments.

To use simulated data, described by the order parameter, ϕ (note the difference in the font between ϕ and φ), in the level-set equation, we prepare the data as follows to best preserve interfacial location during the smoothing process. We begin with ϕ, which describes a two-phase structure where the phases are defined by bulk values, such as $\phi = 0$ or 1, and the phase boundary defined as the region where ϕ transitions between the bulk values. Since the zero level-set defines the interface, the value of order parameter needs to be adjusted by adding or subtracting a constant if the interfacial value of ϕ is nonzero. Additionally, we found that Eq. (3.1) converges more quickly and accurately with a minimal shift of the interface, if the range of ϕ is adjusted so that the magnitude of the gradient is approximately one near the interface (which is the steady-state condition of Eq. (3.1)). For example, if the input order parameter, ϕ, has the bulk phase values defined at 0 and 1 while the phase boundary has a nondimensional length of δ, then ϕ needs to be translated and scaled such that it varies from $-\delta/2$ to $\delta/2$. This adjusted order parameter then becomes the initial condition, φ^0, and has the property $|\nabla \varphi^0| \simeq 1$ near the interface.

The level-set equation, Eq. (3.1), is a modification of re-initialization equation

developed by Sussman, et al. [122]. The discretized version of Eq. (3.1) in a 3-D Cartesian grid system, where i, j, and k denote the indices for x, y, and z positions, respectively, is

$$\varphi_{ijk}^{N+1} = \varphi_{ijk}^{N} + \Delta\tau \cdot \mathrm{S}(\varphi_{ijk}^{N}) G(\varphi_{ijk}^{N}), \tag{3.2}$$

where $\mathrm{S}(\varphi_{ijk})$ is the numerical implementation of the smoothed sign function (explained below), and $G(\varphi_{ijk})$ is the numerical approximation for $1 - |\nabla\varphi|$ at a grid point (i, j, k). Following Sussman, $G(\varphi_{ijk})$ is calculated using a first-order upwind scheme [122]. If we define one-sided derivatives as

$$\begin{aligned} a &= \frac{\varphi_{i,j,k} - \varphi_{i-1,j,k}}{\Delta x} \ , \ b = \frac{\varphi_{i+1,j,k} - \varphi_{i,j,k}}{\Delta x} \\ c &= \frac{\varphi_{i,j,k} - \varphi_{i,j-1,k}}{\Delta y} \ , \ d = \frac{\varphi_{i,j+1,k} - \varphi_{i,j,k}}{\Delta y} \\ e &= \frac{\varphi_{i,j,k} - \varphi_{i,j,k-1}}{\Delta z} \ , \ f = \frac{\varphi_{i,j,k+1} - \varphi_{i,j,k}}{\Delta z} \ , \end{aligned} \tag{3.3}$$

then $G(\varphi_{ijk})$ is evaluated as

$$G(\varphi_{ijk}) = \begin{cases} 1 - \sqrt{\max((a^+)^2, (b^-)^2) + \max((c^+)^2, (d^-)^2) + \max((e^+)^2, (f^-)^2)} \\ \qquad \text{if } \varphi_{ijk} > 0 \ , \\ 1 - \sqrt{\max((a^-)^2, (b^+)^2) + \max((c^-)^2, (d^+)^2) + \max((e^-)^2, (f^+)^2)} \\ \qquad \text{if } \varphi_{ijk} < 0 \ , \\ 0 \qquad \text{if } \varphi_{ijk} = 0 \ , \end{cases} \tag{3.4}$$

where the superscript $^+$ indicates that only the positive values of the derivatives are considered (if the value of the derivative is negative then zero is used). Similarly, the superscript $^-$ indicates that only the negative values of the derivatives are considered. This monotone scheme possesses improved stability over standard central differencing and also ensures that φ near the interfaces converges to the steady-state

first. While we adopt the same numerical scheme to calculate $1 - |\nabla\varphi|$ as Sussman's, our numerical implementation of the sign function is modified such that shift in the interfacial position is reduced. The smoothed sign function, $\mathrm{S}(\varphi)$, used in our level-set formulation is defined as

$$\mathrm{S}(\varphi_{ijk}) = \varphi_{ijk} \Big/ \sqrt{\varphi_{ijk}^2 + \zeta^2}, \tag{3.5}$$

where the numerical parameter, ζ, is used to regularize the singularity in the numerical implementation of $\mathrm{S}(\varphi)$. There are two differences between our smoothed sign function and the sign function adopted by Sussman: the smoothed sign function can vary during the level-set iteration and uses much larger value of ζ. For a typical sign function, a very small value of ζ is used so that the sign function returns a value of either approximately 1 or -1. We employ a larger value of ζ, one that is comparable to the range of φ^0, to smooth the sign function; hence we refer to $\mathrm{S}(\varphi)$ as a "smoothed sign function." These two modifications ensure that the effective time step, $\Delta\tau \cdot \mathrm{S}(\varphi_{ijk}^N)$, actively changes as φ approaches the signed distance function near the interface. The effective time step is smaller in the region near the interfaces, where the level-set equation converges faster and higher accuracy is needed, and is larger in the region further away, where the equation converges slower and less accuracy is needed.

However, even with the adjustment of the input such that $|\nabla\varphi^0| = 1$ at the interface and the use of the smoothed sign function that reduces the effective time step for grid points near interfaces, the interfacial location can shift slightly in high curvature regions (usually at distances smaller than a voxel, which is still undesired). One way to mitigate this problem is by limiting the number of iterations of the level-set method. Calculation of interfacial quantities requires the level-set function in the form of a signed distance function only within a certain number of grid points near

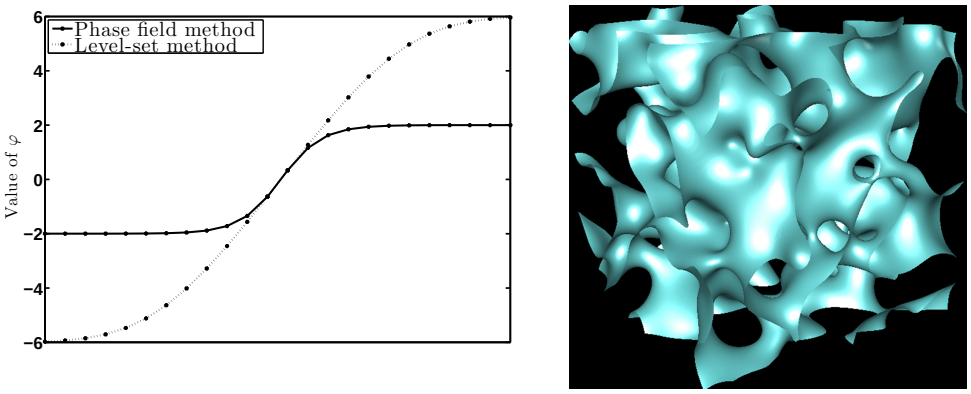

(a) **(b)**

Figure 3.1: a) The interfacial profile of the AC structure (details of the structure are discussed in Section 3.2.2), comparing the input function from phase-field order parameter and the level-set function obtained using the scheme described Section 3.2.1.1. The solid line shows the phase-field order parameter describing the two phases, scaled such that the magnitude of the gradient at interface is unity. The dotted line shows the level-set function whose value near the interface ($3\Delta x$ on each side) is the signed distance from the nearest interface. b) Morphology of the bicontinuous AC structure at the simulation time of $t_0 = 600$.

the interface. For example, the number of grid points, N, near the interface required for calculating curvature is determined by the width of the stencil used to calculate the high-order derivatives. With the numerical scheme adopted, $N = 6\Delta x$ ($3\Delta x$ on both sides of the interface) is sufficient to calculate all of the interfacial quantities discussed in this dissertation, including dynamic interfacial quantities (rate of changes of interfacial characteristics). To provide adequate iteration time for the level-set function to converge to the signed distance function in the region within $3\Delta x$ of the interfaces, the level-set equation is iterated until the maximum magnitude of the level-set function reaches $6\Delta x$ (twice the distance over which the distance function is desired), as shown in Fig. 3.1a. Once the iteration is complete, the level-set method produces a signed distance function, φ, near the interface.

3.2.1.2 Diffusion smoothing method

The signed distance function obtained above contains a significant amount of numerical noise in the second derivative. To remove noise in the second derivative, diffusion smoothing, achieved by evolving the standard diffusion equation, is applied to the level-set function. The dimensionless diffusion equation is given by

$$\frac{\partial \varphi}{\partial \tau} = \nabla^2 \varphi, \tag{3.6}$$

where, τ is a nonphysical iterative time. Over-iteration of diffusion smoothing can significantly alter the location of the interfaces. This is avoided by limiting the diffusion smoothing to the bare minimum required to eliminate noise in the second derivative.

The appropriate amount of diffusion smoothing depends on the quantity to be calculated. Calculation of static interfacial quantities, such as curvatures, requires a small number of iterations for diffusion smoothing; we use 20 iteration steps with time-step of $0.1(\Delta x)^2$. On the other hand, calculation of dynamic interfacial quantities, such as the rate of change of curvatures, need approximately 30 iterations of diffusion smoothing.

While the interfacial positions can be preserved by limiting the diffusion smoothing, the level-set function near the interfaces can deviate from the signed distance function during this process. We have found that this deviation is nearly uniform over the grid points required to calculate interfacial quantities. To remedy this problem, after applying the diffusion smoothing, we compute $|\nabla\varphi|$ at all grid points and determine its average, $\langle|\nabla\varphi|\rangle$, where $|\varphi| < 1\Delta x$, i.e. the region where the level-set function is closest to the distance function after diffusion smoothing, and scale the level-set function with the calculated $1/\langle|\nabla\varphi|\rangle$. After normalization, the diffusion smoothed level-set function again takes the form of the signed distance function. Hereafter, to simplify notations, ϕ, φ and φ^D will be used to denote the order parameter, the

level-set function, and the smoothed level-set function that has been processed by the diffusion smoothing and normalized by $\langle|\nabla\varphi|\rangle$. The combination of the level-set function with diffusion smoothing will be referred to as level-set smoothing.

3.2.2 Preparation of Structures

Three types of structures are employed in this chapter to validate the level-set smoothing method: a sphere, a cylinder and a bicontinuous structure. All structures presented in this chapter are constructed in a nondimensional space, and therefore all measurements of length and time are unitless. A grid spacing of $\Delta x = \Delta y = \Delta z = 1.0$ is employed for simplicity.

Order parameters describing spherical and cylindrical geometries can be constructed analytically using a hyperbolic tangent function. For a spherical particle in a Cartesian grid system, the discretized order parameter, ϕ_{ijk}, where i, j, and k denote the indices for the position, can be constructed as

$$\phi_{ijk} = \frac{1}{2} + \frac{1}{2}\tanh\left(\frac{2\left(r_{ijk} - R\right)}{\frac{1}{2}\delta_{tanh}}\right), \tag{3.7}$$

where

$$r_{ijk} = \sqrt{\left(i - x_c\right)^2 + \left(j - y_c\right)^2 + \left(k - z_c\right)^2}, \tag{3.8}$$

and R is the radius of the spherical particle. The variables x_c, y_c, z_c represent the Cartesian coordinate of the center of the sphere, which is placed at the center of the computational domain. The order parameter defined by Eq. (3.7) will have a bulk value of 0 for the inside of the sphere and 1 for the outside while δ_{tanh} represents the nondimensional interfacial thickness, which is defined as the region where the value of ϕ smoothly transitions between the two bulk values. In this chapter, we used $\delta_{tanh} = 4.0$, which results in about four grid points across the interface and is typical of phase-field simulations. Similarly, a cylindrical tube with an infinite length along

the z-axis can be constructed by Eq. (3.7) with r_{ijk} redefined as

$$r_{ijk} = \sqrt{(i - x_c)^2 + (j - y_c)^2}, \tag{3.9}$$

where x_c and y_c represent the Cartesian coordinate of the axis of the cylinder. To calculate the dynamic interfacial quantities, pairs of spherical particles and cylindrical tubes with different radii were analytically constructed from the order parameters.

While above geometries provide important test cases with well defined analytical solutions to interfacial quantities, the true power of the method is its ability to be applied to a wide range of complex microstructures. For demonstration, we choose a bicontinuous structure resulting from phase ordering [84]. Using the phase-field method, a two-phase bicontinuous structure is simulated via nonconserved Allen-Cahn dynamics. Henceforth, this bicontinuous structure is referred to as the AC structure. A time step of $\Delta t = 0.1$ with $L_\phi = 1.0$ are employed for simplicity. The remaining parameters in the governing equation are $\epsilon^2 = 0.4$ and $W = 0.8$, which lead to an interfacial thickness of $\delta = 4$ and interfacial energy of $\gamma = 0.2$. Since this AC structure is also statistically analyzed in the subsequent chapter, a large computational domain size of $2048 \times 2048 \times 2048$ in a Cartesian-grid system was simulated. Starting from an initial condition consisting of random numbers that vary between $\phi = 0.5 \pm 0.1$ that ensures equal volume fractions of the two phases, the simulation was run until the AC structure underwent sufficient amount of coarsening to achieve self-similarity. Even though the dynamics is nonconserved, the system maintains a $50 : 50$ volume fraction due to its symmetry. The simulation time $t_0 = 600$ is used as a reference simulation time for all analyses presented in this chapter. Figure 3.1b shows the isosurfaces of the AC structure at nondimensional simulation time $t_0 = 600$. As a note, in this chapter, only a cubic region of side length $6.2(S_v^{-1})$ of the AC structure is examined for the validation of the level-set smoothing method.

3.2.3 Calculation of the interfacial quantities with Convective and Advective Method

In order to study the morphology of a complex microstructure, curvatures of the surface, such as the mean and Gaussian curvatures, need to be evaluated. Furthermore, to study the evolution of microstructures, calculations of rate of changes of relevant quantities are necessary to quantify the evolution of interfaces. These dynamic quantities include the normal velocity, which is the rate of displacement of interfaces in the direction normal to the interface, and the rate of changes of mean and Gaussian curvatures (calculated following the interface), which quantify the evolution of local curvatures. In this section, we briefly explain how the mean curvature, H, the Gaussian curvature, K, and the normal velocity, v, can be calculated using the level-set approach. We then introduce two methods, the convective and the advective method, which are used to calculate rate of changes of mean and Gaussian curvatures, DH/Dt and DK/Dt, respectively and defined below. All interfacial quantities are calculated from the smoothed level-set function, φ^D.

Since φ^D takes the form of a signed distance function near the interface, the interfacial quantities, H, K, and v can be evaluated from the derivatives of φ^D using the level-set method [116]. The main advantage of using the smoothed level-set function is that the interfacial quantities can be accurately computed on the Cartesian coordinate without parameterizing the surface of the microstructure. Once an interfacial quantity is calculated at all grid points, the physically meaningful interfacial values are obtained by linear interpolation at the interfacial position where $\varphi^D = 0$. The expressions for H, K, and v can be found in Sethian's book [116] and are included in Appendix A along with the finite differencing methods used to evaluate the spatial derivatives that appear in the expressions. Note that our definition of H varies from [116] by a factor of $1/2$.

We now present the two numerical methods to evaluate DH/Dt and DK/Dt,

each based on a different frame of reference (FOR): Eulerian with fixed FOR and Lagrangian with material FOR. The first approach is the convective method [123]. The convective method uses an Eulerian approach to calculate the Lagrangian derivative D/Dt. For instance, DH/Dt can be expressed in terms of an Eulerian derivative $\partial H/\partial t$ and a gradient, ∇H, as

$$\frac{DH}{Dt} = \frac{\partial H}{\partial t} + \boldsymbol{v} \cdot \nabla H. \tag{3.10}$$

Here, $\boldsymbol{v}$ is the normal velocity vector defined as the product of the normal velocity, v (Eq. (A.9)), and the unit normal vector, $\boldsymbol{n}$ (Eq. (A.3)). The convective method calculates each term on the right hand side of Eq. (3.10) at all grid points, where H and $\boldsymbol{v}$ are computed using the level-set approach. The partial rate of changes of the mean curvature in Eq. (3.10) is an Eulerian derivative and can be discretized as

$$\frac{\partial H(x_i, y_j, z_k, t_1)}{\partial t} = \frac{H(x_i, y_j, z_k, t_2) - H(x_i, y_j, z_k, t_1)}{\Delta t}, \tag{3.11}$$

where t_1 and t_2 are different evolution times, $\Delta t = t_2 - t_1$, and x_i, y_j, and z_k are the coordinates in Cartesian grid, where i, j, and k are the indices associated with grid points along the x, y, and z directions, respectively. Values of $H(x_i, y_j, z_k, t_1)$ and $H(x_i, y_j, z_k, t_2)$ at each grid point are calculated from the smoothed level-set function at t_1 and t_2, respectively, based on Eq. (A.4). The second term, $\boldsymbol{v} \cdot \nabla H$, in Eq. (3.10) is referred to as the convective term and is calculated using a first-order upwind scheme, where the normal velocity vector, $\boldsymbol{v}$, is calculated as $v\boldsymbol{n}$, and the gradient of H is evaluated at t_1, $\nabla H(x_i, y_j, z_k, t_1)$. The convective term provides the correction between the Lagrangian derivative (D/Dt), also known as the convective derivative or the material derivative, and the Eulerian derivative ($\partial/\partial t$), which does not take into account the movement of interfaces. Once the sum of the partial derivative and the convective term is evaluated at all grid points, the interfacial values of DH/Dt are

determined by linear interpolation at the interfacial position where $\varphi^D(t_1) = 0$. The main advantage of the convective method is that the entire calculation is performed at stationary grid points, which circumvents the need to explicitly follow the interfacial movement between time steps.

The second approach for calculating the rate of changes of curvatures is the advective method. Unlike the convective method, the advective method requires the explicit determination of the location of interfaces at two consecutive time steps. The advective method can be viewed as directly calculating DH/Dt and DK/Dt on a FOR that is moving with the interface. The rate of changes of the mean curvature, DH/Dt, can be expressed as

$$\frac{DH}{Dt}(\boldsymbol{x}(t_1), t_1) = \frac{H(\boldsymbol{x}(t_2), t_2) - H(\boldsymbol{x}(t_1), t_1)}{\Delta t}, \tag{3.12}$$

where

$$\boldsymbol{x}(t_2) = \boldsymbol{x}(t_1) + \boldsymbol{v}\Delta t. \tag{3.13}$$

Here, $\boldsymbol{x}(t_1)$ is the interfacial coordinate at reference simulation time t_1; and $\boldsymbol{x}(t_2)$ is the predicted interfacial coordinate of the point $\boldsymbol{x}(t_1)$ at time t_2, which is obtained by displacing $\boldsymbol{x}(t_1)$ by $\boldsymbol{v}\Delta t$ (see Eq. (3.13)). Figure 3.2 shows a schematic representation of the advection of interfacial coordinates, onto which the mean curvature values are interpolated.

While the convective method is more straightforward because the rate of changes of curvatures are computed on stationary grid points, the advective method yields more accurate results as demonstrated below. There are two reasons behind this. As an example, we here consider the calculation of DH/Dt. The first source of error in the convective method is in the term $\boldsymbol{v}\cdot\nabla H$. The convective term requires calculation of ∇H, and the higher order derivative introduces additional numerical errors. The second source of error arises from the calculation of $H(x_i, y_j, z_k, t_2)$ near $\boldsymbol{x}(t_1)$. For an

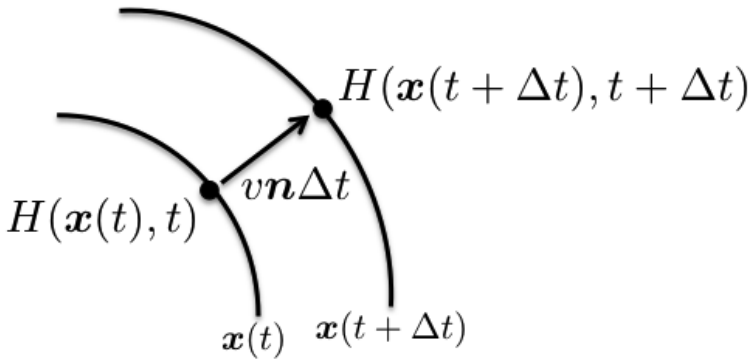

Figure 3.2: A schematic representation of the advection of interfacial coordinates. The variables $\boldsymbol{x}(t)$ and $\boldsymbol{x}(t+\Delta t)$ represent interfacial coordinates at time t and the predicted interfacial coordinates at $t+\Delta t$, which is obtained by advecting $\boldsymbol{x}(t)$ by $v\Delta t$ in the direction of the normal. The values of mean curvatures at t and at $t+\Delta t$ are interpolated onto $\boldsymbol{x}(t)$ and $\boldsymbol{x}(t+\Delta t)$, respectively.

accurate calculation of $H(x_i, y_j, z_k, t_2)$, $\varphi^D(t_2)$ needs to be in the form of the signed distance function. However, if the interfacial displacement between two time steps is large, $\varphi^D(t_2)$ at grid points near $\boldsymbol{x}(t_1)$ may not be a signed distance function (since $\varphi^D(t_2)$ is in the form of the signed distance function only within $3\Delta x$ from $\boldsymbol{x}(t_2)$). Error in $H(x_i, y_j, z_k, t_2)$ leads to inaccuracy in $\partial H/\partial t$. Hence, the accuracy of the convective method quickly deteriorates as the interfacial displacement between two consecutive time steps increases. A detailed study of the errors associated with the calculation of interfacial quantities are presented in the subsequent section.

3.3 Results & Discussion

The following section demonstrates the capability of the proposed level-set smoothing method for calculating various types of interfacial quantities. As mentioned earlier, we aim to achieve (1) accurate calculations of interfacial quantities, (2) minimal displacement of interfaces during the smoothing process, and (3) to demonstrate the

method with complex microstructures. As such, we divided this section into four parts:

- Validation and uncertainty quantification of the level-set smoothing for simple geometries
- Validation of the calculation of rate of changes of curvatures for simple geometries
- Comparison of interfacial locations before and after smoothing for a complex microstructure
- Application of the method to a complex microstructure.

3.3.1 Validation & Uncertainty Quantification of the Level-Set Smoothing for Simple Geometries

Generally speaking, validation of a numerical method can be accomplished by comparing the numerically calculated quantities with corresponding analytical solutions. To carry out such comparisons for the level-set smoothing method, we must compare the numerically calculated interfacial quantities from the smoothed level-set functions with corresponding analytical values. Therefore, we use pairs of spheres and cylinders with different radii (to mimic the morphologies of contracting objects at two different times). The simple geometries of spheres and cylinders are ideal for obtaining analytical values of interfacial quantities and their changes. The construction of these structures using the hyperbolic tangent function, presented in Section 3.2.2, ensures near perfect spherical and cylindrical geometries, minimizing errors in the geometries themselves.

As an initial analysis, we used pairs of spheres and cylinders with $R_1 = 40$ and $R_2 = 38$. Figure 3.3a shows the interfacial profiles of the pair of spherical particles.

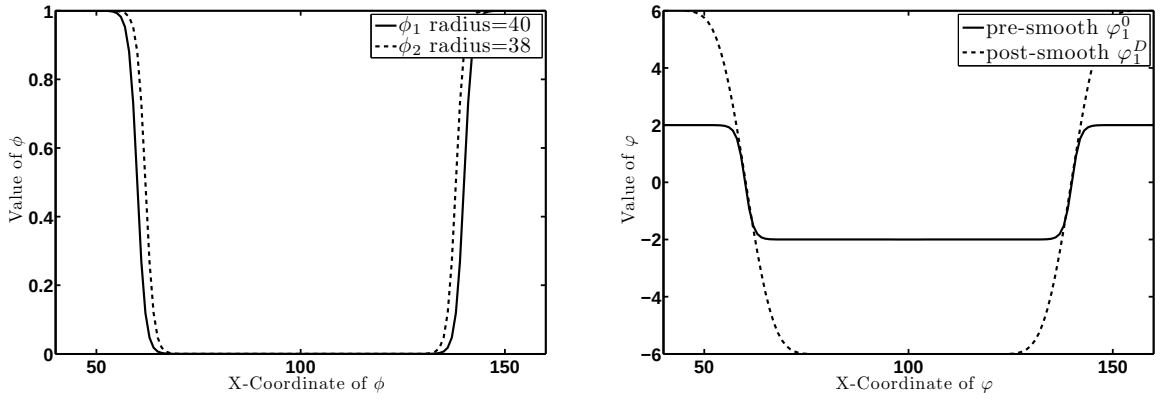

(a) **(b)**

Figure 3.3: (a) A center cut showing the interfacial profiles of the spherical particles of radius 40 and 38 given by ϕ_1 (solid line) and ϕ_2 (dashed line), respectively. The outside of the sphere is defined as $\phi = 1$ and the inside as $\phi = 0$. (b) A center cut showing interfacial profiles of the spherical particle with radius of 40 described by φ_1^0 (solid line), before smoothing, and φ_1^D (dashed line), after smoothing. The outside of the sphere is defined as $\varphi^0 = 2$ and the inside as $\varphi^0 = -2$.

The same smoothing sequence was applied to the four order parameters. Before the smoothing process, we translate the values of the order parameter, ϕ, via

$$\varphi^0 = 4\phi - 2. \tag{3.14}$$

After the translation, the inside and outside the structures are defined as $\varphi^0 = -2$ and $\varphi^0 = 2$, respectively (see Fig. 3.3b). Throughout the smoothing sequence, $\Delta x = \Delta y = \Delta z = 1.0$, $\Delta\tau = 0.1$, $\zeta = 3\sqrt{(\Delta x^2 + \Delta y^2 + \Delta z^2)}$ in Eq. (3.5), and periodic boundary condition was used. The level-set equation is iterated until the maximum $|\varphi|$ reaches $6\Delta x$. Subsequently, the level-set function is processed via diffusion smoothing and is scaled by 0.9 ($\approx \langle|\nabla\varphi|\rangle$ near the interfaces after the diffusion smoothing step) to acquire φ^D, as shown in Fig. 3.3b.

After obtaining the smoothed level-set functions, we calculated various interfacial quantities discussed in Section 3.2.3. For the calculation of dynamic interfacial quantities, the structures with larger radii are considered the reference point at t_1. For this

particular setup, the physical time, Δt, required for the calculation of rate of change quantities can be arbitrarily chosen since it cancels out during the quantification of the fractional error of the numerical calculation with respect to the analytical solution, as discussed below. The numerically calculated interfacial quantities are then compared with the analytical solutions to evaluate the fractional errors according to

$$\epsilon(f) = \frac{f_{numerical} - f_{analytical}}{f_{analytical}}, \tag{3.15}$$

where f is one of the interfacial quantities. The comparison of the numerical calculation with the analytical solution is performed at every vertex that forms the surface mesh of the spheres and the cylinders. Figures 3.4 & 3.5 display the isosurfaces of the spherical particle and the cylinder, respectively, each with radius of 40, colored by the magnitude of fractional errors of various interfacial quantities calculated from ϕ and φ^D.

The grid effect, which manifests itself as rapidly varying errors on the surface, appears for both types of data sets. This effect originates from the grid-anisotropy of the underlying Cartesian grid employed. However, the range of the magnitude of percentage errors (as noted by the color bar range) shows that the level-set smoothing method significantly improves the accuracy of the calculated interfacial quantities, especially for the dynamic interfacial quantities.

The differences in errors from pre-smoothed and post-smoothed data sets do not vary much for the curvatures (as shown in Fig. 3.4a-d and Fig. 3.5a-b, about a factor of 2). However, for the dynamic interfacial quantities, the magnitudes of errors reduce dramatically after smoothing, by as much as a factor of 100, as shown in Fig. 3.4e-j and Fig. 3.5c-f. The large magnitude of errors in the calculated rate of changes of curvatures from pre-smoothed data sets can be explained by identifying the sources of errors for DH/Dt and DK/Dt. Based on Eq. (3.15), with $f = DH/Dt$ for an

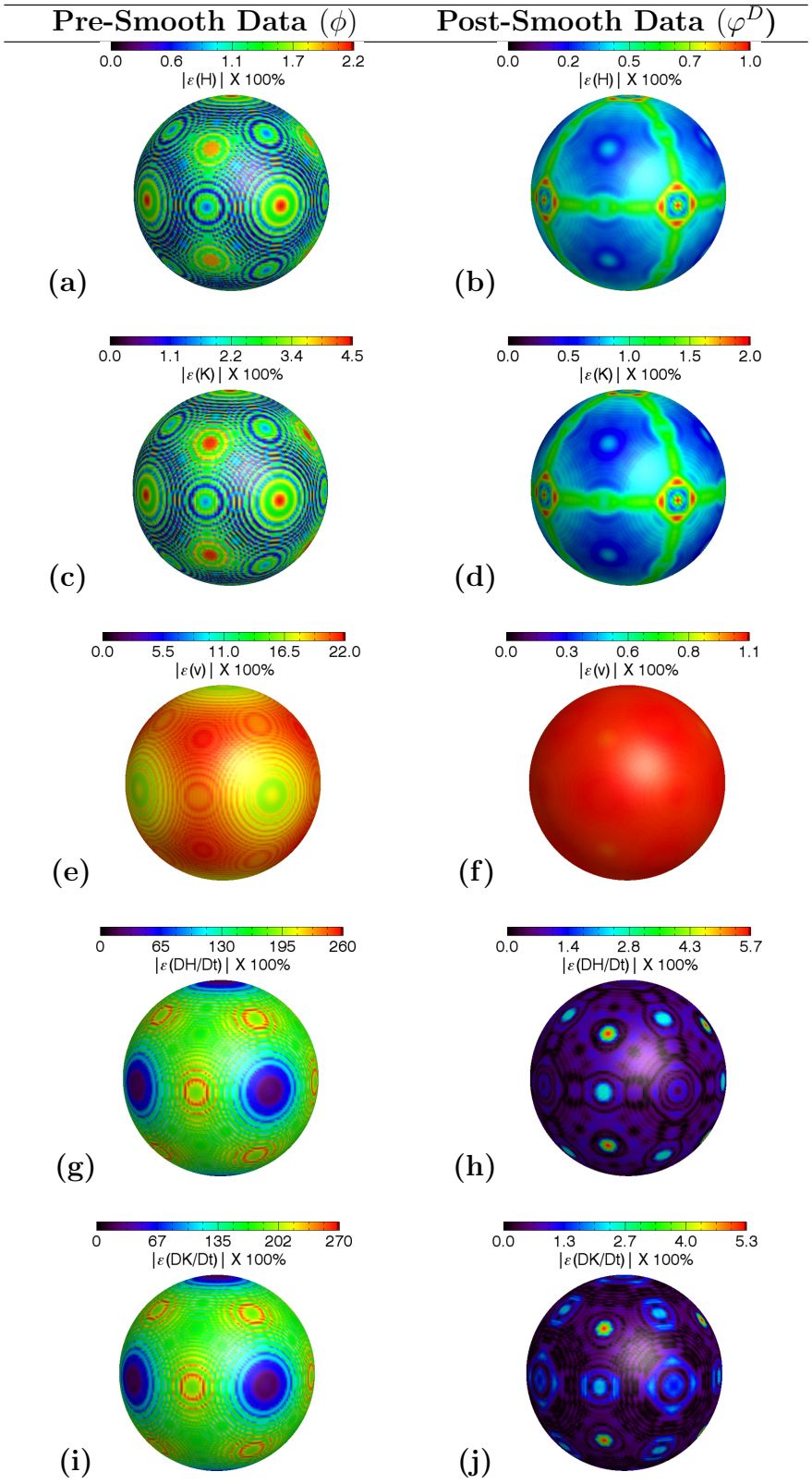

Figure 3.4: The isosurfaces of the spherical particle with $R = 40$ described by (left column) the unsmoothed order parameter, ϕ, (right column) and the smoothed level-set function, φ^D, each colored by the magnitude of errors of (a,b) H, (c,d) v, (e,f) DH/Dt using the advective method.

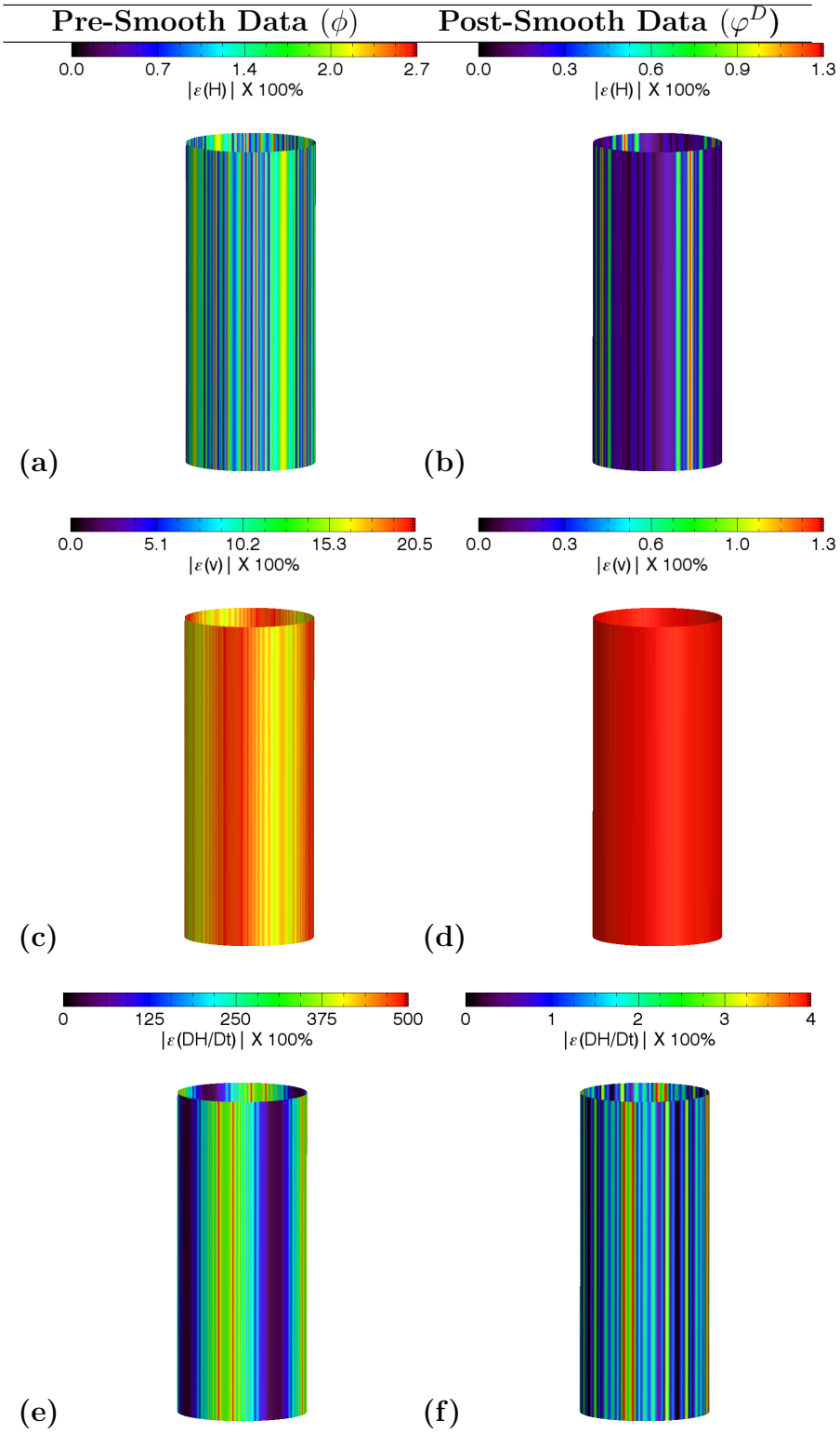

Figure 3.5: The isosurfaces of the cylinder with $R = 40$ described by (left column) the unsmoothed order parameter, ϕ, (right column) and the smoothed level-set function, φ^D, each colored by the magnitude of errors of (a,b) H, (c,d) v, (e,f) DH/Dt using the advective method.

example,

$$\epsilon(DH/Dt) = \frac{\frac{H_2(1+\epsilon(H_2))-H_1(1+\epsilon(H_1))}{\Delta t} - \frac{H_2-H_1}{\Delta t}}{\frac{H_2-H_1}{\Delta t}} = \frac{H_2\epsilon(H_2) - H_1\epsilon(H_1)}{H_2 - H_1}, \tag{3.16}$$

where $\Delta t = t_2 - t_1$, and H_i and $\epsilon(H_i)$ are the interfacial mean curvatures and their associated fractional errors at simulation time t_i ($i = 1$ and 2), respectively. Following Eq. (3.16), the upper-bound error of $|\epsilon(DH/Dt)|$, $sup_{|\epsilon(DH/Dt)|}$, becomes

$$sup_{|\epsilon(DH/Dt)|} = \frac{max\left(|\epsilon(H_1)|, |\epsilon(H_2)|\right)\left(|H_1| + |H_2|\right)}{|\Delta H|} \approx \frac{2|\epsilon(H_1)|}{\frac{|\Delta H|}{|H_1|}}, \tag{3.17}$$

where $\Delta H = H_2 - H_1$ and the right-hand side is based on the assumption that $|\epsilon(H_1)| = |\epsilon(H_2)|$ and $H_1 \approx H_2$ during Δt. Equation (3.17) shows that the upper-bound error is observed when $\epsilon(H_1)$ and $\epsilon(H_2)$ have opposite signs. Moreover, $sup_{|\epsilon(DH/Dt)|}$ is amplified if the difference in quantities, ΔH, is much smaller than the quantities from which the differences are calculated, $H_1 \approx H_2$. Without the application of the level-set smoothing method, interfaces of the pre-smoothed data have noise as a result of low interfacial resolution. The unsmoothed order parameter across the interfaces produces continuous over/under-estimation of curvatures along the surface. Hence, there is a greater probability that $\epsilon(H_1)$ and $\epsilon(H_2)$ have inconsistent signs, which ultimately increases $|\epsilon(DH/Dt)|$. However, after applying the level-set smoothing method, the interfaces are represented by the smoothed level-set function with significantly reduced noise. As a result, the magnitudes of $\epsilon(H)$ and $\epsilon(K)$ are reduced and, more importantly, the signs of the errors are more consistent between time-steps, which leads to error cancellation when computing DH/Dt and DK/Dt.

Tables 3.1 & 3.2 summarize the statistics of the errors for all interfacial quantities calculated from both ϕ's and φ^D's describing the spheres and the cylinders. The maximum error, $max(|\epsilon|)$, is the magnitude of the largest error on the surface mesh of the sphere. The standard deviation of the error based on area, σ_ϵ, is calculated on

	Before Smoothing (ϕ)		**After Smoothing** (φ^D)	
Interfacial Properties	$max(\|\epsilon\|)$ [%]	σ_ϵ [%]	$max(\|\epsilon\|)$ [%]	σ_ϵ [%]
H at radius=40	2.2	1.1	0.98	0.45
K at radius=40	4.5	2.5	2.0	0.91
H at radius=38	2.2	1.1	1.0	0.49
K at radius=38	4.5	2.5	2.1	1.0
v	22	18	1.1	1.1
DH/Dt convective method	833	498	11	6.3
DK/Dt convective method	795	476	13	9.1
DH/Dt advective method	262	147	5.7	0.84
DK/Dt advective method	268	149	5.3	0.89

Table 3.1: Error analysis of the interfacial quantities calculated on two spherical particles with different radii. The variables $max(|\epsilon|)$ and σ_ϵ denote the magnitude of the maximum error among all errors defined at vertices on the surface mesh and the standard deviation of the error based on area, respectively.

the triangulated surface mesh and is defined as

$$\sigma_{\epsilon(f)} = \frac{\sqrt{\dfrac{\sum_{i=1}^{N} \left(f_{numerical} - f_{analytical}\right)^2 A_i}{\sum_{i=1}^{N} A_i}}}{|f_{analytical}|}, \tag{3.18}$$

where the calculated interfacial quantity, $f_{numerical}$, is interpolated at the center of each triangulated element, N is the number of triangulated elements that make up the surface mesh of the spheres and cylinders, and A_i represent surface area of each triangulated element.

The statistics of errors presented in the two tables emphasize the much improved accuracy of the calculation of interfacial quantities after applying the level-set smoothing method, especially with the rate of changes of curvatures (c.f. Tables 3.1 & 3.2, σ_ϵ for DH/Dt and DK/Dt). As expected, the advective method yielded higher accuracy in the calculation of rate of changes of curvatures. Hence, we suggest the use of advective method for calculating the rate of changes of curvatures when meshing of the surface contour is possible. It should be noted that there exist first-order errors

	Before Smoothing (ϕ)		**After Smoothing** (φ^D)	
Interfacial Properties	$max(\|\epsilon\|)$ [%]	σ_ϵ [%]	$max(\|\epsilon\|)$ [%]	σ_ϵ [%]
H at radius=40	2.7	1.6	1.3	0.38
H at radius=38	2.6	1.6	1.3	0.39
v	20	18	1.3	1.3
DH/Dt convective method	1658	894	11	7.7
DH/Dt advective method	503	241	4.0	1.8

Table 3.2: Error analysis of the interfacial quantities calculated on two cylindrical tubes with different radii. The variables $max(|\epsilon|)$ and σ_ϵ denote the magnitude of the maximum error among all errors defined at vertices on the surface mesh and the standard deviation of the error based on area, respectively. Error analysis of K and DK/Dt calculations of the cylinder is omitted since their analytical values are zero.

associated with linear interpolation of interfacial quantities to the location of the interfaces. However, we claim that these errors from interpolation are negligible based on the wide variation of $max(|\epsilon|)$ and σ_ϵ values for different interfacial quantities that were interpolated to the location of interfaces using the same linear interpolation scheme.

3.3.2 Validation of the Calculation of rate of changes of Curvatures for Simple Geometries

Our next step was to identify the effects of the size of the particles and the displacement of interfaces between time-steps on the magnitude of errors associated with the calculation of DH/Dt and DK/Dt. In this section, we considered only structures with spherical geometries. In order to conduct this parametric study, multiple sets of spherical particles with varying R_1 values (10, 20, 30, 40 and 50) and $R_2 = R_1 - |\Delta R|$ values, where $1 \leq |\Delta R| \leq 4$, are created from the hyperbolic tangent function (see Section 3.2.2). After obtaining the smoothed level-set functions (by using the same smoothing sequence presented in Section 3.3.1), we calculated DH/Dt and DK/Dt using the advective method and analyzed the statistics of their respective errors. Figure 3.6 shows the plots of maximum error, $max(|\epsilon|)$, and standard deviation of error

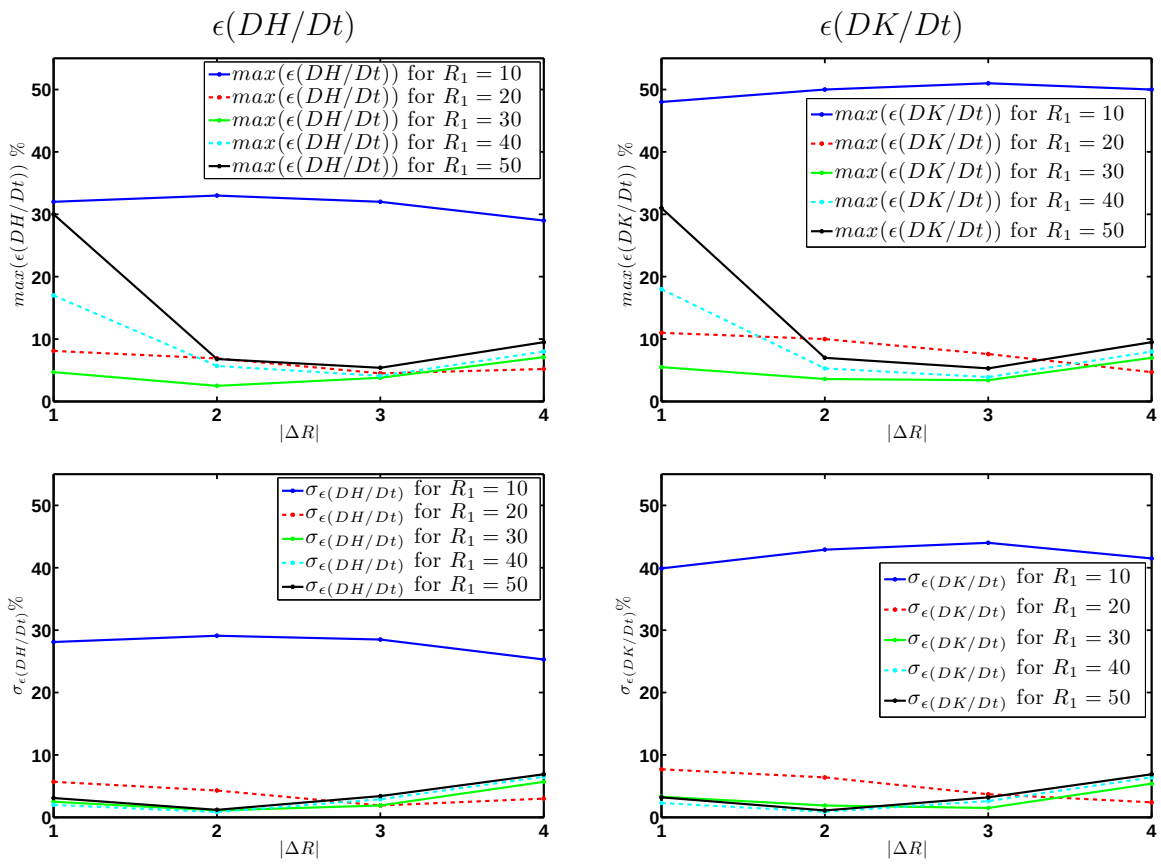

Figure 3.6: The maximum error, $max(\epsilon)$, and the standard deviation of error, σ_ϵ, of DH/Dt (left column) and DK/Dt (right column) as a function of interfacial displacement, $|\Delta R|$, for different particle sizes. The error plots show that $|\Delta R|$ values between two and three are optimal for computing rate of changes of curvatures.

based on area, σ_ϵ, associated with calculating DH/Dt and DK/Dt as functions of interfacial displacement, $|\Delta R|$, for different R_1 values.

We find that $|\Delta R| = 2$ or 3 (interfacial displacement of about two or three grid points) is optimal for computing the rate of change quantities. The large magnitude of $\epsilon(DH/Dt)$ and $\epsilon(DK/Dt)$ for the smallest particle, $R_1 = 10$, results from the fact that as the radius of the particle approaches to the thickness of the diffuse interface, $\epsilon(H)$ and $\epsilon(K)$ values become large. For $R_1 = 20$ (five times the interfacial thickness), the errors were comparable to the cases with larger radius. Therefore, DH/Dt and DK/Dt calculated on interfaces with radii of curvatures greater than five times the

interfacial thickness should yield sufficiently accurate results. As a note, further error analysis showed that H, K and v (normal velocity) can be accurately calculated on interfaces with radii of curvatures greater than four times the interfacial thickness.

3.3.3 Comparison of Interfacial Locations Before and After Smoothing for a Complex Microstructure

For complex morphologies with spatially varying curvatures, such as the AC structure, a direct comparison to known solutions cannot be made. Therefore, an alternative approach to validating a smoothing method is necessary. Here, we will examine the position of the interfaces before and after the smoothing process to determine how the level-set smoothing method alters the surface morphology.

Preservation of the interfacial location during a smoothing process is important, especially for complex morphologies that often have fine features as well as coarse ones. Even if the calculated curvature values appear to be smooth when plotted on the surface of a structure, if the interfacial shifts are significant during data processing, the calculated curvature values will not accurately represent the morphology and the topology of the original structure. In addition, if the shifts of the interfaces caused by a smoothing process is greater than the interfacial displacement due to microstructural evolution, the rate of change calculations become meaningless. Therefore, an effective smoothing method must demonstrate that it can preserve the interfacial location sufficiently during the smoothing process.

The level-set smoothing method was applied to convert the order parameter, ϕ, from the phase-field simulation that describes the AC structure to the smoothed level-set function, φ^D. The same sequence of smoothing with the same set of parameter values as in Section 3.3.1 were employed. We then calculated the interfacial quantities and plotted the values on the surface of the structure to ensure that the calculated quantities are smooth, as shown in Fig. 3.7.

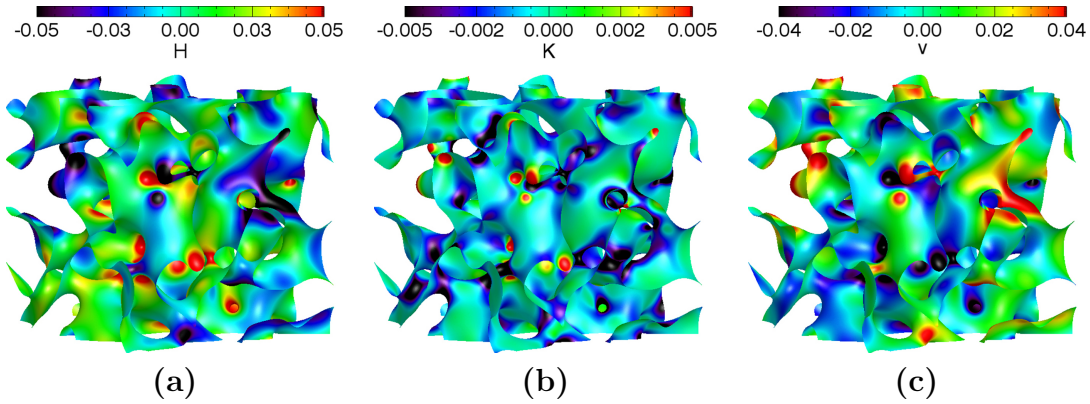

Figure 3.7: Isosurfaces of the AC structure colored by a) the mean curvature, b) the Gaussian curvature, c) the normal velocity calculated from the rate of changes of the smoothed level-set functions.

In order to visualize the effect of the smoothing scheme on the interfacial locations, the contour lines (interfacial locations) obtained at $\phi = 0.5$ and $\varphi^D = 0$ are compared, as shown in Fig. 3.8. The overplots reveal a general overlap of the two contours of the interfaces from the pre-smoothed and the post-smoothed data, indicating that the level-set smoothing preserves the location of the interfaces for most interfaces for most interfaces. At surface patches with very high curvatures (where the radii of curvatures are comparable to the interfacial thickness), there are slight shifts in the two contour lines obtained from ϕ and φ^D (see inset (a) for a magnified image of two regions with notable shifts). However, these regions are confined to small volumes of the entire structure and should not affect the overall results when statistically examined. In addition, these small shifts occur in regions where the interfacial thickness is comparable to the radius of curvature of the interface. Thus the phase-field calculation is under resolved at these points and these areas should not be included in the calculations.

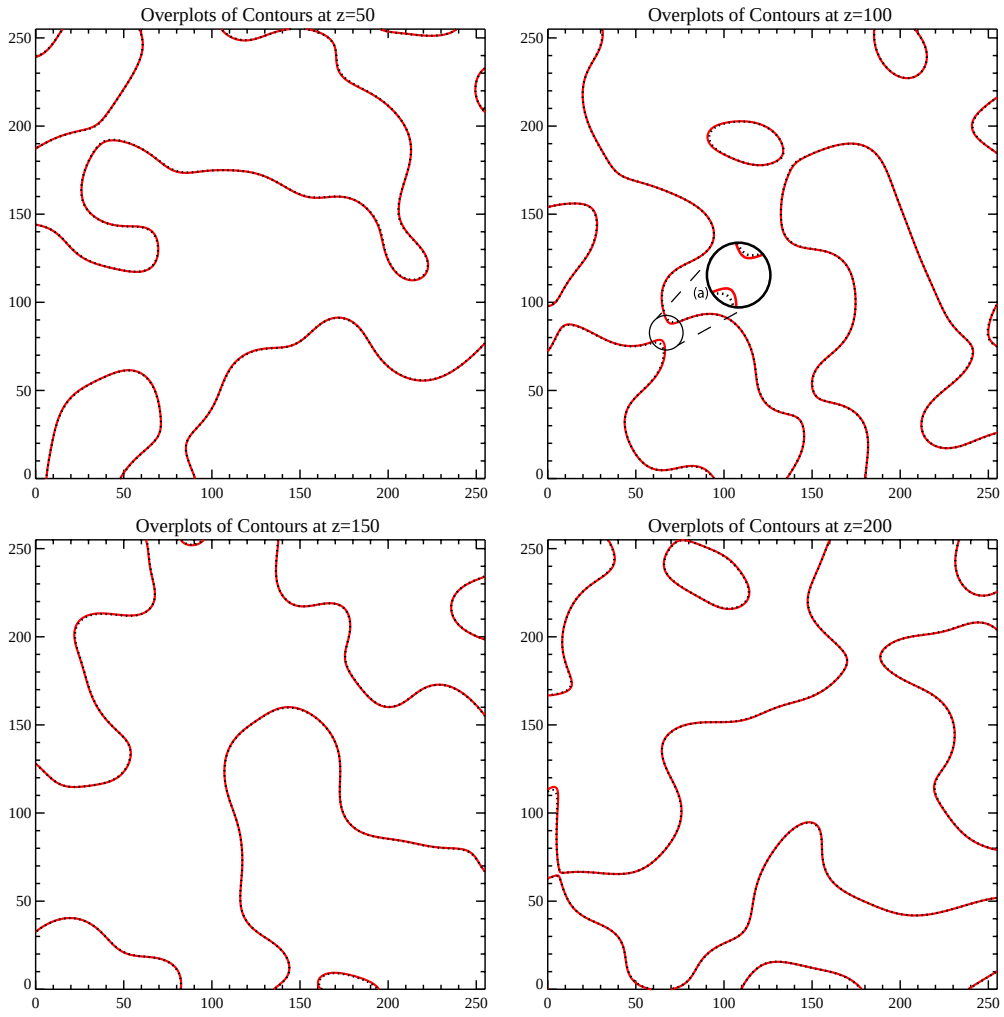

Figure 3.8: Overplots of the interfacial contour lines of the AC structure described by the order parameter, ϕ, (solid red line) and the smoothed level set function, φ^D (dotted black line). The contour lines are obtained on the x-y planes of the AC structure at different z values. Two contours are generally coincident except in the very high curvature regions where the radii of curvatures are comparable to the thickness of the diffuse interface, as shown in inset (a).

3.3.4 Application of the Method to a Complex Microstructure

We have thus far demonstrated the level-set smoothing method's capability to smooth the interfaces with minimal motion of the interfaces so that interfacial quantities are accurately calculated. We also found that the errors associated with rate of change quantities are minimized when the interfacial displacement between time steps is about two to three grid points. Unlike the shrinking sphere, the AC structure possesses spatially dependent mean curvatures and rate of changes, where some interfaces are evolving faster than others. Therefore, in order to maintain this range of interfacial displacement, it is necessary to take different Δt that depends on the normal velocity.

For the AC structure, the normal velocity, v, is proportional to the mean curvature [84],

$$v = -MH, \tag{3.19}$$

where M is a proportionality constant as a function of L_ϕ and ϵ^2 of the Allen-Cahn equation, Eq. (2.12). Therefore, to implement a multiple time-differential size to calculate DH/Dt and DK/Dt of the evolving AC structure, one only needs to consider the local mean-curvature values at the interface. First, we group the surface patches of the structure at simulation time t_0 based on their mean-curvature values, and then we determine the required time-step, Δt, for each curvature group, such that all surface patches would be displaced two to three grid points except for the low curvature regions (as explained below). If we assume that the individual surface patches of a microstructure can be approximated as spherical patches with varying radii, then we can substitute $v = dR/dt$ and $H = 1/R$ in Eq. (3.19). After integration, one obtains

$$\Delta t = \frac{R(t_0 + \Delta t)^2 - R(t_0)^2}{-2M} \tag{3.20}$$

where $R(t_0)$ is the inverse of the mean curvature of a surface patch at time t_0 and $R(t_0 + \Delta t)$ is the corresponding value after Δt. Table 3.3 lists the curvature range, $R(t_0)$, $R(t_0 + \Delta t)$, and the corresponding Δt for each group of surface patches. For each curvature group, $R(t_0)$ is the reciprocal of the $|H|$ value at the lower end of the curvature range in each group. The time-step, Δt, in each group is determined by Eq. (3.20) setting $R(t_0+\Delta t) = R(t_0)-2\Delta x$. Note that even though we assigned Δt values for interfaces with very large curvature values (in this case $R(t_0) < 20$ as discussed in Section 3.3.2), in practice the calculated values on these high curvature surfaces (which constitute only about 5% of the total interfacial area of the AC structure) contain significant errors and should still be discarded for quantitative analysis of the evolution of local curvatures.

For the surface patches with $|H| < 0.025$, we use $\Delta t = 100$. This is because, as Δt increases, the general morphology of the structure can undergo substantial evolution (the low curvature patches are connected with the rest of the structure) and consequently rate of changes of curvature calculations become meaningless. Therefore, one must strike a balance when choosing the appropriate time steps such that rate of change computations are accurate and also physically meaningful. It should be noted that, because the interfacial displacements for the low curvature regions are less than the optimal range, the error in the calculated DH/Dt and DK/Dt at these interfaces maybe substantially larger than those discussed earlier. For example, $max(|\epsilon|)$ and σ_ϵ in DH/Dt for a sphere with $R_1 = 80$ and $R_2 = 79$ are 78% and 7.3%, respectively. However, these large errors are not detrimental to the quantitative analysis of local curvatures since these low curvature regions undergo very small change in curvatures; thus these surfaces do not contribute substantially to the overall microstructural evolution.

Figure 3.9 shows the calculated DH/Dt and DK/Dt of the AC structure described by the smoothed level-set function, φ^D, using a multiple time-differential size based

Range of $\|H\|$	$R(t_0)$	$R(t_0 + \Delta t)$	Δt
$0.2 \leq \|H\|$	5.0	3.0	10.0
$0.1 \leq \|H\| < 0.2$	10.0	7.8	25.0
$0.05 \leq \|H\| < 0.1$	20.0	17.9	50.0
$0.033 \leq \|H\| < 0.05$	30.0	27.9	75.0
$0.025 \leq \|H\| < 0.033$	40.0	37.9	100.0
$0.0125 \leq \|H\| < 0.025$	80.0	79.0	100.0
$\|H\| < 0.0125$	-	-	100.0

Table 3.3: Different evolution times, Δt, are required to ensure displacement of interfaces that yield accurate rate of changes of curvatures of the AC structure ($\Delta x = 1$ is used). The left-hand column shows the range of $|H|$ values that each group of surface patches have while $R(t_0)$ represents reciprocal of the H value at the lower end of the curvature range in each group and $R(t_0 + \Delta t)$ is the corresponding radius value after evolving for Δt. The values of $R(t_0)$ and $R(t_0 + \Delta t)$ are omitted for $|H| < 0.0125$ because the minimum $|H|$ value in this curvature range is zero.

on the Δt's for each curvature group shown in Table 3.3. To compare the values of DH/Dt and DK/Dt obtained from the convective and the advective method, the differences in their corresponding values were also plotted. Figure (3.9c) and f shows that the convective and the advective methods for calculating DH/Dt and DK/Dt agree for most part except in the high curvature regions, where the radii of curvatures are comparable to five times the interfacial thickness. Based on the error analysis performed in Sections 3.3.1 & 3.3.2, we have more confidence in the accuracy of the rate of changes of curvatures calculated with the advective method.

In summary, the above analysis suggests the use of a multiple time-differential size for more accurate calculation of rate of changes of interfacial characteristics of a microstructure with complex morphologies. We note that, while the surface patches of the AC structure were approximated to be spherical for the above analysis, other simple geometries, such as cylinders, can be used for the same analysis. However, the resulting dependence of Δt on H remains the same regardless of the assumed geometry. Furthermore, high curvature regions typically possess geometry similar to a sphere, and therefore the results should be representative of rapidly evolving

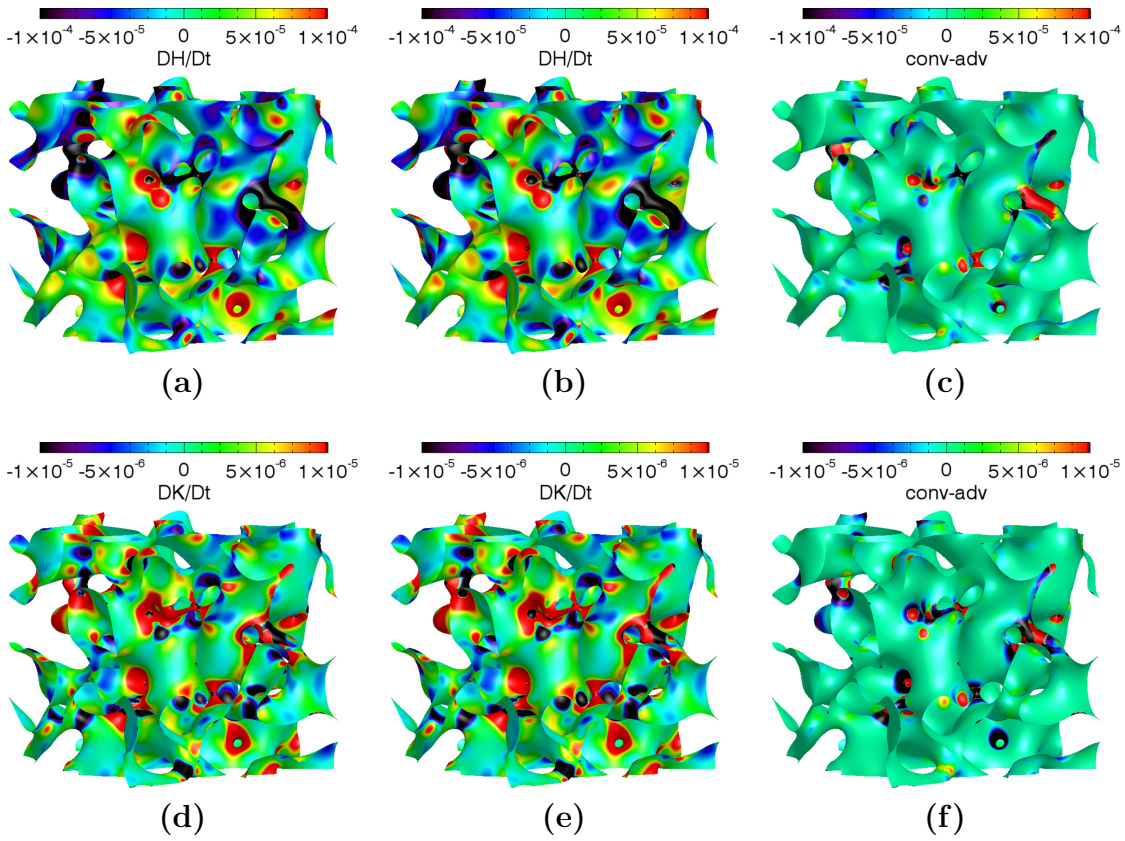

Figure 3.9: Isosurfaces of the AC structure colored by a) DH/Dt using the convective method, b) DH/Dt using the advective method, c) the difference between a) and b), d) DK/Dt using the convective method, e) DK/Dt using the advective method, and f) the difference between d) and e). All DH/Dt and DK/Dt calculations employed a multiple time-differential size, Δt, based on Table 3.3.

features in a morphologically complex microstructure.

3.4 Conclusion

We present an algorithm, "level-set smoothing," that smoothes voxel-based data describing the interfaces with minimal shift in the interfaces so that interfacial quantities can be accurately calculated. The significance of the level-set smoothing method is its ability to be applied to a wide range of complex microstructures obtained from 3-D experimental and computational techniques. The proposed method can be applied to any voxel-based data describing a 3-D two-phase structure so that the interfacial quantities, including their rate of change, can be accurately calculated. These interfacial quantities can then be used to characterize the morphology of a microstructure and its evolution, which is a crucial aspect of 3-D materials science. The level-set smoothing method is a set of sequential data-processing schemes that consists of first generating the signed distance function for the given microstructure using the level-set method, followed by smoothing via diffusion. In addition, this chapter also includes numerical algorithms to calculate various types of interfacial quantities, such as the curvatures and their rate of changes, the latter of which can be calculated by either the convective or the advective methods.

The error analysis of interfacial quantity calculations for simple geometries shows that the method improves the accuracy of the calculated curvatures and their rate of changes of and that the magnitude of the errors are within the acceptable range for the analysis of these quantities. For example, in the case of spheres and cylinders with $R_1 = 40$ and $R_2 = 38$ described by the smoothed level-set functions (with $\Delta x = 1$ and interfacial thickness of 4), the maximum error level is found to be $\sim 1\%$ in H, $\sim 2\%$ in K (for a sphere) and $\sim 4 - 7\%$ in rate of changes of the curvatures when using the advective method. The improvement is especially significant for the rate of change of quantities. We determine that an interfacial thickness less than fifth of the

radius of curvature ensures accurate values of DH/Dt and DK/Dt.

We find that the advective method yields more accurate results for both DH/Dt and DK/Dt than the convective method. The source of the increased error in the convective method is traced to the calculation of gradient and the partial rate of change of, which are not required for the advective method. Furthermore, interfacial displacement of two to three grid points is shown to be optimal for calculating the rate of changes of curvatures. Comparison of the surface contours of the AC structure from the initial order parameter and the post-smoothed level-set function demonstrates that the level-set smoothing method sufficiently preserves the location of the interfaces except for where the curvature is large. Lastly, we have shown that if the evolution of the structure is non-uniform, multiple time differential sizes are suggested to accurately calculate the rate of changes of curvature. The considerations should be given to balance sufficient motion of interfaces for numerical accuracy while preventing major evolution of the microstructure.

CHAPTER IV

Evolution of Interfacial Curvatures of a Bicontinuous Structure Generated via Nonconserved Dynamics

The material presented in this chapter is based on the published manuscript "C.-L. Park, P. W. Voorhees, and K. Thornton. Evolution of Interfacial Curvatures of a Bicontinuous Structure Generated via Nonconserved Dynamics, Acta Materialia 90:182-193, 2015."

4.1 Introduction

As stated in Chapter I, we propose to consider the evolution during coarsening as a consequence of (1) the interfacial velocity induced by diffusion and (2) the resulting evolution of the interfacial curvatures. Examination of the evolution via nonconserved dynamics is the ideal starting point to elucidate the complex dynamics of coarsening since the kinetics is in the simplest form; it is driven by motion by mean curvature and thus the normal velocity is only a function of the local mean curvature. We use a bicontinuous structure simulated via nonconserved dynamics as a test bed to investigate the second aspect of the evolution. In this chapter, we identify interfacial quantities that influence the evolution of local mean curvature.

4.2 Numerical Method

This section briefly describes the phase-field method used to simulate the bicontinuous structure and the numerical algorithms employed to calculate various interfacial quantities.

4.2.1 Preparation of Microstructural Data

In this chapter, we use the bicontinuous AC structure presented in Section 3.2.2 as a test bed. As already discussed in the aforementioned section, the bicontinuous structure is simulated using the phase-field method based on the governing equation for the nonconserved Allen-Cahn dynamics, Eqs. (2.9) and (2.12). To generate sufficient statistics, a large computational domain size of $2048 \times 2048 \times 2048$ in a Cartesian-grid system is employed. Starting from an initial condition consisting of random numbers that vary between $\phi = 0.5 \pm 0.1$ that ensures equal volume fractions of the two phases, the simulation was run until self-similarity was achieved. The simulation time $t_0 = 600$ is used as a reference simulation time for all analyses presented in this chapter. The characteristic length scale of AC structure at this reference simulation time is $S_v^{-1} = 41.0$.

4.2.2 Calculation of Interfacial Quantities

We characterize the interfacial morphology of the AC structure with the mean and the Gaussian curvatures, H and K, respectively, or alternatively with the minor and major principal curvatures, $\kappa_1 = H - \sqrt{H^2 - K}$ and $\kappa_2 = H + \sqrt{H^2 - K}$, respectively. The normal displacement of interfaces is characterized with the interfacial normal velocity, v. On the other hand, the evolution of interfacial morphology is characterized with the Lagrangian rate of changes (in the material frame) of the mean and Gaussian curvatures, DH/Dt and DK/Dt, respectively, or alternatively

with the rate of changes of the principal curvatures, $D\kappa_1/Dt$ and $D\kappa_2/Dt$.

In order to accurately calculate these interfacial quantities, we apply the level-set smoothing method presented in Chapter III. The mean and Gaussian curvatures are calculated first using the level-set approach and the principal curvatures are then computed using the values of H and K. The interfacial velocity is also evaluated using the level-set approach. On the other hand, the rate of changes of curvatures are calculated using the advective method in the moving frame of the reference. To improve the accuracy of the calculation of dynamic interfacial quantities, we employ multiple time-differential sizes, $\Delta\tau$, based on Table 3.3 in Section 3.3.4, such that the smallest and the largest $\Delta\tau$ utilized are 10 and 100, respectively. All interfacial quantities presented in this chapter are scaled by S_v^{-1} at $t_0 = 600$ and the corresponding time scale, $S_v^{-1}/(dS_v^{-1}/dt)$, where dS_v^{-1}/dt is evaluated with $S_v^{-1}(t_1 = 700)$ and $S_v^{-1}(t_0 = 600)$. The time step $\Delta\tau = 100$ is chosen to calculate dS_v^{-1}/dt since most of the interfaces have small mean curvature values, which fall in the lowest curvature group in Table 3.3. In addition, the difference between the values of dS_v^{-1}/dt calculated with $\Delta\tau = 10$ (the shortest time step used to calculate rate of changes of curvatures for the interfaces with the largest mean curvature values) and $\Delta\tau = 100$ is only about 4%.

4.3 Procedures for Analysis

This section briefly explains the various techniques employed to analyze the morphologies and their evolution of the AC structure.

4.3.1 Analysis of the Overall Evolution Using a Statistical Approach

Statistical analysis quantifies the overall morphology of the AC structure and its evolution. For this analysis, the entire structure is examined. We apply two statistical characterization techniques: the interfacial shape distribution (ISD) superimposed

with average curvature velocity arrows and the probability contour map of rate of changes of mean curvature as a function of H and of H and K.

The interfacial shape distribution (ISD) is a probability distribution defined in the principal curvature space. The background on the ISD are presented in Section 2.1.2. Figure 4.1 shows the ISD map defined in the principal curvature space with isolines of constant net curvature and the $H = (\kappa_1 + \kappa_2)/2 = 0$ line. The $H = 0$ line (red) represents symmetric saddle-shaped interfaces. In addition, the isolines of constant net curvature (green), $d = \left(\left(\kappa_1^2 + \kappa_2^2\right)/2\right)^{1/2}$, that are farther away from the origin of the ISD represent interfaces with higher net curvatures. Labels 1 through 4 mark the four regions (quadrants) of the ISD that describe different interfacial morphologies. Regions 1 and 4 represent elliptic interfaces and regions 2 and 3 represent saddle-shaped (hyperbolic) interfaces.

To understand how, on average, the morphologies of the interfaces with the same principal curvatures evolve, we calculate the average velocity in the curvature space, $\boldsymbol{v}_{\boldsymbol{\kappa}}$:

$$\boldsymbol{v}_{\boldsymbol{\kappa}} = \langle D\kappa_1/Dt \rangle_{\kappa_1,\kappa_2} \hat{\kappa}_1 + \langle D\kappa_2/Dt \rangle_{\kappa_1,\kappa_2} \hat{\kappa}_2, \tag{4.1}$$

where $\langle D\kappa_1/Dt \rangle_{\kappa_1,\kappa_2}$ and $\langle D\kappa_2/Dt \rangle_{\kappa_1,\kappa_2}$ are the area-averages of the rate of changes of principal curvatures of all interfaces with given κ_1 and κ_2, and $\hat{\kappa}_1$ and $\hat{\kappa}_2$ are the unit vector on the principal curvature space. The vector, $\boldsymbol{v}_{\boldsymbol{\kappa}}$, is represented as arrows superimposed on the ISD (termed "average curvature-velocity arrows"). The direction of the curvature velocity arrow is determined by the direction of $\boldsymbol{v}_{\boldsymbol{\kappa}}$ and the length of the arrow is representative of $|\boldsymbol{v}_{\boldsymbol{\kappa}}|$.

The second characterization technique is the probability contour map. The evolution of mean curvature is statistically characterized by the probability distribution, $P_1(H, DH/Dt)$, defined as

$$P_1(H, DH/Dt) = \frac{A_1\left(H, DH/Dt\right)}{A_T}, \tag{4.2}$$

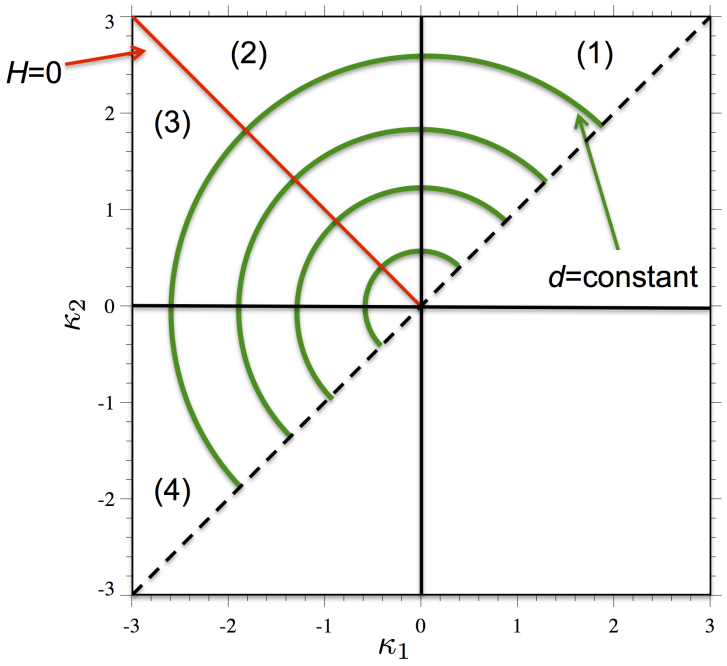

Figure 4.1: The ISD map defined in the principal curvature space with isocurves of constant net curvature d (green) and the $H = 0$ line (red). Labels 1 through 4 mark the four regions (quadrants) of the ISD that represent different interfacial morphologies.

where $A_1(H, DH/Dt)$ is the total surface area of all interfaces with given H and DH/Dt and A_T is the total surface area of the microstructure. This is numerically evaluated by summing interfacial areas that have mean curvature and its rate of change within the range of $H^i \pm \Delta H/2$ and $DH/Dt^i \pm \Delta DH/Dt$ / 2, where H^i and DH/Dt^i are the center values of the i-th bin, and ΔH and $\Delta DH/Dt$ are the bin sizes in H and DH/Dt, respectively. Additionally, to investigate the role of K, which together with H determine the interfacial morphology, in the evolution of mean curvature, we calculate the probability distribution, $P_2(H, K, DH/Dt)$, defined as

$$P_2(H, K, DH/Dt) = \frac{A_2\,(H, K, DH/Dt)}{A_T}, \tag{4.3}$$

where $A_2(H, K, DH/Dt)$ is the total surface area of all interfaces with given H, K, and DH/Dt. This is numerically evaluated in the similar manner described above.

4.3.2 Analysis of Local Morphologies and Their Evolution

To gain insights into the local morphological characteristics and their evolution of the AC structure, we visualize the interfacial quantities with shades of colors on the isosurfaces of the structure. For this analysis, we examine a cubic region of side length $6.2(S_v^{-1})$ of the AC structures. The relationships between the mean curvature and its rate of change is examined through the comparison of the isosurfaces colored with H and DH/Dt.

4.4 Results & Discussion

4.4.1 Overall Morphologies and Their Evolution

The ISD of the AC structure in a scaled principal curvature space is shown in Fig. 4.2 (both plots show the same ISD, and the arrows superimposed on the ISD are discussed below). It shows that the most of the distribution is in the regions 2

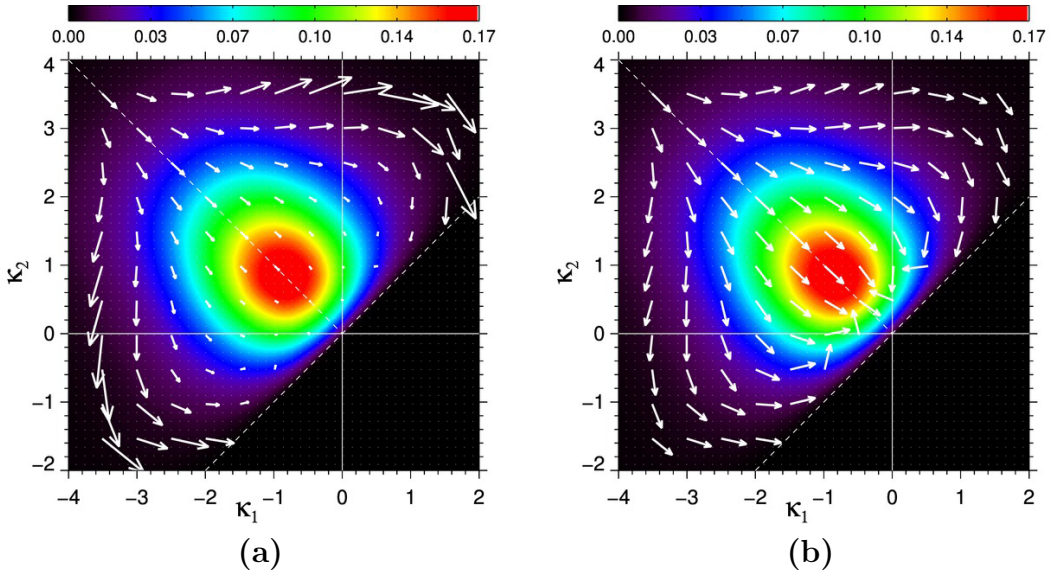

Figure 4.2: ISD of the AC structure superimposed with (a) the average curvature-velocity arrows, which represent the average velocity in curvature space, $\boldsymbol{v}_{\boldsymbol{\kappa}}$, and (b) the normalized average curvature-velocity arrows, which represent the normalized average velocity in curvature space, $\boldsymbol{v}_{\boldsymbol{\kappa}}/\left|\boldsymbol{v}_{\boldsymbol{\kappa}}\right|$.

and 3 of the ISD, which indicates that the majority of interfaces are saddle-shaped. The symmetry of the ISD about the $H = 0$ line ($\kappa_1 = -\kappa_2$) is a consequence of the 50:50 volume fractions of the phases of the AC structure, the steady-state structure arising from nonconserved dynamics. Note that the equal volume fractions alone are not sufficient for achieving the symmetry of the ISD about the $H = 0$ line; in the case of the AC structure, the symmetry between the two phases is ensured by the dynamics and the initial condition that do not bias either of the phases.

Figure 4.2a shows the average curvature-velocity arrows on the ISD, which represent the velocity (including the magnitude) in curvature space, $\boldsymbol{v}_{\boldsymbol{\kappa}}$ in Eq. (4.1). Figure 4.2b is presented to show the direction of the curvature velocity by plotting the normalized average curvature-velocity arrows, $\boldsymbol{v}_{\boldsymbol{\kappa}}/\left|\boldsymbol{v}_{\boldsymbol{\kappa}}\right|$, as it is difficult to show the direction in Fig. 4.2a when the value of $\boldsymbol{v}_{\boldsymbol{\kappa}}$ is small. The average curvature-velocity arrows demonstrate that the magnitude of $\boldsymbol{v}_{\boldsymbol{\kappa}}$ generally increases the net curvature (as evident by the longer arrows away from the origin than near the origin). This

implies that highly curved interfaces of the AC structure are rapidly changing their interfacial morphologies during coarsening, as expected.

Figure 4.2b shows that the normalized average curvature-velocity arrows near the peak of the distribution (within the green color contour) point toward either toward the origin or toward the $\kappa_1 = \kappa_2$ line, indicating that the majority of interfaces are flattening. However, there are few arrows far from the origin of the ISD and the $H = 0$ line that point toward the direction that increases the net curvature. This tendency indicates that some of highly curved interfaces are increasing their net curvatures during coarsening, even though the overall net curvature decreases (or alternatively, the characteristic length scale increases).

This phenomenon is not unlike those observed in coarsening in particulate systems. In a system of spherical particles, the average particle size increases only by disappearance of small particles. These particles, which are smaller than the critical particle size, contract and their curvatures increases in the process. The coarsening thus proceeds by two concurrent processes: smaller particles increasing their net curvatures, evolving towards topological singularity (disappearance), and larger particles growing at their expense. An analogy can be drawn for the bicontinuous structure. In this case, the reduction of the overall net curvature during coarsening is accomplished by : a) some of the small features increasing in net curvatures and evolving toward topological singularity (in this case, pinching), as shown in Fig. 4.3, and b) large features flattening, as shown in Fig. 4.4. Unlike the spherical particle systems, however, some of the small features (with high net curvatures) also flatten when they are surrounded by flatter interfaces. This is the case subsequent to pinching, where the remnant is retracting, as illustrated by Fig. 4.3c-f.

All of these processes can be observed in Fig. 4.2b. The normalized average curvature-velocity arrows that point to higher net curvatures in regions 2 and 3 of the ISD represent the saddle-shaped interfaces increasing their net curvatures as they

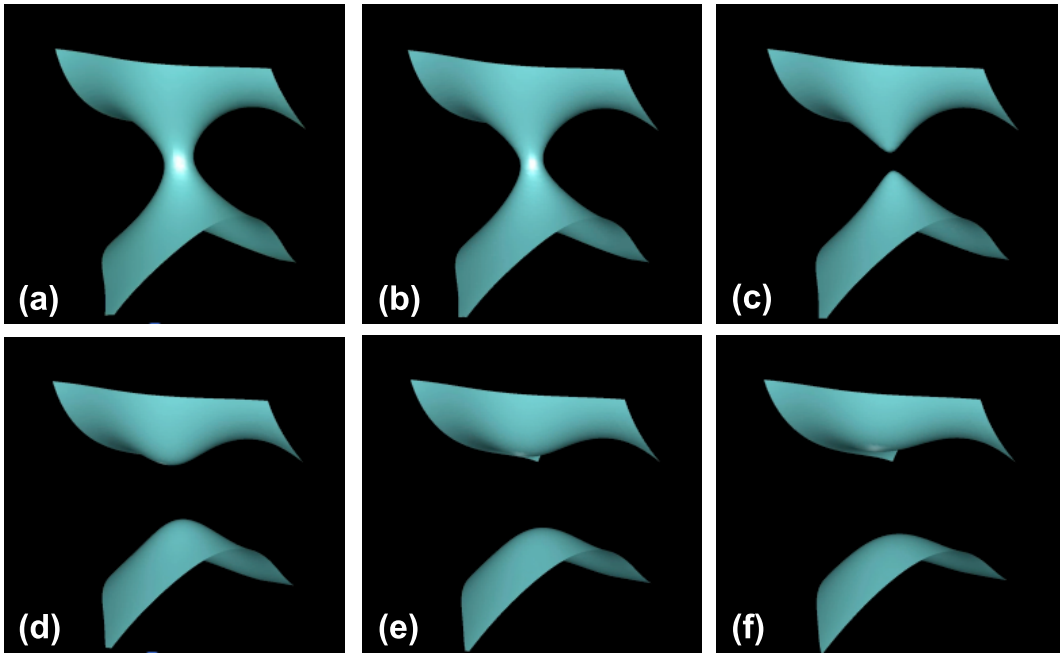

Figure 4.3: Sequential snapshots of the evolution of an interfacial feature in the AC structure undergoing pinching, resulting in a topological singularity, followed by retraction of the remnants of pinching. The corresponding evolution times are (a) $t = 600$, (b) $t = 610$, (c) $t = 625$, (d) $t = 650$, (e) $t = 675$, and (f) $t = 700$.

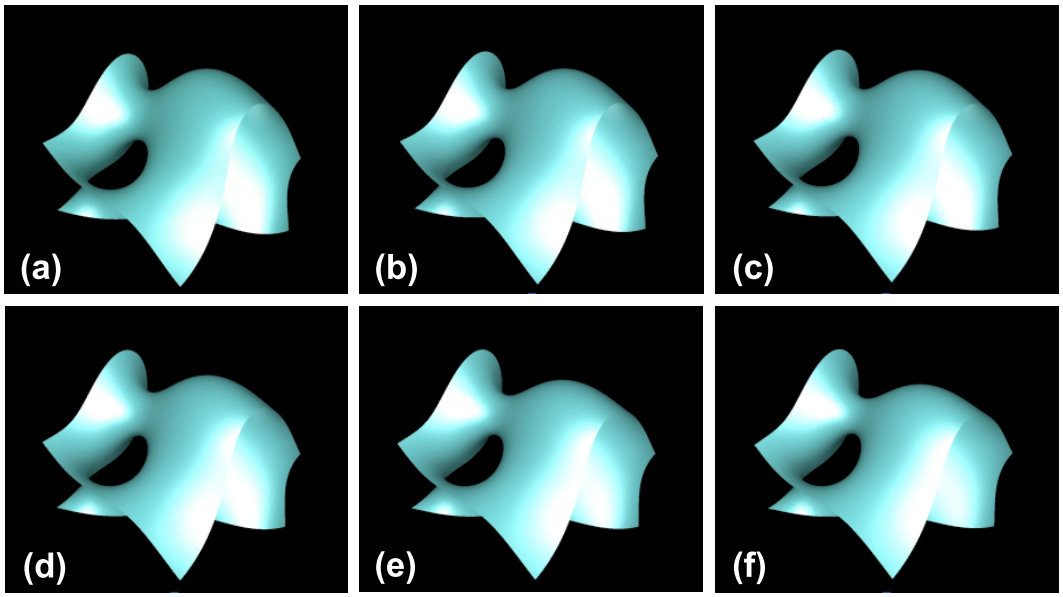

Figure 4.4: Sequential snapshots of the evolution of an interfacial feature in the AC structure undergoing flattening. The corresponding evolution times are (a) $t = 600$, (b) $t = 610$, (c) $t = 625$, (d) $t = 650$, (e) $t = 675$, and (f) $t = 700$.

evolve toward pinching. On the other hand, the nearly spherical interfaces with high curvatures, likely a remnant of pinching, evolve toward the origin (i.e., flattening), as indicated by the arrows pointing toward lower net curvatures in regions 1 and 4 close to the $\kappa_1 = \kappa_2$ line. These results show that topological singularities play a vital role in increasing the length scale of the AC structure during coarsening.

4.4.2 Evolution of Mean Curvature

To gain insight into the evolution of the mean curvature via nonconserved dynamics, we examine the expression for the rate of change of mean curvature, derived from differential geometry:

$$\frac{DH}{Dt} = -(2H^2 - K)v - \frac{1}{2}\left(v_{,11} + v_{,22}\right), \tag{4.4}$$

where $v_{,11}$ and $v_{,22}$ are the second derivatives of the interfacial velocity with respect to the principal coordinates [124]. This expression clearly shows that there are two contributions to the evolution of mean curvatures. In particular, the first term in Eq. (4.4) depends solely on the local curvatures and local normal velocity, while the latter depends on the variation of the velocity. Using Eq. (3.19), Eq. (4.4) can be re-written as

$$DH/Dt = M(2H^2 - K)H + \frac{M}{2}\left(H_{,11} + H_{,22}\right). \tag{4.5}$$

Therefore, for nonconserved dynamics, the first term only depends on the local interfacial curvatures, $M(2H^2 - K)H$, and the second term depends on the variation of mean curvature along the surface, $\frac{M}{2}\left(H_{,11} + H_{,22}\right)$. Note that this term is the surface Laplacian of the mean curvature, and in the absence of the local term, the evolution equation, Eq. (4.5), reduces to the surface diffusion equation, which typically describes the concentration of a chemical species diffusing on a surface. Hereafter, we refer to the first term in Eq. (4.5) as the local term and the second term as the

nonlocal term.

Since M and $(2H^2 - K)$ are positive, the local term of DH/Dt always has the same sign as the mean curvature. Therefore, the local term, which consists of only H and K, do not induce reduction of $|H|$ (the magnitude of H), which would be required to flatten an interface. On the other hand, the nonlocal term of DH/Dt has the form of the surface Laplacian of H, which tends to smooth it in the manner similar to surface diffusion of chemical species. Hence, the nonlocal term drives H toward values similar to the surface's neighbors. Depending on the values of H in the neighborhood, the resulting change may be in the direction of increasing or decreasing $|H|$. However, since this structure has an average mean curvature of zero, the overall tendency is toward decreasing $|H|$.

To verify the role of the local and the nonlocal term of DH/Dt based on Eq. (4.5), we examined the probability contour maps of these quantities, as shown in Fig. 4.5. Figure 4.5a shows the probability distribution of for a given set of DH/Dt and H; the red indicates larger area of interfaces of having the set of DH/Dt and H, and black indicates little or no area. If these two quantities are perfectly correlated, the distribution will collapse to a line. Figure 4.5a indicates some correlation (trend), but with a large dispersion. Similarly, Fig. 4.5b and c are the probability distribution for a given set of the local term of DH/Dt and H and for a given set of the nonlocal term of DH/Dt and H respectively. The probability contour map of the local term of DH/Dt shows a positive and tight correlation between the local term and the mean curvature (i.e., local term always increases $|H|$ and spread as long as the value of K is not large). Note that the probability in Fig. 4.5b is strongly peaked due to the tight correlation, and thus the color bar range is significantly different from Fig. 4.5a and c. In contrast, the probability contour map of the nonlocal term of DH/Dt (Fig. 4.5c) shows, on average, a negative correlation between the nonlocal term and the mean curvature (i.e., the nonlocal term preferentially decrease $|H|$).

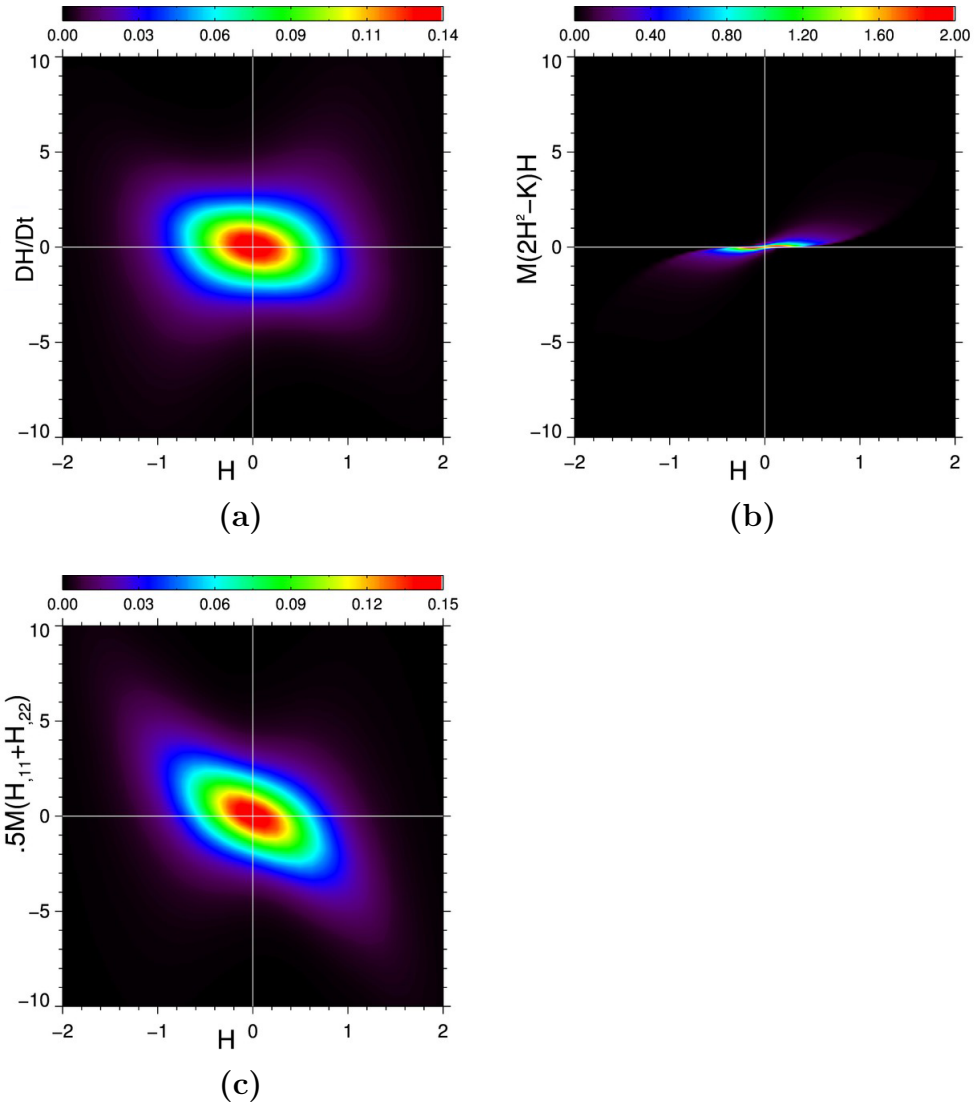

Figure 4.5: Probability contour maps of (a) DH/Dt (b) the local term of DH/Dt and (c) the nonlocal term of DH/Dt as functions of H. These plots confirm that much of the dispersion of DH/Dt for a given H value stems from the nonlocal term of DH/Dt.

Hence the three probability contour maps on Fig. 4.5 demonstrate that the local term of DH/Dt increases $|H|$, while the nonlocal term favors decrease in $|H|$, but with a large dispersion.

We also investigate the statistical dispersions of DH/Dt, as well as its local term and its nonlocal term for a given H value. While the source of the dispersion of the local term is clear, the source of the dispersion in the nonlocal term is not. To examine whether the dispersion originates from its dependence on K, we plot the probability contour map for the nonlocal term for fixed K values, $K = -4, -1, 0,$ and 1, in Fig. 4.6. Interfaces with negative K are those that lie in the regions 2 and 3 of the ISD map ($\kappa_1 < 0$, $\kappa_2 > 0$), as shown in Fig. 4.1. These saddle-like shapes constitute the majority of interfaces in the structure. The distributions of the nonlocal term of DH/Dt are alike in this class of interfaces, which are similar to that of the entire structure. The interfaces with $K = -4$ have similar morphologies as those with $K = -1$ but differ by the magnitude of K. The larger spread in the nonlocal term for interfaces with $K = -4$ indicates that the immediate neighborhood of the interfaces have more diverse interfacial morphologies for saddle-like interfaces with larger $|K|$ than those with smaller $|K|$. The $K = 0$ interfaces have cylindrical shapes. It consists of two populations, one with $\kappa_1 = 0$ and the other with $\kappa_2 = 0$, whose distributions for the nonlocal term of DH/Dt are antisymmetric. The combined distribution is still reminiscent of those of the interfaces with negative K. On the other hand, the distribution for $K = 1$ is significantly different. It consists of two distinct distributions, one belonging to the region 1 of ISD ($\kappa_1 > 0$, $\kappa_2 > 0$), and the other region 4 ($\kappa_1 < 0$, $\kappa_2 < 0$). These interfaces have elliptic shapes, and exhibit a wider spread in the nonlocal term than those with $K = -1$. Nevertheless, it follows the same trend as other populations in that the nonlocal term is negatively proportional to H.

In all of these probability plots shown in Fig. 4.6, the large dispersion in the

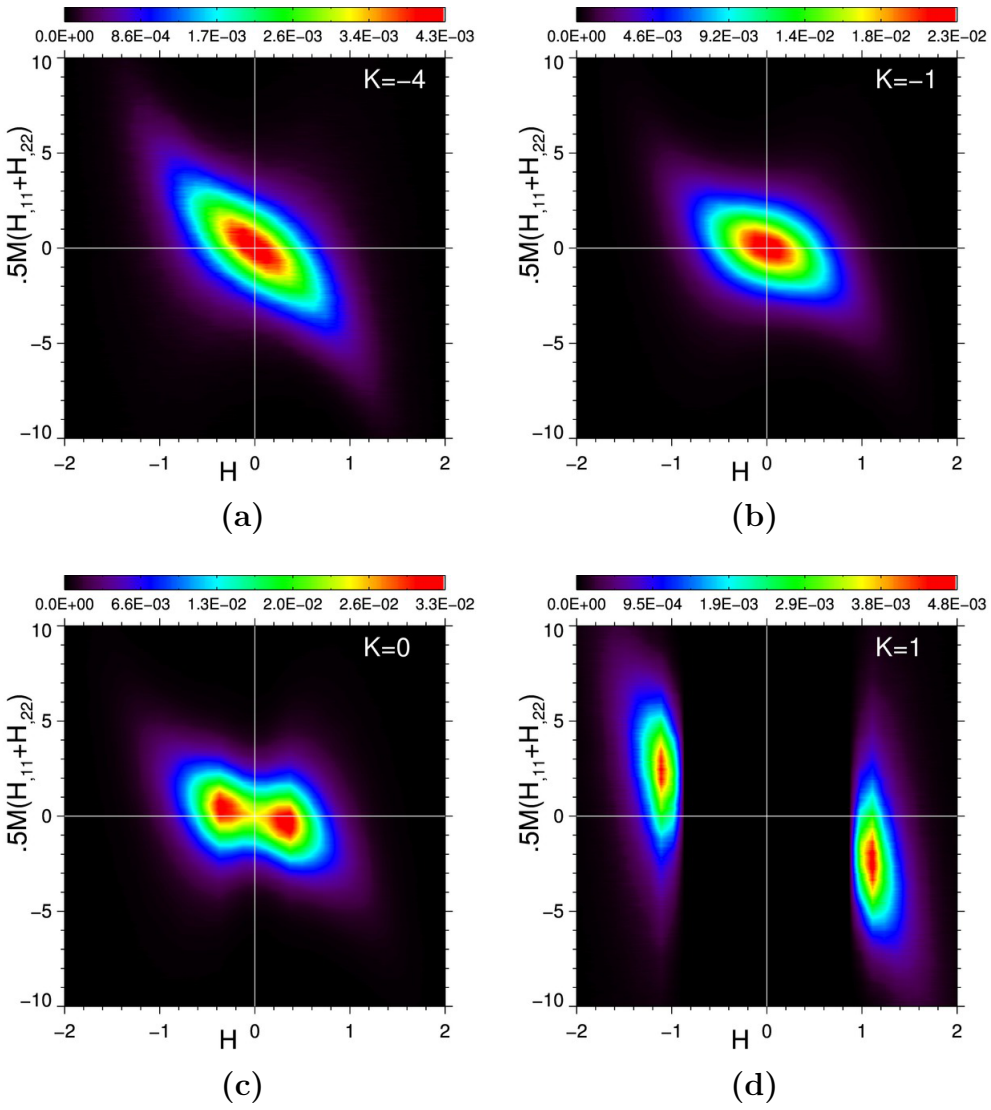

Figure 4.6: Probability contour maps of the nonlocal term of DH/Dt as a function H at K values of (a) $K = -4$, (b) $K = -1$, (c) $K = 0$, and (d) $K = 1$. The large dispersion persists even when the K value is fixed.

nonlocal term persists, indicating that the spread in K for given H is not responsible for the dispersion observed in Fig. 4.5c. Therefore, the origin of the dispersion is truly nonlocal, and it cannot be characterized by the local curvatures or shape of a patch of interface. This nonlocality is a result of the surface diffusion term in the evolution equation for H, Eq. (4.5).

4.4.3 Local Morphologies and Their Evolution

The isosurfaces of the AC structure colored by the mean and the Gaussian curvature values are shown on Fig. 4.7. Consistent with the ISD, the isosurfaces of the AC structure have spatially varying curvatures with interfacial morphologies that continuously vary from elliptical to cylindrical and to hyperbolic (saddle-shaped) interfaces. The isosurfaces also show many evidence of topological singularities in the form of pinching. The numbers marked on Fig. 4.7b highlight regions of interfaces that are about to undergo pinching (labels (1) and (2)) and regions of interfaces that are remnant of pinching (labels (3) and (4)). We find that interfaces that are about to pinch off always have large $|H|(>\sim 5$, which can still be tracked with the given diffuse interface) and negative K values (asymmetric saddle-shaped interfaces) and interfaces that are remnant of pinching have large $|H|$ and positive K values (elliptic interfaces).

We also investigate the local dynamics of interfaces through the calculations of the interfacial velocity and the rate of changes of curvatures, using the AC structure at different simulation times. In the limit where the interfacial thickness is much smaller than the radius of curvature of the interface, the interfacial velocity, v, in Allen-Cahn dynamics is proportional to the mean curvature of the interface. To verify this local dependence of the interfacial velocity, we also calculate the interfacial velocity as a function of mean curvature, the right-hand side of Eq. (3.19). Figure 4.8 shows excellent agreement between the two velocity data, one from the rate of change of the

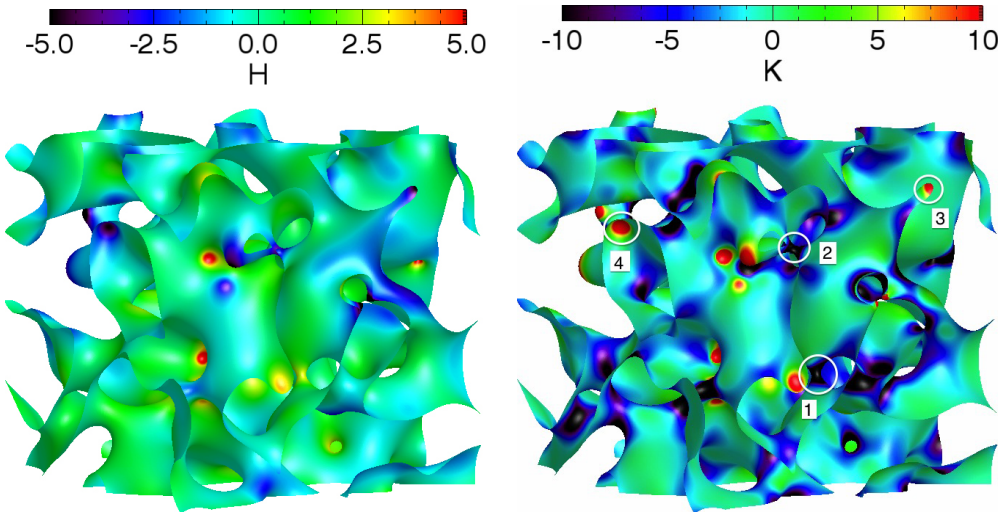

Figure 4.7: Isosurfaces of the AC structure colored by (a) the mean curvature, H, and (b) the Gaussian curvature, K. Labels (1) and (2) are examples of interfaces that are about to undergo topological singularity (pinching), which always have negative K values (saddle-shaped interfaces). On the other hand, labels (3) and (4) are examples of interfaces that are remnant of pinching, which always have positive K values (elliptic interfaces).

smoothed level-set function and the other based on the right-hand side of Eq. (3.19). This agreement demonstrates the accuracy of the method employed to calculate the interfacial velocity from the microstructural data at two closely separated times. This also demonstrates that, for most of the interfacial area, the nonzero interfacial thickness has no effect on the interfacial velocities. Note that, for this comparison only, we use small $\Delta\tau = 10$ to calculate v to capture the dynamics of rapidly evolving interfaces with large mean curvature values.

The evolution of interfacial curvatures, on the other hand, is examined by the calculation of the rate of changes of mean and Gaussian curvatures, DH/Dt and DK/Dt, respectively. Figure 4.9 shows isosurfaces colored with DH/Dt and DK/Dt values. Compared to the interfacial velocity (Fig. 4.8), the values of rate of changes of curvatures exhibit much larger fluctuations throughout the interfaces. More importantly, a direct comparison between the isosurfaces of H and DH/Dt (Figs. 4.7a

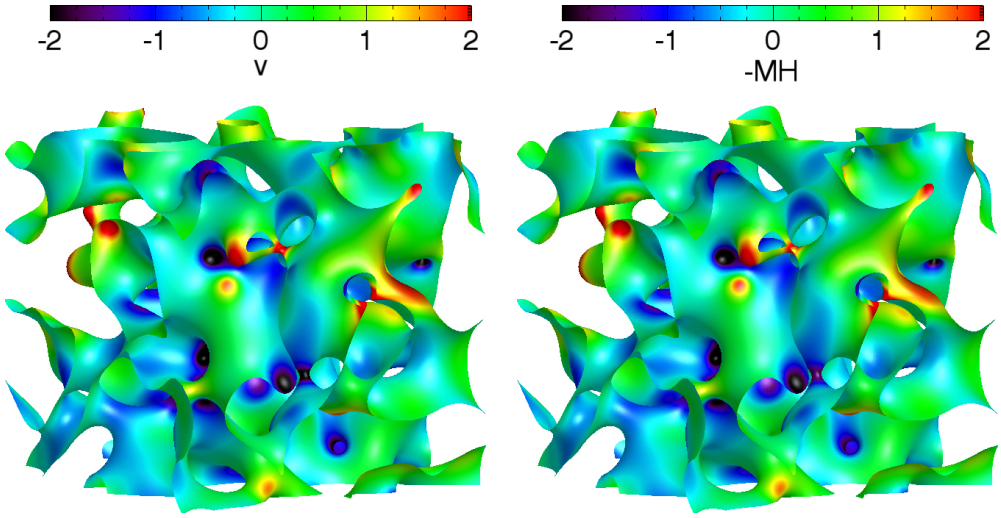

Figure 4.8: Isosurfaces of the AC structure colored by the interfacial velocity calculated from (a) the rate of change of the smoothed level-set function and (b) the mean curvature. The excellent agreement between the two sets of data validates the accuracy of the method employed to calculate the interfacial velocity from the rate of change of the smoothed level-set function.

& 4.9a) reveals a nonlinear relationship between the two quantities, even though the interfacial velocity is linearly proportional to the mean curvature.

Figure 4.10 shows the interfaces colored by H, the local term, and the nonlocal term of DH/Dt in Eq. (4.5). By comparing Figs. 4.10a and b, one can observe that the high (positive) mean curvature region (in red in Fig. 4.10a) has positive value of the local term (in red in Fig. 4.10b). On the other hand, the signs of the nonlocal term (Fig. 4.10c) tend to be opposite of the signs of the mean curvatures, but not always. These results are consistent with the findings obtained from the probability contour maps of H and DH/Dt in Fig. 4.5 in Section 4.4.2.

4.5 Conclusion

In this chapter, we investigate the morphological evolution of a bicontinuous structure simulated via nonconserved dynamics to elucidate the evolution of local mean

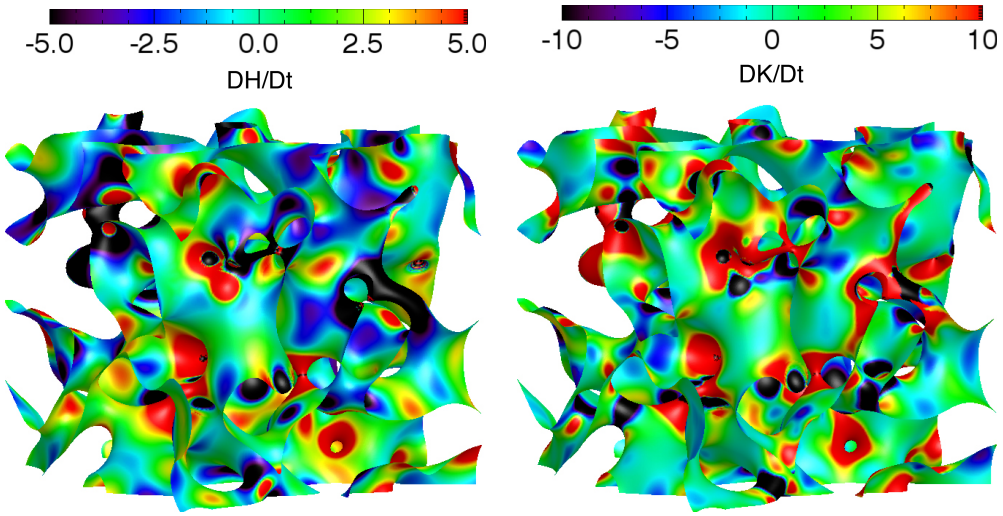

Figure 4.9: Isosurfaces of the AC structure colored by the rate of change of (a) the mean curvature, DH/Dt, and (b) the Gaussian curvature, DK/Dt.

curvature. The AC structure is used as a test bed. The order parameter describing the interfaces of the AC structure is smoothed by the level-set smoothing method so that the interfacial quantities, including dynamic interfacial quantities, could be accurately calculated. These interfacial quantities are then used to quantify the morphology and its evolution to understand the dynamics of coarsening of the bicontinuous structure.

The average curvature-velocity arrows superimposed on the ISD demonstrate that, while the majority of interfaces are flattening (decreasing net curvatures), some of highly curved interfaces are increasing their net curvatures. This is attributed to features evolving toward topological singularity (pinching). The probability contour maps of DH/Dt, its local term, and its nonlocal term confirm that the local term always increases $|H|$, whereas the average value of the nonlocal term decreases $|H|$; the resulting evolution is given by a competition of the two terms. We also find that the large dispersion of DH/Dt for a given H value stems from the nonlocal term of DH/Dt. In addition, we observe that the dispersion in the nonlocal term is not due to variation in K for a given H.

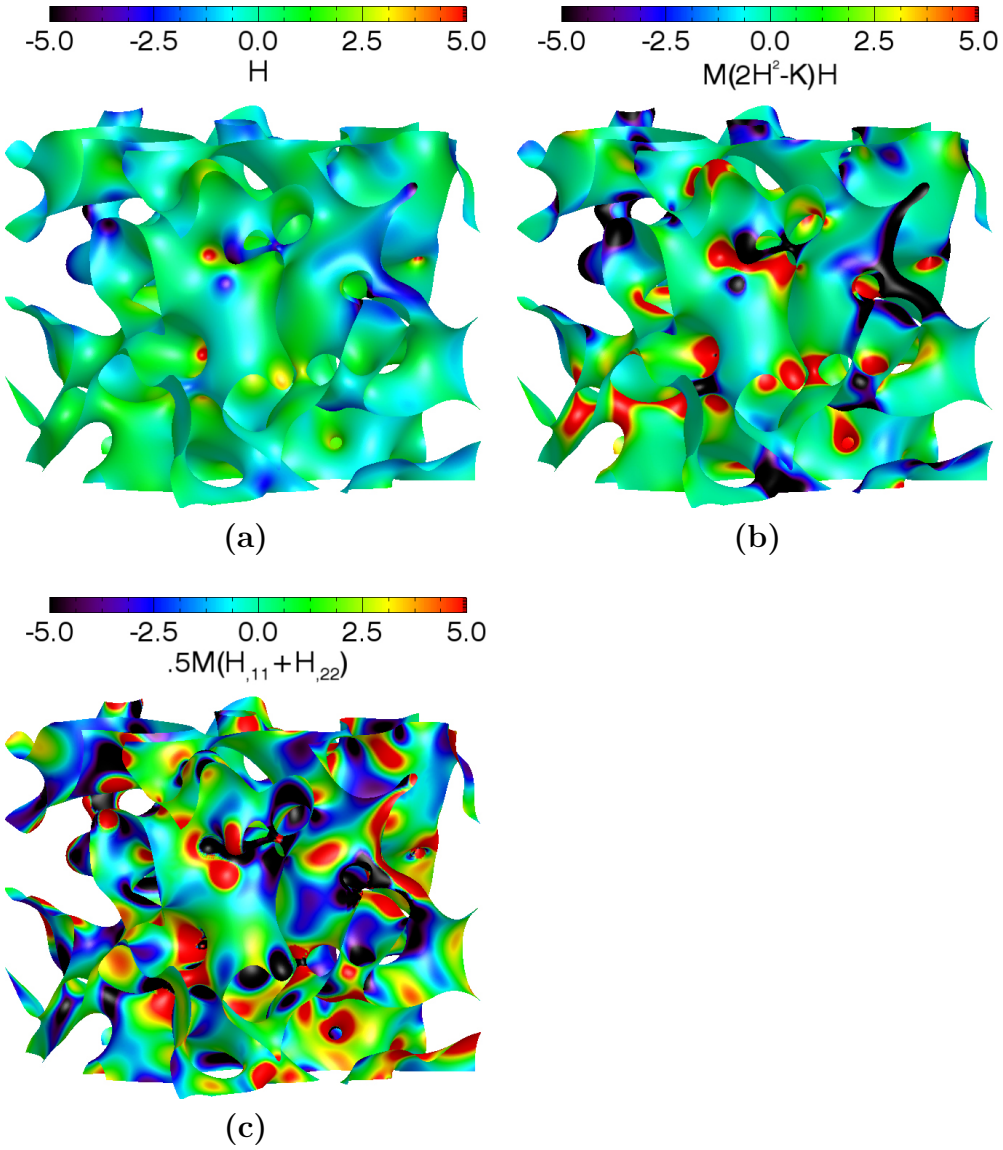

Figure 4.10: Isosurfaces of the AC structure colored by (a) H (b) the local term of DH/Dt, and (c) the nonlocal term of DH/Dt. In agreement with the findings from the probability contour maps shown in Fig. 4.5, the local term always increases the magnitude of H and the nonlocal term favors reduction in the magnitude of H.

CHAPTER V

Coarsening of Complex Microstructures Following Spinodal Decomposition

The material presented in this chapter is based on the manuscript in preparation "C.-L. Park, J.W. Gibbs, P. W. Voorhees, and K. Thornton. Coarsening of Complex Microstructures Following Spinodal Decomposition."

5.1 Introduction

As stated in Chapter I, we propose to consider the evolution as a consequence of (i) the interfacial velocity induced by diffusion and (ii) the resulting evolution of the interfacial curvatures. In the previous chapter, we have investigated the effects of interfacial curvature on coarsening by simulating the evolution of a bicontinuous structure via nonconserved dynamics and the analysis of the interfacial morphologies and their evolution. Building upon this work, in this chapter we examine the coarsening of three complex structures following spinodal decomposition, in which the evolution of interfaces is due to the interfacial-energy-driven bulk diffusion. We first elucidate the dynamics of coarsening by examining the correlation between interfacial velocity and static interfacial properties, namely the mean curvature and the surface Laplacian of mean curvature. We also examine the distribution of interfacial velocities

of interfaces with given principal curvatures. Based on the information gathered from the analysis of interfacial velocity during coarsening, we develop a semi-analytical approach to predict the rate of change of mean curvature, which is then verified against the simulation results.

5.2 Numerical Methods

5.2.1 Preparation of Microstructural Data

In this chapter, we use bicontinuous structures simulated using the phase-field method based on governing equation for the conserved Cahn-Hilliard dynamics, Eqs. (2.9) & (2.13). The simulations are performed with a dimensionless form of the Cahn-Hilliard equation, where we define the dimensionless variables such that $x = \tilde{x}/l$, where l is the scaling length, and $t = \tilde{t}/\tau$, where τ is the associated time scale and the tilde indicates the dimensional variables. We select l such that the grid spacings are $\Delta x = \Delta y = \Delta z = 1.0$ and τ such that $L_\phi = \tilde{L_\phi}\tau/l^2\tilde{W} = 1.0$, where $\tilde{L}$ is the dimensional mobility coefficient and $\tilde{W}$ is the dimensional well-height parameter. A time step of $\Delta t = 0.05$ is employed. A computational domain size of $1024 \times 1024 \times 1024$ in a Cartesian grid system is chosen to generate sufficient statistics for accurate analyses of interfacial morphologies. In the phase-field method, values of ϵ^2 and W in the Cahn-Hilliard equation determine the interfacial thickness, δ. In order to ensure sufficient interfacial resolution, we used $\epsilon^2 = 0.2$ and $W = 0.4$ to obtain $\delta = 4.0$, which results in the interfacial region (defined by ϕ in range 0.1 to 0.9) approximately four-grid-point wide.

In order to examine the influence of overall morphologies on the dynamics of coarsening, we performed three separate simulations with different initial conditions that result in different volume fractions of the phases. The three initial conditions consist of order parameters with average values $\phi_1 = 0.5$, $\phi_2 = 0.4$, and $\phi_3 = 0.3$, each

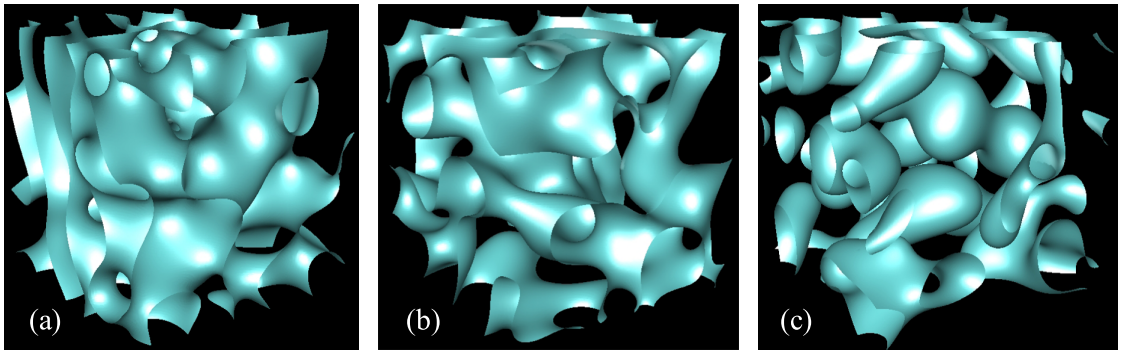

Figure 5.1: Morphologies of (a) the 50:50 CH structure, (b) the 40:60 CH structure, and (c) the 30:70 CH structure at the reference simulation time of $t_0 = 65,000$. The structures in (a) and (b) are bicontinuous, while that in (c) is not bicontinuous. The morphologies shown are in cubic domains with side lengths six times their respective characteristic length scales, S_v^{-1}.

with a random noise of amplitude 0.1. These initial conditions result in bicontinuous structures with 50:50 and 40:60 volume fractions of the phases, and a nonbicontinuous structure with 30:70 volume fractions of the phases. Since the Cahn-Hilliard equation is conserved, the volume fractions of the phases remain constant throughout their evolution.

The three structures were evolved for dimensionless simulation time of $t_0 = 65,000$, which is sufficient to produce self-similar structures for the 50:50 and 40:60 volume fractions [42]. Hereafter, these simulated structures are termed 50:50, 40:60, and 30:70 CH structures, respectively. As a note, the self-similar morphology of the structure with the 30:70 volume fraction should be a polydisperse spherical system, as suggested by [42]. Therefore, the 30:70 CH structure is not self-similar, but rather evolving toward one consisting of spherical particles. Figure 5.1 shows cubic portions of the three CH structures, each with side length $6S_v^{-1}$, where S_v^{-1} is the inverse of surface area per unit volume, which is employed as the characteristic length scale.

5.2.2 Calculation of Interfacial Quantities

Interfacial quantities can be classified into three categories: static local properties, static nonlocal properties, and dynamic quantities. The static local properties include the mean curvature, H, the Gaussian curvature, K, the two principal curvatures, $\kappa_1 = H - \sqrt{H^2 - K}$ and $\kappa_2 = H + \sqrt{H^2 - K}$. We also evaluate the net curvature, $d = \sqrt{\left(\kappa_1^2 + \kappa_2^2\right)/2}$, which measures the overall bend of the interface and reduces to $1/R$ in spherical geometry [43]. The static nonlocal property we examine is the surface Laplacian of mean curvature, $\Delta_S H$, which describes the local variation of H. The three dynamic quantities we examine are interfacial velocity, v, the rate of change of mean curvature, DH/Dt, and the surface Laplacian of interfacial velocity, $\Delta_S v$. These dynamic quantities all appear in the expression for DH/Dt based on differential geometry, Eq. (4.4), in which the sum $v_{,11} + v_{,22}$ in Eq. (4.4) is equal to the surface Laplacian of interfacial velocity, $\Delta_S v$ [124].

In order to accurately calculate these interfacial quantities, we apply the level-set smoothing method [125]. The mean and Gaussian curvatures are calculated first and other curvatures are then computed using the values of H and K. The nonlocal static property, $\Delta_S H$, is calculated based on the expression

$$\Delta_S H = \nabla^2 H - 2H\frac{\partial H}{\partial n} - \frac{\partial^2 H}{\partial n^2} \tag{5.1}$$

where $\nabla^2 H$ is the Laplacian of H, and $\partial H/\partial n$ and $\partial^2 H/\partial n^2$ are the first and second derivative of H with respect to the normal coordinate, respectively [126]. The interfacial velocity is calculated using the level-set method. Based on this velocity, DH/Dt, the Lagrangian derivative is evaluated with respect to the coordinates moving with the interface. We use the advective method to calculate the Lagrangian derivative, as described in Chapter III. The surface Laplacian of interfacial velocity, $\Delta_S v$, is calculated in the same manner as $\Delta_S H$. All interfacial quantities presented in this

chapter are scaled by the characteristic length scale, S_v^{-1}, and the corresponding time scale, $S_v^{-1}/\left(dS_v^{-1}/dt\right)$, where S_v is the surface area per unit volume calculated for the entire simulation volume for each structure.

As a note, while the use of a multiple time-differential size is recommended when calculating dynamic interfacial quantities (refer to Section 3.3.4 for details), for the analysis in this chapter, we use a single time differential of $\Delta\tau = 100$. This is because, unlike with the AC structure, interfaces of the CH structures with the same mean curvature can have very different rates of displacement of interfaces depending on the curvatures of the nearby interfaces. This implies that we cannot assign a single time step for interfaces that belong to a particular mean curvature group. Therefore, we choose a time differential of $\Delta\tau = 100$, which yields sufficient motion of interfaces without major evolution of the microstructures.

5.3 Procedures for Analysis

This section briefly explains the various techniques employed to analyze the morphologies and their evolution of complex structures.

5.3.1 Analysis of the Overall Morphologies Using a Statistical Approach

The statistical analysis reveals the global features of the morphology and the general relationships between interfacial quantities that govern the dynamics of coarsening. The characterization technique used in the statistical analysis is the probability distribution as a function of various interfacial characteristics. All of the probability distributions are calculated by examining each structure in its entirety. The probability distributions employed in this chapter are described below.

The overall morphologies of the three structures are statistically characterized by the interfacial shape distributions (ISDs). The ISD is the probability distribution of finding a patch of interface with a given pair of principal curvatures, κ_1 and κ_2. For

more details of the ISD, refer to Section 2.1.2. The statistical relationship between the interfacial velocity and the local mean curvature is examined through the probability distributions, $P_3(H, v)$, defined as

$$P_3(H, v) = \frac{A_3(H, v)}{A_T} \tag{5.2}$$

where $A_3(H, v)$ is the total area of interfaces with given values of H and v. This is numerically evaluated by summing interfacial areas that have mean curvature and interfacial velocity within the range of $H^i \pm \Delta H/2$ and $v^i \pm \Delta v/2$, where H^i and v^i are the center values of the i-th bin, and ΔH and Δv are the bin values in H and v coordinates, respectively. All distributions presented in this chapter are numerically evaluated in the similar manner. The correlation between the interfacial velocity and the surface Laplacian of mean curvature is examined through the probability distributions, $P_4(\Delta_S H, v)$, defined as

$$P_4(\Delta_S H, v) = \frac{A_4(\Delta_S H, v)}{A_T} \tag{5.3}$$

where $A_4(\Delta_S H, v)$ is the total area of interfaces with given values of $\Delta_S H$ and v. In addition, the correlation between the surface Laplacian of mean curvature and mean curvature is also examined through the probability distributions, $P_5(H, \Delta_S H)$, defined as

$$P_5(H, \Delta_S H) = \frac{A_5(H, \Delta_S H)}{A_T} \tag{5.4}$$

where $A_5(H, \Delta_S H)$ is the total area of interfaces with given values of H and $\Delta_S H$.

The distribution of normal velocities of interfaces with the same principal curvatures is examined through the probability distribution, $P_6(\kappa_1, \kappa_2, v)$, defined as

$$P_6(\kappa_1, \kappa_2, v) = \frac{A_6(\kappa_1, \kappa_2, v)}{A_T} \tag{5.5}$$

where $A_6(\kappa_1, \kappa_2, v)$ is the total area of interfaces with given values of κ_1, κ_2, and v.

In an effort to predict the rate of change of mean curvature, we calculate the area-weighted averages of interfacial velocity, $\langle v \rangle_{H,d}$, the surface Laplacian of interfacial velocity, $\langle \Delta_S v \rangle_{H,d}$, and the rate of change of mean curvature, $\langle DH/Dt \rangle_{H,d}$, of all interfaces with given values of H and d. For example, $\langle v \rangle_{H,d}$ is evaluated as

$$\langle v \rangle_{H,d} = \frac{A^*(H,d)}{A_{H,d}(H,d)} \tag{5.6}$$

where $A^*(H,d)$ is the sum of the product of area of a patch of interface with given values of H and d and its interfacial velocity, and $A_{H,d}(H,d)$ is the area of interfaces with given values of H and d. Other averaged quantities, $\langle \Delta_S v \rangle_{H,d}$ and $\langle DH/Dt \rangle_{H,d}$, are calculated in the same manner.

5.3.2 Analysis of Local Morphologies and Interfacial Dynamics

To gain insights into the local morphological characteristics and their evolution of the three CH structures, we visualize the interfacial quantities with shades of colors on the isosurfaces of the structure. For this analysis, we examine a cubic region of side length $6S_v^{-1}$ from each of the CH structures. The relationship between the interfacial velocity and local curvature is examined by comparing of the isosurfaces colored by the values of v and $-H$. We use the negative of the mean curvature for easier comparison of the two isosurfaces because v and $-H$, in general, have the same sign. In addition, the influence of the local variation of curvature on the interfacial velocity is investigated by comparing the isosurfaces colored by the values of v and $\Delta_S H$.

5.4 Results

5.4.1 Overall Morphologies and Interfacial Dynamics

Figure 5.2(a.1)-(c.1) shows the interfacial shape distributions of the three CH structures. These ISDs are consistent with those calculated by Kwon et al. [42]. The ISDs of the 50:50 and 40:60 CH structures, Fig. 5.2(a.1) and (b.1), show that the majority of the interfaces are saddled-shaped. The ISD of the 50:50 CH structure is symmetric about the $H = 0$ line due to the equal volume fraction of the two phases. On the other hand, the ISD of the 40:60 CH structure has similar shape as that for the 50:50 CH structure, but is slightly shifted to the left of the line as a result of the unequal volume fraction. In contrast to the two bicontinuous structures, the ISD of the 30:70 CH structure, Fig. 5.2(c.1), shows that the majority of the interfaces are elliptic surfaces.

The correlations between v and H, as well as v and $\Delta_S H$, are examined with the corresponding probability contour maps for all three structures, as shown in Fig. 5.2(a.2)-(c.2) and (a.3)-(c.3), respectively. For ease of comparison, a probability contour map of $P_3(H, v)$ is plotted against $-H$. All plot ranges are kept constant for each type of plots. In Fig. 5.2(c.2), a second probability contour map of $P_3(H, v)$ of the 30:70 CH structure with a wider range is inserted to show the entire distribution. The plots of $P_3(H, v)$ show that v and H are strongly correlated. However, it is clear that the value of H does not set v; there is a dispersion of velocities for a given H, unlike the case of nonconserved dynamics where v is proportional to H. In addition, similar correlations can be observed between v and $\Delta_S H$. Furthermore, $P_3(H, v)$ and $P_4(\Delta_S H, v)$ for each structure have similar shape, but over different ranges of H and $\Delta_S H$, that differ by approximately a factor of five. However, the distribution with respect to H show shift toward a greater value of H for the asymmetric 40:60 and 30:70 CH structures as a consequence of unequal volume fraction. The white solid

curve in each of the contour map represents the average interfacial velocity, $\langle v \rangle_H$ and $\langle v \rangle_{\Delta_S H}$, for a given value of H and $\Delta_S H$, respectively. These curves confirm the general correlations between the interfacial quantities. We find that both $\langle v \rangle_H$ and $\langle v \rangle_{\Delta_S H}$ are good fit to cubic polynomials (not shown because the fit overlaps the average values); the fit parameters are shown in the Appendix B. The apparent discrepancy between $\langle v \rangle_{\Delta_S H}$ and the peak of the $P_4(\Delta_S H, v)$ distributions at $|\Delta_S H|$ greater than 2 for all volume fractions is the result of the asymmetry of $P_4(\Delta_S H, v)$, which is not visible with the range of color chosen to show the entire distribution. Such asymmetry is nearly absent in the $P_3(H, v)$ and thus $\langle v \rangle_H$ coincides with the apparent peak of the distribution.

Since the mean curvature determines the chemical potential at the interface, it is not surprising that v and H are correlated; interfaces with higher chemical potential is expected to evolve faster than those with lower chemical potentials on the average. Similar correlation between v and H has been observed for experimental microstructures as well, e.g., in the solid-liquid dendritic mixtures of Al-Cu alloy [43]. On the other hand, the origin of the correlation between v and $\Delta_S H$ is not obvious. However, the interfacial velocity is determined by the normal gradient of the chemical potential at the interface, which is influenced by the chemical potentials of the nearby interfaces. Since the chemical potential at each interface is determined by mean curvature (due to Gibbs-Thomson effect), it is reasonable that $\Delta_S H$, which measures the local variation of mean curvature, can be correlated with v.

Since the above results point to possible correlation between H and $\Delta_S H$, we have examined $P_5(H, \Delta_S H)$ for all three structures (not shown). The contour maps reveal that, on average, $\Delta_S H$ share a negative correlation with H, but broader than other correlations we have identified. This correlation may be a result of the correlation between v and $\Delta_S H$ and v and H, or, alternatively, it may be a result of geometrically necessary variation in H for the bicontinuous structure.

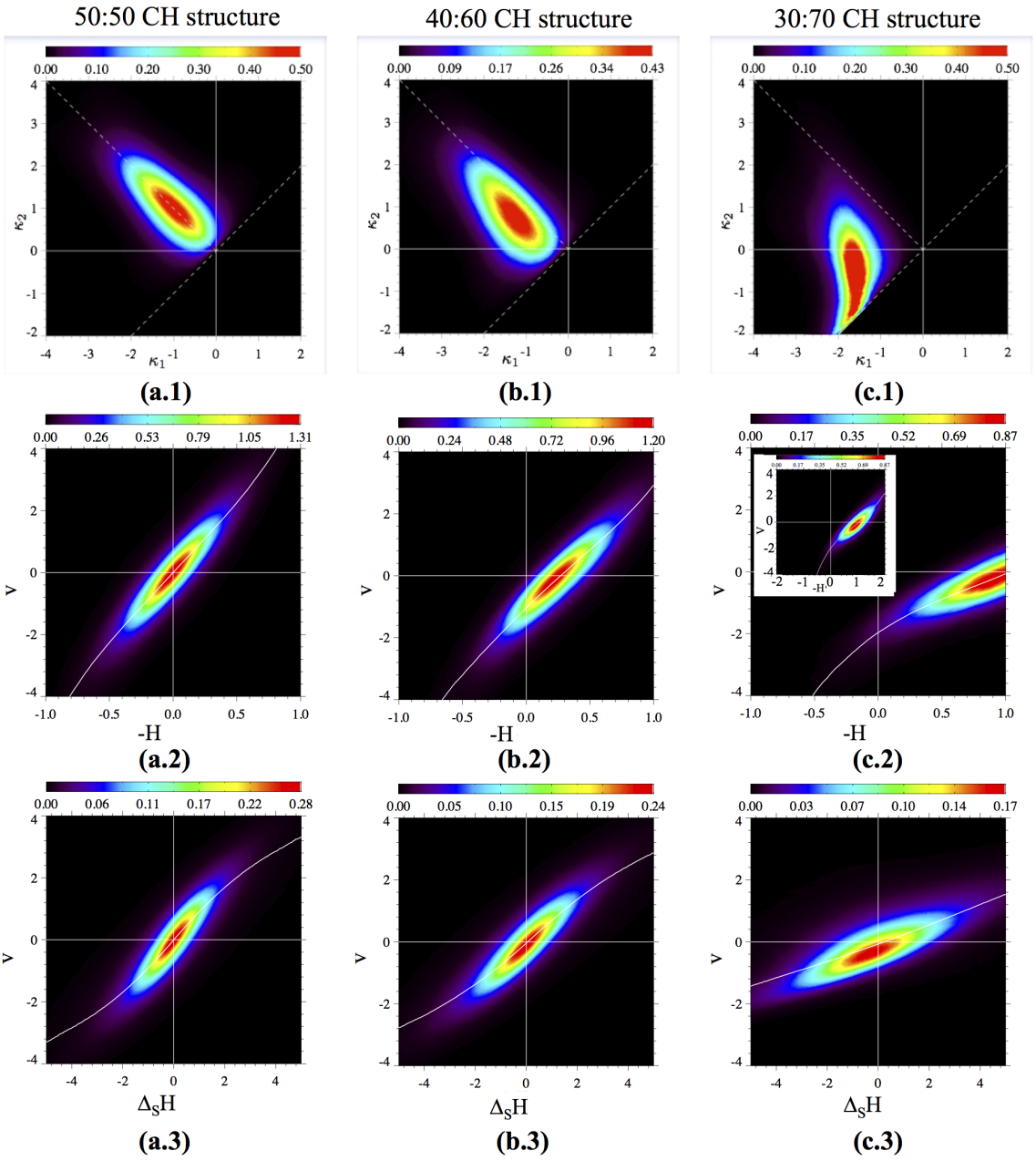

Figure 5.2: The interfacial shape distributions of (a.1) 50:50, (b.1) 40:60, and (c.1) 30:70 CH structure, along with the corresponding probability contour maps of $P_3(H, v)$ ((a.2)-(c.2)) and $P_4(\Delta_S H, v)$ ((a.3)-(c.3)). The white solid curve in each of the contour map represents the average interfacial velocity, $\langle v \rangle_H$ and $\langle v \rangle_{\Delta_S H}$, for a given a value of H and $\Delta_S H$, respectively.

5.4.2 Local Morphologies and Interfacial Dynamics

The morphologies of the interfaces of the three CH structures colored by the negative of the mean curvature values are shown in Fig. 5.3(a.1)-(c.1). While the range on the color bars for Fig. 5.3(a.1) and (b.1) is symmetric and is equal to $[-1, 1]$, the range for Fig. 5.3(c.1) is shifted and is set to [0, 2] to accommodate the substantial change in the range of the mean curvature in that structure as compared to the other two. All of the local morphologies exhibit features that are consistent with the ISDs presented in Fig. 5.2(a.1)-(c.1). The 50:50 CH structure appears to have an equal distribution of positive and negative mean curvature (consistent with the equal volume fractions of the two phases), while the 40:60 CH structure clearly has a larger proportion of interfaces with negative mean curvature, as observed in Fig. 5.3(a.1)-(b.1). The nonbicontinuous 30:70 CH structure possesses multiple isolated domains with near-spherical caps, as shown in Fig. 5.3(c.1). The fact that most of the surfaces of the isolated domains have negative mean curvature values indicates that these droplet-like interfaces enclose the minority phase (by the sign convention chosen). In addition, these isolated domains have larger $|-H|$ than the saddle-shaped interfaces in the 50:50 CH structure.

The local dynamics of coarsening is investigated by considering the interfacial velocities indicated by the color on the interfaces, as shown in Fig. 5.3(a.2)-(c.2). The comparisons between Fig. 5.3(a.1)-(c.1) and (a.2)-(c.2) reveal a general correlation between interfacial velocity and mean curvature, which is consistent with the probability distributions $P_3(H, v)$ in Fig. 5.2(a.2)-(c.2). In most regions, interfaces with large $|-H|$ also have large $|v|$, as illustrated by the circled regions A through C in these figures. These regions include both saddle-shaped and elliptic surfaces, and thus the correlation appears to hold for a wide range of interfacial morphologies without notable rules or exceptions. However, in the nonbicontinuous 30:70 CH structure, there are interfaces with $H \approx 0$ but have large $|v|$, as highlighted by the

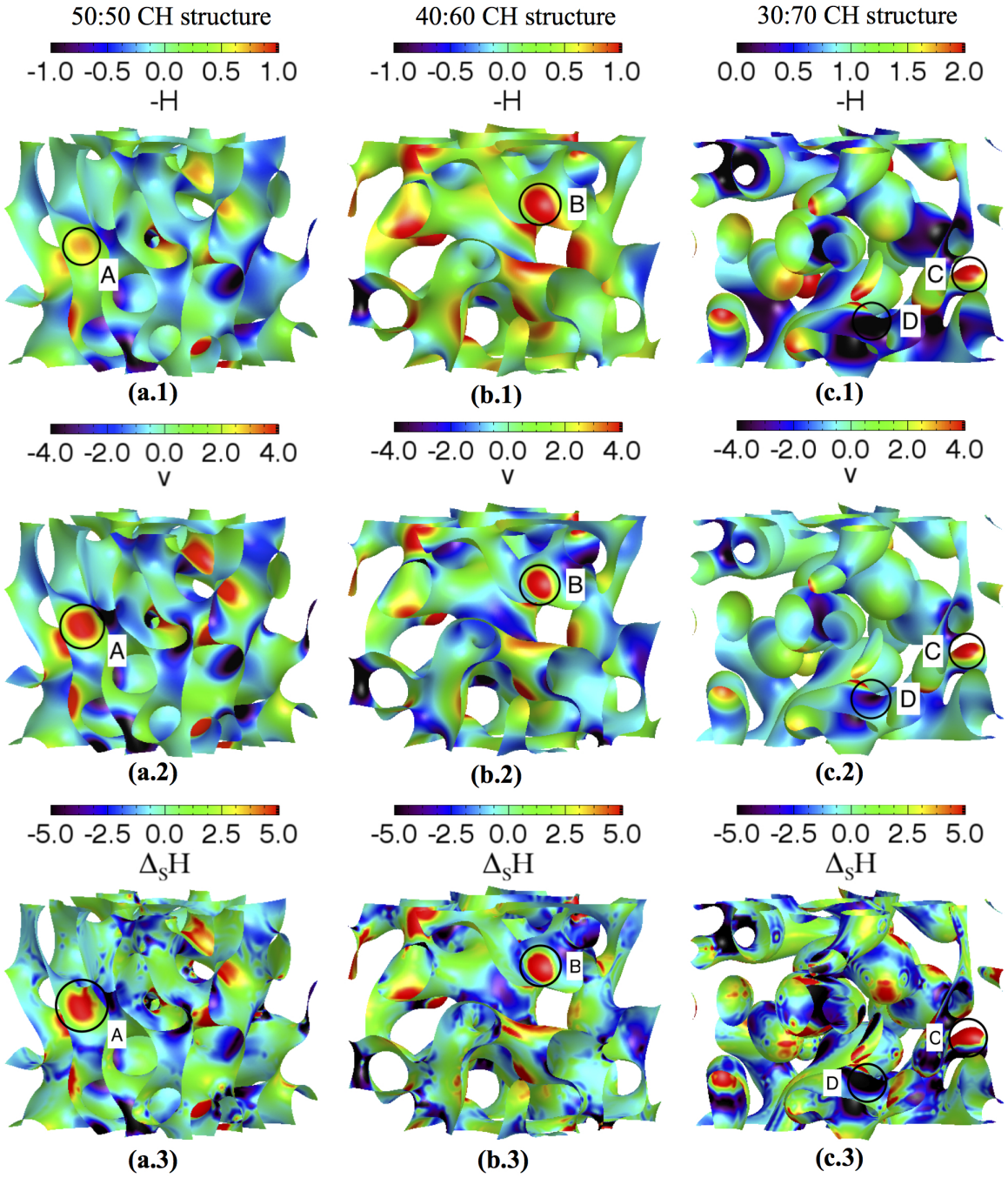

Figure 5.3: Morphologies of the CH structures with different volume fractions: (a.1)-(a.3) 50:50; (b.1)-(b.3) 40:60; and (c.1)-(c.3) 30:70, colored with (a.1)-(c.1) the negative of the mean curvature, H; (a.2)-(c.2) the interfacial velocity, v; and (a.3)-(c.3) the surface Laplacian of mean curvature, $\Delta_S H$.

circled region D in Fig. 5.3(c.1) and (c.2). This is also consistent with the contour map of $P_3(H, v)$ for the 30:70 CH structure, where the center of the distribution is shifted from $v = 0$ and $H = 0$. This apparent discrepancy can be understood by considering the driving force of coarsening being the difference in the chemical potential of the interface with respect to the average (or mean-field) chemical potential of the surroundings. It has been suggested that the interfacial velocity may be modeled as $v \propto (H - H_c)$, where H_c is the critical mean curvature (which equals the average mean curvature) of the system [43]. In this case, the interfaces having in the 30:70 CH structure, which has $H_c = -1.1$, is expected to have a nonzero velocity. This is consistent with the observation from Fig. 5.3. However, as discussed in the previous subsection, there appear to be higher-order terms that exist when v is modeled as a function of H. Nevertheless, this simple linear model may provide insights into coarsening of complex microstructures by capturing the primary dependence of v on H.

To examine the correlation between v and $\Delta_S H$ in detail, we compare the iso-surfaces colored by the surface Laplacian of mean curvature (Fig. 5.3(a.3)-(c.3)) and the normal velocity (Fig. 5.3(a.2)-(c.2)). Consistent with $P_4(\Delta_S H, v)$, it is clear that v and $\Delta_S H$ have a positive correlation as displayed by the like-colors throughout the interfaces in all three structures, highlighted by the circled regions A through D in Fig. 5.3(a.2)-(c.2) and (a.3)-(c.3). This finding agrees with the contour map of $P_4(\Delta_S H, v)$, where the centers of the distributions all lie at or near the origin. Again, we examined both saddle-shaped and elliptic surfaces, and no notable exceptions from the general correlation were found.

As a note, the roughness in the color that appears on in Fig. 5.3(a.3)-(c.3) is the result of the grid effect that manifests itself when high-order derivatives are calculated at interfaces with insufficient interfacial resolution. The level-set smoothing method applied to the microstructural data is designed to smooth up to the second-order

derivatives required in the calculation of curvatures, as evidenced by the smooth H profiles in Fig. 5.3(a.1)-(c.1). Since $\Delta_S H$ requires calculation of fourth-order derivatives across the interfaces, the level-set smoothing method cannot fully eliminate the numerical noise associated with the calculation of $\Delta_S H$. Thus, the quality of data from the calculation of $\Delta_S H$ is slightly affected. Nevertheless, the numerical noise does not seem to significantly deteriorate the quality of the data as the correlations between $\Delta_S H$ and other interfacial quantities can be quantitatively verified.

5.4.3 Distribution of Interfacial Velocities

The distribution of normal velocities of interfaces with the same principal curvatures, $P_6(\kappa_1, \kappa_2, v)$, is also examined. Figures 5.4-5.6 show the ISD and $P_6(\kappa_1, \kappa_2, v)$ for the 50:50, 40:60, and 30:70 CH structures, respectively. The principal curvature values at which $P_6(\kappa_1, \kappa_2, v)$ are plotted are shown on the ISD as solid blue circles with arrows pointing to the corresponding distributions (the actual ranges in the i-th bin are $\kappa_1^i \pm 0.01$ and $\kappa_2^i \pm 0.01$, as in the ISD calculation). For velocity, the bin size is taken to be $\Delta v = 0.16$. Each distribution is then fitted with a Gaussian function; the fit parameters are shown in Table 5.1.We find that the Gaussian function fits the distributions very well, independent of the principal curvature values and the volume fraction of the system.

The fact that a Gaussian function fits the velocity distributions across the wide range of curvatures is remarkable. However, it is even more surprising that it fits all volume fractions examined because the 50:50 and 40:60 CH structures are evolving in a self-similar manner, while the 30:70 CH structure is in the process of breaking up into individual domains that consist of spherical particles. The latter is expected to be fundamentally different from the self-similar evolution of a bicontinuous structure. Furthermore, it is notable that, while v has a wide range, σ_v is relatively constant across different curvature values for a given volume fraction. Specifically, $\sigma_v \approx 0.51 \pm$

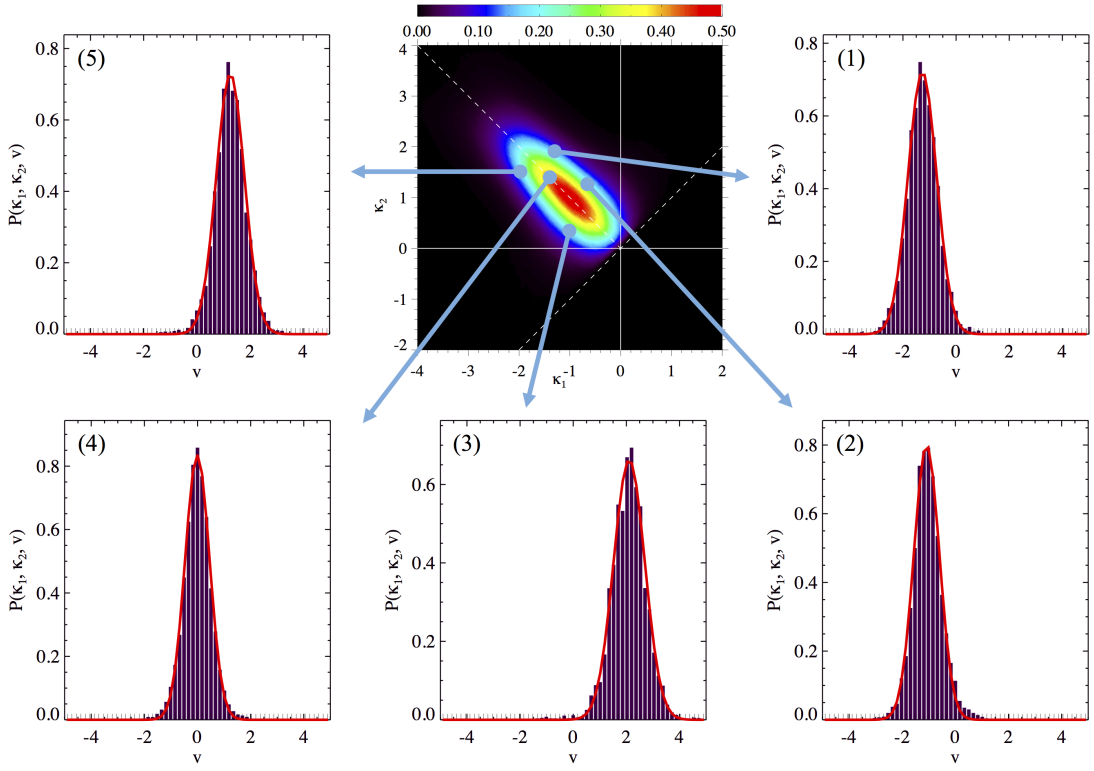

Figure 5.4: Probability distributions of interfacial velocities, $P_6(\kappa_1, \kappa_2, v)$, at various principal curvature values for the 50:50 CH structure. The principal curvature values at which $P_6(\kappa_1, \kappa_2, v)$ are plotted are shown on the ISD (top center) as solid blue circles connected to the corresponding distributions. The Gaussian fit is represented as a solid red curve on each plot. The numbers marked on the top left corner of the plots correspond to the plot numbers in Table 5.1.

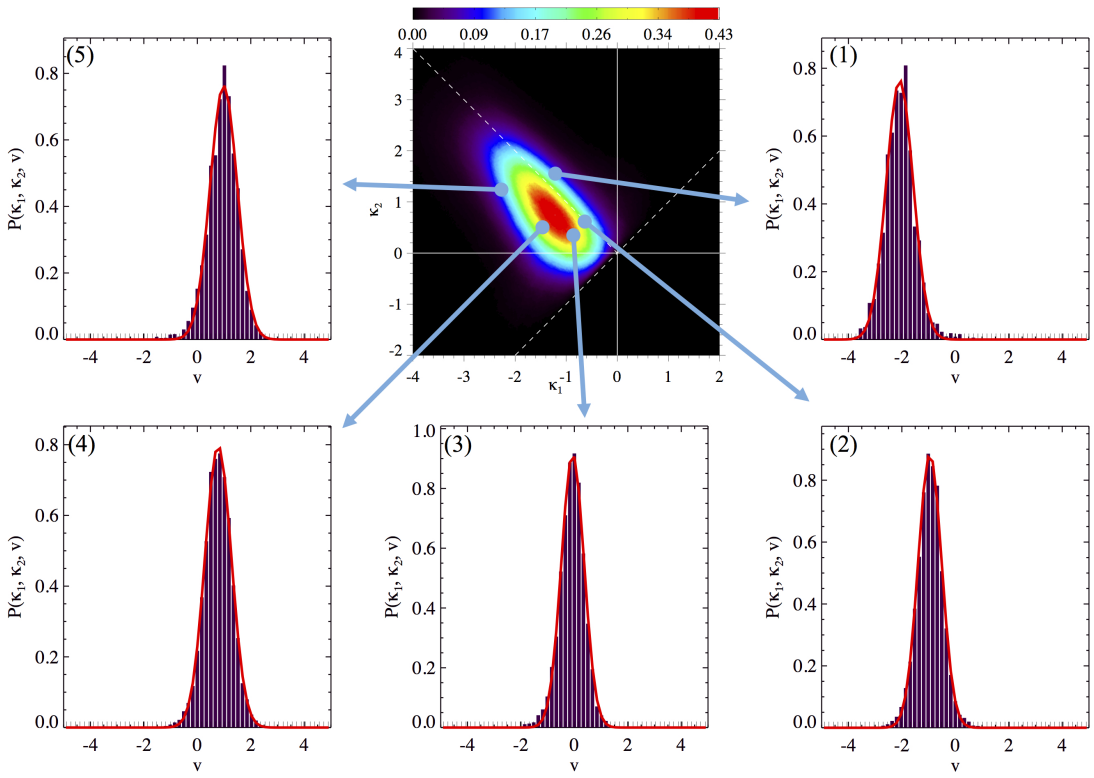

Figure 5.5: Probability distributions of interfacial velocities, $P_6(\kappa_1, \kappa_2, v)$, at various principal curvature values for the 40:60 CH structure. The principal curvature values at which $P_6(\kappa_1, \kappa_2, v)$ are plotted are shown on the ISD (top center) as solid blue circles connected to the corresponding distributions. The Gaussian fit is represented as a solid red curve on each plot. The numbers marked on the top left corner of the plots correspond to the plot numbers in Table 5.1.

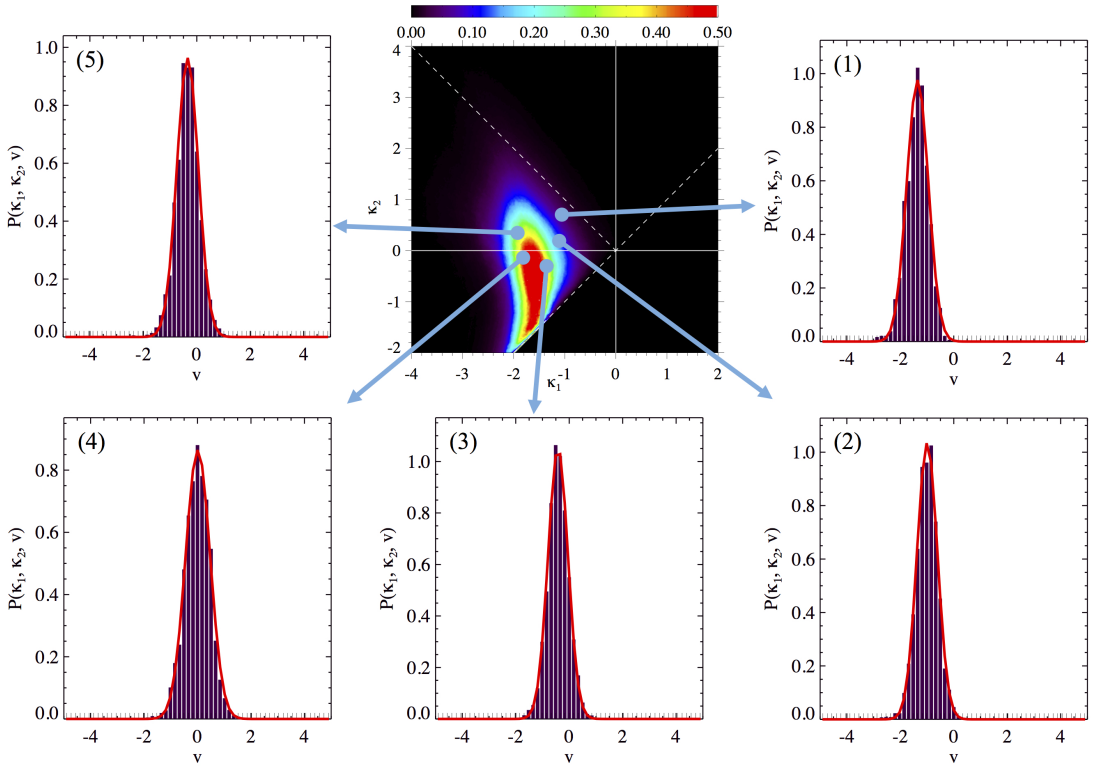

Figure 5.6: Probability distributions of interfacial velocities, $P_6(\kappa_1, \kappa_2, v)$, at various principal curvature values for the 30:70 CH structure. The principal curvature values at which $P_6(\kappa_1, \kappa_2, v)$ are plotted are shown on the ISD (top center) as solid blue circles connected to the corresponding distributions. The Gaussian fit is represented as a solid red curve on each plot. The numbers marked on the top left corner of the plots correspond to the plot numbers in Table 5.1.

Structure	Plot #	κ_1	κ_2	$\langle v \rangle$	σ_v
50:50 CH Structure	1	-1.48	1.98	-1.24	0.54
	2	-0.72	1.22	-1.04	0.47
	3	-1.37	0.37	2.06	0.58
	4	-1.25	1.25	-0.01	0.45
	5	-1.98	1.48	1.23	0.52
40:60 CH Structure	1	-1.13	1.63	-2.01	0.50
	2	-1.00	1.00	-0.93	0.44
	3	-0.80	0.30	-0.06	0.42
	4	-1.37	0.37	0.77	0.49
	5	-2.02	1.02	0.96	0.50
30:70 CH Structure	1	-1.18	0.78	-1.34	0.40
	2	-1.09	0.29	-0.98	0.38
	3	-1.40	-0.20	-0.41	0.37
	4	-1.98	-0.02	0.01	0.46
	5	-1.95	0.35	-0.33	0.40

Table 5.1: Fit parameters of $P_6(\kappa_1, \kappa_2, v)$ presented in Figs. 5.4-5.6. The plot numbers are the numbers indicated on the top left corner of each distribution plot. Variables κ_1 and κ_2 are the curvature values chosen to plot $P_6(\kappa_1, \kappa_2, v)$, and $\langle v \rangle$ and σ_v are the average and the standard deviation of the Gaussian fit, respectively.

0.07 for the 50:50 CH structure, $\sigma_v \approx 0.45 \pm 0.05$ for the 40:60 CH structure, and $\sigma_v \approx 0.40 \pm 0.06$ for the 30:70 CH structure. The origin of the Gaussian distribution is still not clear and requires further investigation.

5.4.4 Prediction of Curvature Evolution

Having gained insights into the evolution of interfaces during coarsening in complex structures, we now attempt to predict the evolution of the average curvature based on local morphological characteristics. As introduced in Chapter IV, the rate of change of mean curvature, DH/Dt, can be expressed as Eq. (4.4) based on differential geometry. Since $2H^2 - K = d^2$ and $v_{,11} + v_{,22} = \Delta_S H$, Eq. (4.4) can be re-written as

$$\frac{DH}{Dt} = -d^2 v - \frac{1}{2}\left(\Delta_S v\right) \quad . \tag{5.7}$$

In the previous chapter, since $v = -MH$ in nonconserved dynamics [84], where M is the proportionality constant, we derive the expression for DH/Dt solely in terms of static interfacial properties, namely the local curvatures, H and K, and nonlocal interfacial property, $\Delta_S H$ (see Eq. (4.5)). In conserved dynamics, even though v is not proportional to mean curvature, the statistical analysis in Section 5.4.1 demonstrated that the *average* interfacial velocity can be expressed in terms of a cubic polynomial of H. Based on this finding, we employ a semi-analytical model to derive an expression for the average rate of change of mean curvature solely in terms of the local curvatures.

By averaging Eq. (5.7) over all interfaces with given values of H and d, the average rate of change of mean curvature, $\langle DH/Dt \rangle_{H,d}$, with the given values of H and d can be written as

$$\left\langle \frac{DH}{Dt} \right\rangle_{H,d} = -d^2 \langle v \rangle_{H,d} - \frac{1}{2} \langle \Delta_S v \rangle_{H,d} \tag{5.8}$$

where $\langle v \rangle_{H,d}$ and $\langle \Delta_S v \rangle_{H,d}$ are the average interfacial velocity and surface Laplacian of interfacial velocity, respectively, of all interfaces with given values of H and d. The expressions for $\langle v \rangle_{H,d}$ and $\langle \Delta_S v \rangle_{H,d}$ in terms of H and d are numerically determined through curve fitting the simulation data using the POLY_FIT function in Interactive Data Language (IDL) software. We then substitute two expressions into Eq. (5.8) to express $\langle DH/Dt \rangle_{H,d}$ in terms of the local curvatures. The curvatures H and d are chosen to express $\langle v \rangle_{H,d}$ and $\langle \Delta_S v \rangle_{H,d}$ since H alone cannot fully describe the local morphology, and thus we require a second parameter. The net curvature, d, is chosen since, unlike the Gaussian curvature, it has the same unit as H and it has an intuitive interpretation as the distance from the origin on the ISD map (refer to Fig. 2.4 in Section 2.1.2), representing the curviness of the interface.

Figure 5.7a shows the values of $\langle v \rangle_{H,d}$ versus d for different values of H for the 50:50 CH structure drawn with solid diamonds that are connected by solid lines,

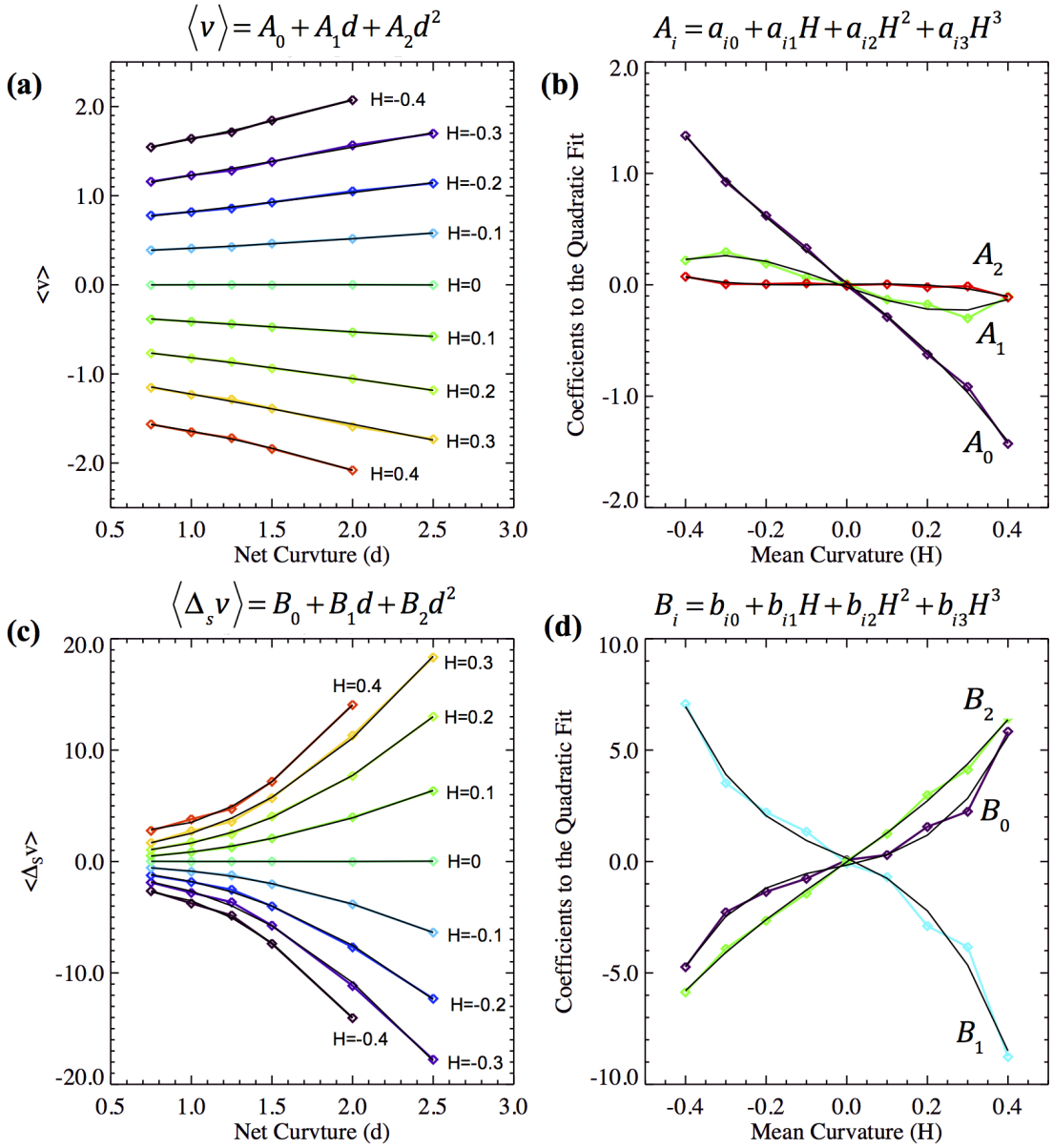

Figure 5.7: (a) Values of $\langle v \rangle_{H,d}$, calculated from the simulation data, as a function of d for different values of H for the 50:50 CH structure are drawn with the colored diamond symbols that are connected by colored lines. Each color represents a given H value. The quadratic fit, in the form of $A_0(H) + A_1(H)d + A_2(H)d^2$, for each set of points for a given H value is drawn with a solid black curve. (b) Values of the coefficients, $A_0(H)$, $A_1(H)$ and $A_2(H)$, as functions of H are drawn with colored diamond symbols that are connected by colored lines. The cubic polynomial fit, in the form of $A_i = a_{i0} + a_{i1}H + a_{i2}H^2 + a_{i3}H^3$ with $i = 0$, 1 and 2, for each coefficient is drawn with a solid black curve. Subfigures (c) and (d) are similar to (a) and (b) but for the average surface Laplacian of interfacial velocity, $\langle \Delta_S v \rangle_{H,d}$ and the coefficients of its quadratic fit, $B_0(H)$, $B_1(H)$, and $B_2(H)$.

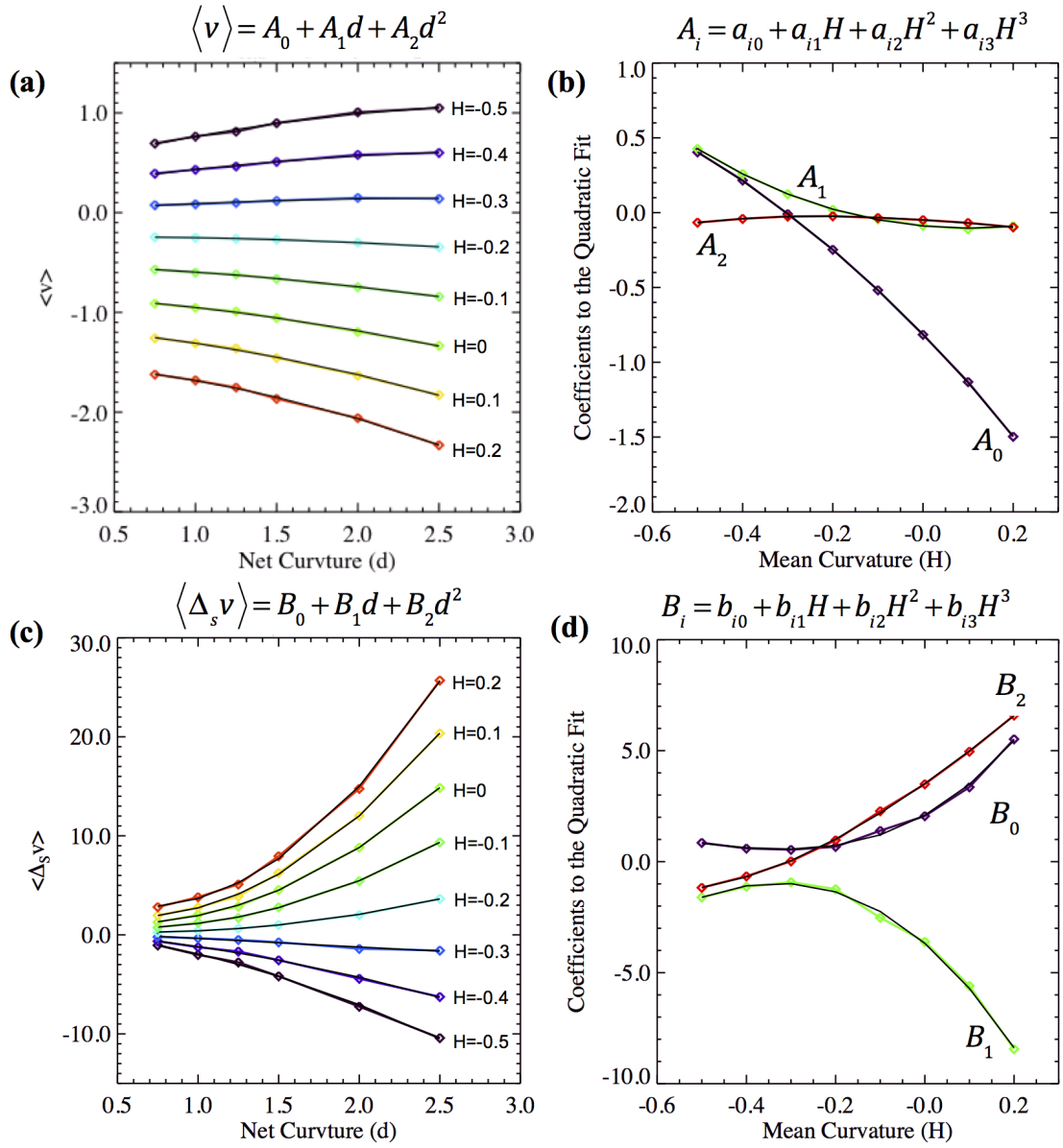

Figure 5.8: (a) Values of $\langle v \rangle_{H,d}$, calculated from the simulation data, as a function of d for different values of H for the 40:60 CH structure are drawn with the colored diamond symbols that are connected by colored lines. Each color represents a given H value. The quadratic fit, in the form of $A_0(H) + A_1(H)d + A_2(H)d^2$, for each set of points for a given H value is drawn with a solid black curve. (b) Values of the coefficients, $A_0(H)$, $A_1(H)$ and $A_2(H)$, as functions of H are drawn with colored diamond symbols that are connected by colored lines. The cubic polynomial fit, in the form of $A_i = a_{i0} + a_{i1}H + a_{i2}H^2 + a_{i3}H^3$ with $i = 0$, 1 and 2, for each coefficient is drawn with a solid black curve. Subfigures (c) and (d) are similar to (a) and (b) but for the average surface Laplacian of interfacial velocity, $\langle \Delta_S v \rangle_{H,d}$ and the coefficients of its quadratic fit, $B_0(H)$, $B_1(H)$, and $B_2(H)$.

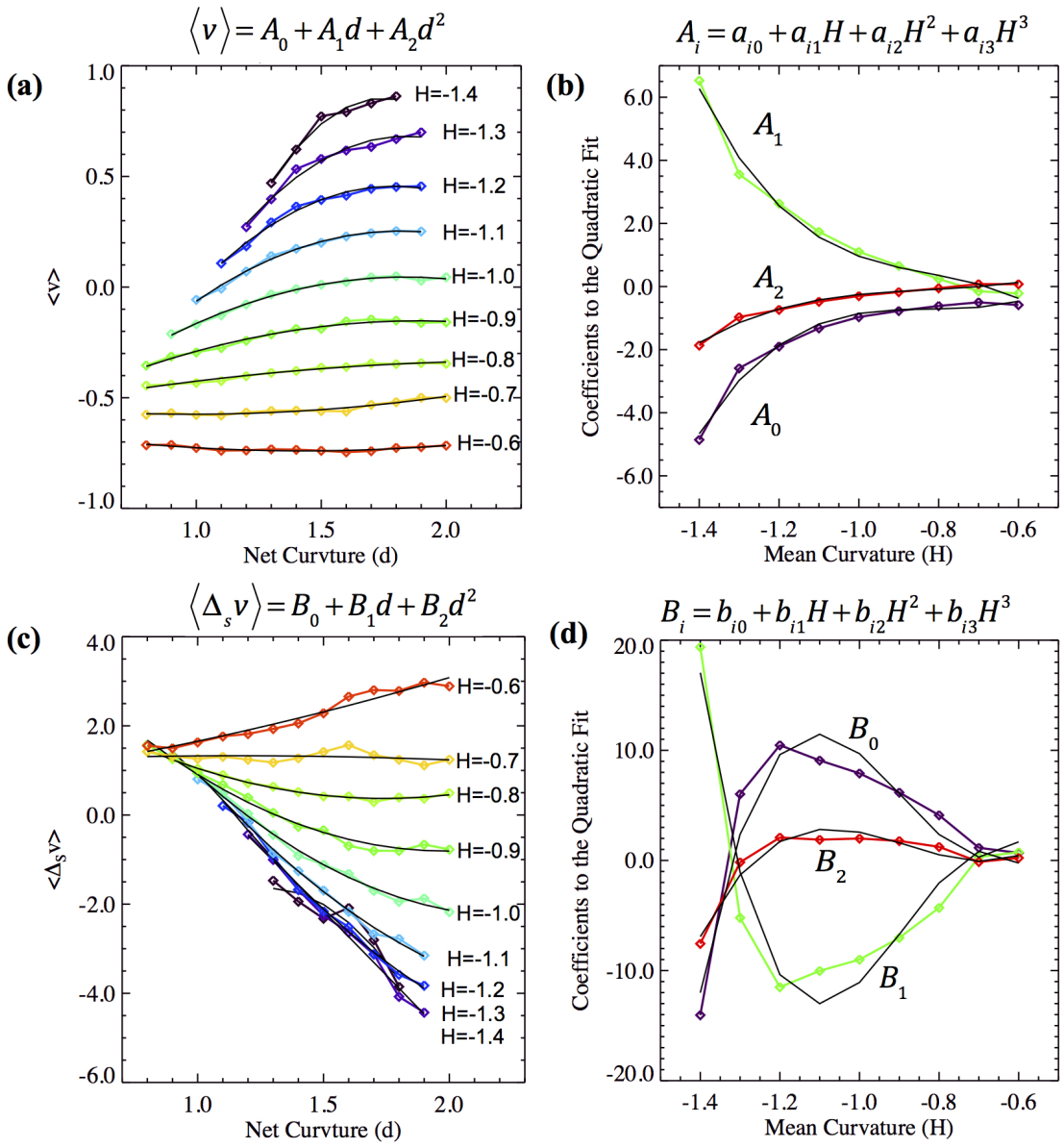

Figure 5.9: (a) Values of $\langle v \rangle_{H,d}$, calculated from the simulation data, as a function of d for different values of H for the 30:70 CH structure are drawn with the colored diamond symbols that are connected by colored lines. Each color represents a given H value. The quadratic fit, in the form of $A_0(H) + A_1(H)d + A_2(H)d^2$, for each set of points for a given H value is drawn with a solid black curve. (b) Values of the coefficients, $A_0(H)$, $A_1(H)$ and $A_2(H)$, as functions of H are drawn with colored diamond symbols that are connected by colored lines. The cubic polynomial fit, in the form of $A_i = a_{i0} + a_{i1}H + a_{i2}H^2 + a_{i3}H^3$ with $i = 0$, 1 and 2, for each coefficient is drawn with a solid black curve. Subfigures (c) and (d) are similar to (a) and (b) but for the average surface Laplacian of interfacial velocity, $\langle \Delta_S v \rangle_{H,d}$ and the coefficients of its quadratic fit, $B_0(H)$, $B_1(H)$, and $B_2(H)$.

where each color represents a given H value. A quadratic fit in the form of

$$\langle v \rangle_{H,d} = A_0(H) + A_1(H)d + A_2(H)d^2 \tag{5.9}$$

is applied on each set of $\langle v \rangle_{H,d}$ points for a given H value and is drawn as a solid black curve on top of the same plot. To find the expressions for the coefficients, $A_0(H)$, $A_1(H)$, and $A_2(H)$, in terms of H, we also plotted the values of coefficients versus H as colored diamonds. A cubic polynomial fit in the form of

$$A_i = a_{i0} + a_{i1}H + a_{i2}H^2 + a_{i3}H^3 \tag{5.10}$$

where $i = 0$, 1 and 2, is applied to each coefficient and is drawn as a solid black curve (Fig. 5.7b). The two numerical fits, Eqs. (5.9) and (5.10), demonstrate that the expression for $\langle v \rangle_{H,d}$ is a combination of a quadratic function of d and a cubic function of H. The values of the fit parameters a_{i0}, a_{i1}, a_{i2}, and a_{i3} in Eq. (5.10) are shown in the Appendix B.

The same approach was used to obtain the expression for $\langle \Delta_S v \rangle_{H,d}$. The plots of data points and their numerical fits are shown in Fig. 5.7c and d. Similar to the expression for $\langle v \rangle_{H,d}$, the expression for $\langle \Delta_S v \rangle_{H,d}$ is a combination of a quadratic function of d and a cubic function of H. The values of the fit parameters are shown in the Appendix B. The plots of $\langle v \rangle_{H,d}$ and $\langle \Delta_S v \rangle_{H,d}$ and the coefficients for their respective numerical fits for the 40:60 and 30:70 CH structures are shown in Figs. 5.8 and 5.9, respectively. We find that $\langle v \rangle_{H,d}$ and $\langle \Delta_S v \rangle_{H,d}$ for the 40:60 and 30:70 CH structures also have the same quadratic and cubic dependencies on d and H, respectively. The values of the fit parameters for the 40:60 and 30:70 CH structures are also included in the Appendix B.

The expressions for $\langle v \rangle_{H,d}$ and $\langle \Delta_S v \rangle_{H,d}$ are substituted into Eq. (5.8) to obtain the expression for $\langle DH/Dt \rangle_{H,d}$ as a function of the local curvatures: H and d. The

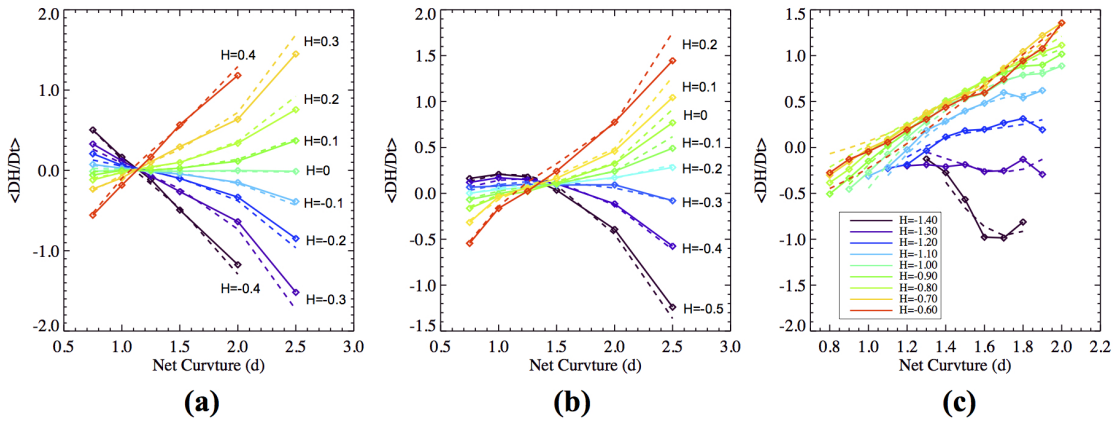

Figure 5.10: Plots of the predicted values of $\langle DH/Dt \rangle_{H,d}$ based on Eq. (5.8) for the CH structure with volume fractions of (a) 50:50, (b) 40:60, and (c) 30:70 are drawn with dashed colored curves. In addition, the calculated values of $\langle DH/Dt \rangle_{H,d}$ are drawn with solid colored curves with the diamond symbol, which mark select values of $\langle DH/Dt \rangle_{H,d}$.

predicted values of $\langle DH/Dt \rangle_{H,d}$ based on the expressions of $\langle v \rangle_{H,d}$ and $\langle \Delta_S v \rangle_{H,d}$ are compared with $\langle DH/Dt \rangle_{H,d}$ directly calculated from DH/Dt at all interfaces with given values of H and d in Fig. 5.10. The calculated $\langle DH/Dt \rangle_{H,d}$ is represented as solid colored curves while the predicted $\langle DH/Dt \rangle_{H,d}$ is represented as dashed colored curves. The predicted $\langle DH/Dt \rangle_{H,d}$ agrees well with the calculated $\langle DH/Dt \rangle_{H,d}$.

The plot of $\langle DH/Dt \rangle_{H,d}$ for the 50:50 CH structure, Fig. 5.10a, shows that H of interfaces with low net curvature, $d \lesssim 1.2$, evolves toward the average mean curvature, $\bar{H} = 0$, while H of interfaces with larger net curvature, $d \gtrsim 1.3$, diverges from $\bar{H}$. For example, the red curve corresponding to $H = 0.4$ is negative for $d \lesssim 1.2$, indicating H evolving toward $H = 0$, while it becomes positive for $d \gtrsim 1.3$, which would result in increasing H further. This finding demonstrates that interfaces with low net curvature are evolving to reduce the local mean curvature during coarsening. On the other hand, interfaces with large net curvature appear to break the symmetry of the saddle-shape even when H is not large ($|H| \geq 0.1$), which can be understood as a part of the process leading to topological singularity. The same trend is observed

for the plot of of the 40:60 CH structure,Fig. 5.10b, which has $\bar{H} = -0.2$.

In the case of the nonbicontinuous 30:70 CH structure, the evolution of mean curvature is more complex, as indicated by the plot of $\langle DH/Dt \rangle_{H,d}$ shown in Fig. 5.10c. We find that H of interfaces with $H \gtrsim \bar{H} = -1.1$ and $d \lesssim 1.2$ evolves toward $\bar{H}$, while H of interfaces with $H \lesssim -1.2$ and $d \gtrsim 1.3$ diverges from $\bar{H}$. This is consistent with the results for bicontinuous structures. Indeed a sizable portion of interfaces with $H \gtrsim \bar{H}$ of the 30:70 CH structure are saddle-shaped, like those of the bicontinuous structures, as can be observed in the ISD in Fig. 5.2(c.1). However, this trend in the evolution of H gradually disappears for interfaces with $H < \bar{H}$. For interfaces with $H \lesssim -1.2$, which are mostly of isolated domains that have elliptical geometry, we find that $|H|$ increases on the average, which represents dissolution of high-curvature interfaces. Thus, the observation that low net curvature regions evolve toward reducing the difference between the mean curvature and the local mean curvature, while high net curvature regions evolves in the opposite direction, may be universal not only to bicontinuous structures but also to hyperbolic interfaces within transient structures that are similar to bicontinuous structures.

The results obtained from the semi-analytical approach demonstrate that the average rate of change of curvatures can be predicted based on the local curvatures. Furthermore, as discussed in the introduction, an analytical expression for the growth rate of a particle, dR/dt, as a function of radius, R, was a critical input in deriving the time-independent particle size distribution and the coarsening law. As in the LSW theory, the expression for the average rate of change of curvature we have obtained here can be used to solve for the time-independent interfacial shape distribution using the continuity equation. This should be the next step in the development of theory of coarsening of complex structures.

5.5 Conclusion

In this chapter, we have examined the correlations between the interfacial velocity and static local properties and developed a semi-analytical approach to predict curvature evolution of complex structures undergoing coarsening following spinodal decomposition. Three simulated CH structures are generated using phase-field simulations with different volume fractions that resulted in two bicontinuous structures and one nonbicontinuous structure. The level-set smoothing method is employed to ensure that various interfacial quantities used in the analysis are accurately calculated.

The probability contour maps have shown that there exist a correlation between v and H; such correlation has been observed for dendritic mixtures of Al-Cu alloy [43]. We also identified a correlation between v and $\Delta_S H$; such correlation has not yet been examined because a technique has not been developed to compute the surface Laplacian of mean curvature for experimentally obtained three-dimensional microstructures. The analyses of $\langle v \rangle_H$ and $\langle v \rangle_{\Delta_S H}$ indicate that average v is of the form of a cubic polynomial of H and $\Delta_S H$. Examination of the local morphologies and their evolution also support the general findings from the statistical analysis.

We find that the distribution of normal velocities of interfaces with the same local principal curvatures fits a Gaussian function well, independent of the local principal curvatures and the volume fractions of the structures. This finding is remarkable since the bicontinuous and nonbicontinuous structures are undergoing fundamentally different evolution, one self-similar and the other in the process of breaking up into disconnected domains. The mechanism that drives the distributions toward Gaussian is still not understood and requires further investigation.

To predict the evolution of mean curvature, we employ a semi-analytical approach to derive the expression for the average rate of change of mean curvature in terms

of static local properties, H and d. The predicted $\langle DH/Dt \rangle_{H,d}$ match the directly calculated $\langle DH/Dt \rangle_{H,d}$ well. The plots of $\langle DH/Dt \rangle_{H,d}$ show that, in the case of the bicontinuous structures, interfaces with low net curvature evolve to reduce the local mean curvature while the opposite occurs for interfaces with large net curvature. The results demonstrate that we have successfully developed a semi-analytical approach that can be employed to predict the evolution of mean curvature and represent a significant advancement in the development of theory of coarsening of complex structures.

CHAPTER VI

Preliminary Results From Examination of Continuity Equation and Singularity

6.1 Introduction

This chapter discusses preliminary work that requires further investigation. The first section focuses on the derivation of the continuity equation of area flow in terms of the interfacial shape distribution. The second section examines the morphological evolution of a rod undergoing pinch-off, resulting in topological singularity.

6.2 Continuity Equation of Interfacial Area

The development of the theory of coarsening will enable the prediction of the evolution of the overall morphology of a microstructure undergoing coarsening. If the microstructure evolves self-similarly, then the probability distribution that quantifies the overall morphology becomes time-independent. As explained in Chapter I, in the case of the coarsening of spherical particles, the LSW theory predicts the overall morphology from the time-independent particle size distribution obtained from the solution of the continuity equation, Eq. (1.6).

A similar approach can be taken to predict the overall morphology of complex microstructures. Chapters IV & V show that the complex morphologies of the bicon-

tinuous structures can be statistically represented by the ISD. Much like the particle size distribution, the ISD also becomes time-independent when a microstructure reaches the self-similar state. As the ISD is based on the area density, we cannot use the same continuity equation, Eq. (1.6), to describe the ISD. Therefore, in this section, we derive the appropriate continuity equation for interfacial areas.

6.2.1 Derivation of the General Continuity Equation for Interfacial Area

The total surface area of the microstructure, A_T, is defined as

$$A_T = \int_S dS \ , \tag{6.1}$$

where S is the surface of the microstructure. Since the surface consists of large number of infinitesimal surface patches with varying principal curvatures, k_1 and k_2, positioned within a three-dimensional space, Eq. (6.1) can be re-formulated as

$$A_T = \int\int \left[\int_S dS \ \delta(k_1 - \kappa_1)\delta(k_2 - \kappa_2) \right] d\kappa_1 d\kappa_2 \ , \tag{6.2}$$

where κ_1 and κ_2 are the coordinates in the principal curvature space. Note that, for this derivation only, we differentiate the notations between the principal curvatures defined in the physical space, k_1 and k_2, and the principal curvature coordinates κ_1 and κ_2.

We now introduce a new variable $A_{\boldsymbol{\kappa}}(\kappa_1, \kappa_2)$, which represents a curvature distribution based on area density as a function of κ_1 and κ_2. Its value at each curvature bin (for a given κ_1 and κ_2 value) is given by

$$A_{\boldsymbol{\kappa}}(\kappa_1, \kappa_2) = \int_S dS \ \delta(k_1 - \kappa_1)\delta(k_2 - \kappa_2) \ , \tag{6.3}$$

which is the total area of all surface patches with $k_1 = \kappa_1$ and $k_2 = \kappa_2$. This curvature distribution becomes ISD once normalized by the total surface area of the system, A_T. Based on the definition of $A_{\boldsymbol{\kappa}}$, A_T can be re-defined as

$$A_T = \int \int A_{\boldsymbol{\kappa}} \, d\kappa_1 d\kappa_2 \ . \tag{6.4}$$

If the surface evolves in time, then both A_T and $A_{\boldsymbol{\kappa}}(\kappa_1, \kappa_2)$ become functions of time t as well.

In general, the differentiable form of the continuity equation for some density, f, is given by

$$\frac{\partial f}{\partial t} + \bar{\nabla} \cdot \boldsymbol{j} = Q, \tag{6.5}$$

where $\boldsymbol{j}$ is the flux of density defined as the product of the density and its velocity in the space where the density is defined, and Q is the source/sink term. The symbol $\bar{\nabla}\cdot$ is the divergence operator on the space in which f is defined and $\partial/\partial t$ is a partial time derivative evaluated on a fixed frame of reference where f is defined, which is different from an ordinary time derivative, d/dt. Note also that it is different from the Lagrangian derivative defined in the material frame, D/Dt, which is reserved for changes within a physical space.

In the case of $A_{\boldsymbol{\kappa}}(\kappa_1, \kappa_2, t)$, which lies in the two-dimensional principal curvature space, the continuity equation becomes

$$\frac{\partial A_{\boldsymbol{\kappa}}}{\partial t} + \frac{\partial}{\partial \kappa_1}\left(\boldsymbol{j}_{\kappa_1}\right) + \frac{\partial}{\partial \kappa_2}\left(\boldsymbol{j}_{\kappa_2}\right) = Q, \tag{6.6}$$

where $\boldsymbol{j}_{\kappa_1}(\kappa_1, \kappa_2)$ and $\boldsymbol{j}_{\kappa_2}(\kappa_1, \kappa_2)$ represent the flux of area density along the κ_1 and κ_2 coordinates, respectively, and $Q(\kappa_1, \kappa_2)$ is the source term that accounts for the rate of generation/loss of area during the evolution of the microstructure. The value

of $\boldsymbol{j}_{\kappa_1}(\kappa_1,\kappa_2)$ and $\boldsymbol{j}_{\kappa_2}(\kappa_1,\kappa_2)$ is defined as

$$\boldsymbol{j}_{\kappa_1}(\kappa_1,\kappa_2) = \int_S \frac{Dk_1}{Dt}\, dS\delta(k_1-\kappa_1)\delta(k_2-\kappa_2) \ , \tag{6.7}$$

$$\boldsymbol{j}_{\kappa_2}(\kappa_1,\kappa_2) = \int_S \frac{Dk_2}{Dt}\, dS\delta(k_1-\kappa_1)\delta(k_2-\kappa_2) \ , \tag{6.8}$$

respectively, where Dk_1/Dt and Dk_2/Dt are the rate of change of principal curvatures defined in physical space. After multiplying the right hand side by $A_{\boldsymbol{\kappa}}/A_{\boldsymbol{\kappa}}$, Eqs. (6.7) & (6.8) simplify to

$$\boldsymbol{j}_{\kappa_1}(\kappa_1,\kappa_2) = A_{\boldsymbol{\kappa}} \left\langle \frac{Dk_1}{Dt} \right\rangle_{\kappa_1,\kappa_2} \ , \tag{6.9}$$

$$\boldsymbol{j}_{\kappa_2}(\kappa_1,\kappa_2) = A_{\boldsymbol{\kappa}} \left\langle \frac{Dk_2}{Dt} \right\rangle_{\kappa_1,\kappa_2} \ , \tag{6.10}$$

respectively, where $\langle Dk_1/Dt\rangle_{\kappa_1,\kappa_2}$ and $\langle Dk_2/Dt\rangle_{\kappa_1,\kappa_2}$ are the average rate of change of principal curvatures of all interfaces with $k_1=\kappa_1$ and $k_2=\kappa_2$. Substituting Eqs. (6.9) & (6.10) into Eq. (6.6) results in

$$\frac{\partial A_{\boldsymbol{\kappa}}}{\partial t} + \frac{\partial}{\partial \kappa_1}\left(A_{\boldsymbol{\kappa}} \left\langle \frac{Dk_1}{Dt} \right\rangle_{\kappa_1,\kappa_2} \right) + \frac{\partial}{\partial \kappa_2}\left(A_{\boldsymbol{\kappa}} \left\langle \frac{Dk_2}{Dt} \right\rangle_{\kappa_1,\kappa_2} \right) = Q \ . \tag{6.11}$$

To determine the source term, Q, we must examine how the overall surface area A_T changes with time. Based on the calculus of moving surfaces, the rate of change of the surface integral is defined as

$$\frac{d}{dt}\int_S dS = \int_S 2Hv\, dS \tag{6.12}$$

where H is the interfacial mean curvature and v is the normal velocity [127]. As done in Eq. (6.2), one can isolate surface patches with same principal curvatures to

re-write Eq. (6.12) as

$$\int\int \left[\frac{d}{dt} \int\limits_S dS\ \delta(k_1 - \kappa_1)\delta(k_2 - \kappa_2) \right] d\kappa_1 d\kappa_2 = \tag{6.13}$$
$$\int\int \left[\int\limits_S 2Hv\, dS\ \delta(k_1 - \kappa_1)\delta(k_2 - \kappa_2) \right] d\kappa_1 d\kappa_2.$$

Substituting Eq. (6.3) into the left hand side and multiplying the right hand side with $A_{\boldsymbol{\kappa}}/A_{\boldsymbol{\kappa}}$, Eq. (6.13) is simplified as

$$\frac{dA_{\boldsymbol{\kappa}}}{dt} = A_{\boldsymbol{\kappa}} \left(\kappa_1 + \kappa_2\right) < v >_{\kappa_1,\kappa_2} = 2A_{\boldsymbol{\kappa}} H < v >_{\kappa_1,\kappa_2} \ , \tag{6.14}$$

where $< v >_{\kappa_1,\kappa_2}$ is the area-weighted average interfacial velocity of all surface patches with $k_1 = \kappa_1$ and $k_2 = \kappa_2$. Equation (6.14) shows that the flow of $A_{\boldsymbol{\kappa}}$ in the principal curvature space is not conserved because the area of a moving interfacial patch changes during the evolution unless the mean curvature is zero. This also implies that the source/sink term in Eq. (6.11) is nonzero even in the absence of topological singularity.

The final form of the continuity equation in terms of the curvature distribution $A_{\boldsymbol{\kappa}}$ is obtained by combining Eqs. (6.11) and (6.14):

$$\frac{\partial A_{\boldsymbol{\kappa}}}{\partial t} + \frac{\partial}{\partial \kappa_1}\left(A_{\boldsymbol{\kappa}} \left\langle \frac{Dk_1}{Dt} \right\rangle_{\kappa_1,\kappa_2} \right) + \frac{\partial}{\partial \kappa_2}\left(A_{\boldsymbol{\kappa}} \left\langle \frac{Dk_2}{Dt} \right\rangle_{\kappa_1,\kappa_2} \right) \tag{6.15}$$
$$= A_{\boldsymbol{\kappa}} \left(\kappa_1 + \kappa_2\right) < v >_{\kappa_1,\kappa_2} + Q_s \ ,$$

where Q_s is the source/sink term that accounts for the discontinuous changes in interfacial curvatures resulting from topological singularities, e.g. pinching of a rod. An example of the discontinuous changes in interfacial curvatures is presented in Section 6.3, in which the morphological evolution of a rod undergoing pinching is examined.

Equation (6.15) is general and should apply to bicontinuous structures as well as those consisting of spherical particles. Thus, in the following subsection, we verify the equation by applying it to a system of spherical particles.

6.2.2 Validation of the Continuity Equation for Coarsening of Spherical Particles

To examine the validity of Eq. (6.15), we apply the equation to solve for the time-independent curvature distribution for spherical particles undergoing coarsening, using the same assumptions as the LSW theory.

6.2.2.1 Mean Curvature Distribution in Terms of Number Density

The particle size distribution presented in the LSW theory is defined in the radius space based on number density. Since Eq. (6.15) is defined in the curvature space, first, we re-derive the time-independent particle size distribution presented in the LSW theory in the mean curvature space (since spheres have $\kappa_1 = \kappa_2 = H$) and compare with the time-independent mean curvature distribution based on area density that will be derived subsequently using the general form of Eq. (6.15).

We first define a mean curvature distribution based on number density, $f(H,t)$, as a function of the mean curvature and time. As in Eq. (1.6), the continuity equation in terms of $f(H,t)$ is

$$\frac{\partial f}{\partial t} + \frac{\partial}{\partial H}\left(f\frac{DH}{Dt}\right) = 0 \ , \tag{6.16}$$

where DH/Dt is the rate of change of mean curvature defined in the physical space. We then transform the coordinates into dimensionless forms, $\tilde{H} = H/H_c$ and $\tau = \ln(H_c(t=0)/H_c(t))$, where $\tilde{H}$ and τ are the dimensionless mean curvature and time, respectively, and $H_c(t)$ and $H_c(t=0)$ are the critical mean curvature (as a function of time) and the critical mean curvature at the onset of coarsening. The critical mean curvature is the inverse of the critical radius at which the growth rate of a particle is

zero in the particulate system undergoing coarsening.

With the dimensionless coordinates defined, Eq. (6.16) is re-written in terms of a dimensionless mean curvature distribution, $f(\tilde{H}, \tau)$,

$$\frac{\partial f}{\partial \tau} + \frac{\partial}{\partial \tilde{H}} \left(f \frac{d\tilde{H}}{d\tau} \right) = 0 \ . \tag{6.17}$$

In the LSW theory, an additional transformation of time is performed such that the reference particle size (particle size that results in zero growth rate) is shifted from the critical mean curvature, H_c, to the minimum scaled mean curvature $\tilde{H}_m$. By this transformation, one obtains the scaled growth rate of a particle for a given $\tilde{H}$, $d\tilde{H}/d\tau$ expressed in terms of $\tilde{H}$ alone [32, 36],

$$\frac{d\tilde{H}}{d\tau} = \tilde{H} - \nu \left(\tilde{H}^4 - \tilde{H}^3 \right) \ , \tag{6.18}$$

where

$$\nu = \omega_{diff} H_c^4 \Big/ \frac{d\tilde{H}}{dt} \ , \tag{6.19}$$

and ω_{diff} is a rate of coarsening in isothermal two-phase alloy. The LSW theory shows that ν becomes a constant at very large τ and that there exists a maximum cut-off size of the particle size distribution (which corresponds to $\tilde{H}_m$). The scaled growth rate, $d\tilde{H}/d\tau$, is zero only at $\tilde{H} = \tilde{H}_m$, which results in two equalities: $d\tilde{H}/d\tau = 0$ and $d\left(d\tilde{H}/d\tau\right)/d\tilde{H} = 0$. On the basis of these two conditions, the values of ν and $\tilde{H}_m$ are evaluated as $-27/4$ and $2/3$, respectively [32, 36].

As an ansatz, we try a solution for Eq. (6.17) of the form

$$f(\tilde{H}, \tau) = \chi(\tau + \Psi) \Big/ \frac{d\tilde{H}}{d\tau} \ , \tag{6.20}$$

where both Ψ and $d\tilde{H}/d\tau$ are functions of only $\tilde{H}$. Substituting Eq. (6.20) into Eq.

(6.17), we find

$$\frac{\partial}{\partial\tau}\left(\frac{\chi}{\frac{d\tilde{H}}{d\tau}}\right)+\frac{\partial}{\partial\tilde{H}}\left(\frac{\chi}{\frac{d\tilde{H}}{d\tau}}\frac{d\tilde{H}}{d\tau}\right)=0\ , \tag{6.21}$$

$$\frac{d\chi}{d(\tau+\Psi)}\left(\frac{1}{\frac{d\tilde{H}}{d\tau}}\right)+\frac{d\chi}{d(\tau+\Psi)}\frac{\partial\Psi}{\partial\tilde{H}}=0\ ,$$

$$\frac{\partial\Psi}{\partial\tilde{H}}=-\left(\frac{1}{\frac{d\tilde{H}}{d\tau}}\right)\ .$$

The expressions for Ψ can be evaluated with an integral with variable upper limit of integration,

$$\begin{aligned}\Psi&=\int_{\infty}^{\tilde{H}}-\frac{1}{\frac{d\tilde{H}}{d\tau}}\,d\tilde{H}' \\ &=\int_{\infty}^{\tilde{H}}-\frac{1}{\tilde{H}'}+\frac{4}{3(3\tilde{H}'+1)}+\frac{5}{3(3\tilde{H}'-2)}-\frac{2}{(3\tilde{H}'-2)^2}\,d\tilde{H}' \\ &=-ln\tilde{H}+\frac{4}{9}ln(3\tilde{H}+1)+\frac{5}{9}ln(3\tilde{H}-2)+\frac{2}{3(3\tilde{H}-2)}-ln3\ .\end{aligned} \tag{6.22}$$

To determine the specific solution of Eq. (6.17) we must consider the volume fraction, Φ, expressed as

$$\begin{aligned}\Phi&=\int_{\tilde{H}_m}^{\infty}\frac{4}{3}\pi H_c^{-3}\tilde{H}^{-3}f(\tilde{H},\tau)\,d\tilde{H} \\ &=\int_{\tilde{H}_m}^{\infty}\frac{4}{3}\pi H_c(0)^{-3}e^{3\tau}\tilde{H}^{-3}\chi(\tau+\Psi)\Big/\frac{d\tilde{H}}{d\tau}\,d\tilde{H}\ .\end{aligned} \tag{6.23}$$

Since the volume fraction is conserved in the particulate system undergoing coarsening, this implies that the product $e^{3\tau}\chi(\tau+\Psi)$ must be independent of τ. Thus,

$$\chi(\tau+\Psi)=Be^{-3(\tau+\Psi)}, \tag{6.24}$$

where B is a numerical constant. Thus, the solution of Eq. (6.17) takes the form of

$$f(\tilde{H},\tau) = Be^{-3\tau}e^{-3\Psi}\Big/\frac{d\tilde{H}}{d\tau} \tag{6.25}$$

$$= Be^{-3\tau}3^3 4\frac{\tilde{H}^2 e^{\overline{2-3\tilde{H}}^{\,2}}}{(3\tilde{H}+1)^{\frac{7}{3}}(3\tilde{H}-2)^{\frac{11}{3}}} \ .$$

The total number of particles, $N_T(\tau)$, that changes with time can be determined as

$$N_T(\tau) = \int_{\tilde{H}_m}^{\infty} f(\tilde{H},\tau)\, d\tilde{H} \tag{6.26}$$

$$= -Be^{-3\tau}\int_{\infty}^{0} e^{-3\Psi}\, d\Psi$$

$$= \frac{B}{3}e^{-3\tau} \ .$$

After normalizing Eq. (6.25) by N_T, we then obtain the time-independent mean curvature distribution based on number density, $P(\tilde{H})^{\#}$,

$$P(\tilde{H})^{\#} = \frac{f(\tilde{H},\tau)}{N_v(\tau)} \tag{6.27}$$

$$= \frac{Be^{-3\tau}e^{-3\Psi}\Big/\frac{d\tilde{H}}{d\tau}}{\frac{B}{3}e^{-3\tau}}$$

$$= 3^4 4\frac{\tilde{H}^2 e^{\overline{2-3\tilde{H}}^{\,2}}}{(3\tilde{H}+1)^{\frac{7}{3}}(3\tilde{H}-2)^{\frac{11}{3}}} \ ,$$

which is equivalent to the particle size distribution presented in the LSW theory, but defined in the mean curvature space.

6.2.2.2 The Mean Curvature Distribution in Terms of Area Density

As in the mean curvature distribution based on number density derived above, the mean curvature distribution based on area density, $A_H(H,t)$, for the particulate system undergoing coarsening is also a function of H and t. The continuity equation in terms of a curvature distribution as a function of the two principal curvatures, Eq. (6.15) is expressed in the mean curvature space as

$$\frac{\partial A_H}{\partial t} + \frac{\partial}{\partial H}\left(A_H \frac{dH}{dt}\right) = -\frac{2A_H}{H}\frac{dH}{dt} \ , \tag{6.28}$$

where $v = dR/dt$ is substituted with $-(1/H^2)(dH/dt)$. The source/sink term due to topological singularities, Q_s, is omitted since the LSW theory neglects any discontinuous changes in the particle size [35, 36]. In addition, particles that are about to undergo topological singularity are very small in size and, thus, their interfacial areas contribute insignificantly to the mean curvature distribution based on area density. Equation (6.28) can be re-written in dimensionless coordinates, $\tilde{H}$ and τ, as

$$\frac{\partial A_H}{\partial \tau} + \frac{\partial}{\partial \tilde{H}}\left(A_H \frac{d\tilde{H}}{d\tau}\right) = -\frac{2A_H}{\tilde{H}}\frac{d\tilde{H}}{d\tau}. \tag{6.29}$$

Since the growth rate, $dH/d\tau$ is already defined in Eq. (6.18), as in Section 6.2.2.1, we try a solution of Eq. (6.29) in the form

$$A_H(\tilde{H},\tau) = \chi(\tau+\Psi)\tilde{H}^{-2}\Big/\frac{d\tilde{H}}{d\tau} \tag{6.30}$$

with both Ψ and $\frac{d\tilde{H}}{d\tau}$ depend only on $\tilde{H}$. Substituting Eq. (6.30) into Eq. (6.29) yields

$$\frac{\partial}{\partial \tau}\left(\frac{\chi}{\frac{d\tilde{H}}{d\tau}}\tilde{H}^{-2}\right) + \frac{\partial}{\partial \tilde{H}}\left(\frac{\chi\tilde{H}^{-2}}{\frac{d\tilde{H}}{d\tau}}\frac{d\tilde{H}}{d\tau}\right) = -\frac{2}{\tilde{H}}\frac{\chi\tilde{H}^{-2}}{\frac{d\tilde{H}}{d\tau}}\frac{d\tilde{H}}{d\tau} \ , \tag{6.31}$$

$$\frac{d\chi}{d(\tau+\Psi)}\left(\frac{\tilde{H}^{-2}}{\frac{d\tilde{H}}{d\tau}}\right)-2\tilde{H}^{-3}\chi+\tilde{H}^{-2}\frac{d\chi}{d(\tau+\Psi)}\frac{\partial\Psi}{\partial\tilde{H}}=-2\chi\tilde{H}^{-3}\ ,$$

$$\frac{\partial\Psi}{\partial\tilde{H}}=-\left(\frac{1}{\frac{d\tilde{H}}{d\tau}}\right)\ .$$

Thus, the expression for Ψ in terms of $\tilde{H}$ is identical to Eq. (6.22).

As in Section 6.2.2.1, the volume fraction, Φ, must be considered to obtain a unique solution to Eq. (6.29). The volume fraction in terms of A_H is expressed as

$$\Phi=\int_{\tilde{H}_m}^{\infty}\frac{1}{3}H_c^{-3}\tilde{H}^{-1}A_H(\tilde{H},\tau)\,d\tilde{H} \tag{6.32}$$

$$=\int_{\tilde{H}_m}^{\infty}\frac{1}{3}H_c(0)^{-3}e^{3\tau}\tilde{H}^{-3}\chi(\tau+\Psi)\Big/\frac{d\tilde{H}}{d\tau}\,d\tilde{H}, \tag{6.33}$$

which must be conserved. Thus, the product $e^{3\tau}\chi(\tau+\Psi)$ must be independent of τ and

$$\chi(\tau+\Psi)=Be^{-3(\tau+\Psi)}, \tag{6.34}$$

where B is a numerical constant. Consequently,

$$A_H(\tilde{H},\tau)=Ce^{-3\tau}e^{-3\Psi}\tilde{H}^{-2}\Big/\frac{d\tilde{H}}{d\tau} \tag{6.35}$$

$$=Ce^{-3\tau}3^3 4\frac{e^{\frac{2}{2-3\tilde{H}}}}{(3\tilde{H}+1)^{\frac{7}{3}}(3\tilde{H}-2)^{\frac{11}{3}}}. \tag{6.36}$$

The total surface area of a particular system, $A_T(\tau)$, is

$$A_T(\tau) = \int_{\tilde{H}_m}^{\infty} A_H(\tilde{H}, \tau)\, d\tilde{H} \tag{6.37}$$

$$= Ce^{-3\tau} \int_{\tilde{H}_m}^{\infty} \frac{e^{\overline{2-3\tilde{H}}^{2}}}{(3\tilde{H}+1)^{\frac{7}{3}}(3\tilde{H}-2)^{\frac{11}{3}}}\, d\tilde{H}. \tag{6.38}$$

We then obtain the time-independent mean curvature distribution based on area density, $P(\tilde{H})^A$, by

$$P(\tilde{H})^A = \frac{A_H(\tilde{H}, \tau)}{A_T(\tilde{H})} \tag{6.39}$$

$$= \frac{1}{h^A_{\tilde{H}}} \frac{e^{\overline{2-3\tilde{H}}^{2}}}{(3\tilde{H}+1)^{\frac{7}{3}}(3\tilde{H}-2)^{\frac{11}{3}}}, \tag{6.40}$$

where $h^A_{\tilde{H}} = 0.00320$ determined numerically using Maple. Figure 6.1 shows the plot of $P(\tilde{H})^{\#}$ and $P(\tilde{H})^A$ for comparison. Since the ratio of the two time-independent solutions, Eqs. (6.27) & (6.39), is a factor of $\tilde{H}^2$, Eq. (6.15) is valid in the case of spherical particles.

6.2.3 Application of the Continuity Equation for Coarsening of Complex Microstructures

To further validate the continuity equation, it must be applied to complex microstructures. We employ the bicontinuous structures presented in previous chapters, which evolve self-similarly. The continuity equation requires the expression of the average rate of changes of principal curvatures of all interfaces with the same principal curvatures, $\langle D\kappa_1/Dt \rangle_{\kappa_1,\kappa_2}$ and $\langle D\kappa_1/Dt \rangle_{\kappa_1,\kappa_2}$, in terms of the principal curvatures. Based on differential geometry, the rate of changes of principal curvatures at an in-

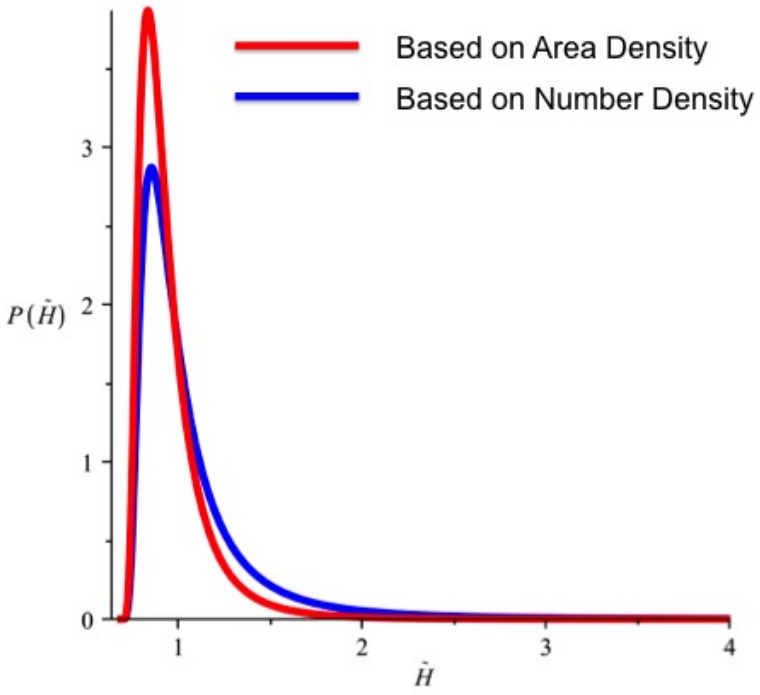

Figure 6.1: The time-independent mean curvature distribution based on number density, $P(\tilde{H})^{\#}$, and the mean curvature distribution based on area density, $P(\tilde{H})^{A}$ in mean curvature space for a particulate system undergoing coarsening.

terface can be expressed as

$$\frac{D\kappa_J}{Dt} = -\kappa_J^2 v - (v_{,11} + v_{,22}) \quad , \tag{6.41}$$

where different principal curvatures are denoted by subscript $J = 1$ or $J = 2$ [124]. The average rate of changes of principal curvatures of all interfaces with the same principal curvatures, $\langle D\kappa_J/dt \rangle_{\kappa_1,\kappa_2}$, then becomes

$$\left\langle \frac{D\kappa_J}{Dt} \right\rangle_{\kappa_1,\kappa_2} = -\kappa_J^2 \langle v \rangle_{\kappa_1,\kappa_2} - \langle \Delta_S v \rangle_{\kappa_1,\kappa_2} \quad , \tag{6.42}$$

where $\langle v \rangle_{\kappa_1,\kappa_2}$ and $\langle \Delta_S v \rangle \, \kappa_1, \kappa_2$ are the average velocity and the surface Laplacian of velocity of all interfaces with the same principal curvatures, respectively. Thus, the expression for $\langle D\kappa_1/dt \rangle_{\kappa_1,\kappa_2}$ and $\langle D\kappa_2/dt \rangle_{\kappa_1,\kappa_2}$ in terms of the principal curvatures can be obtained once we determine $\langle v \rangle_{\kappa_1,\kappa_2}$ and $\langle \Delta_S v \rangle_{\kappa_1,\kappa_2}$ in terms of the principal curvatures.

The expressions of $\langle v \rangle_{\kappa_1,\kappa_2}$ and $\langle \Delta_S v \rangle_{\kappa_1,\kappa_2}$ in terms of the two principal curvatures can be obtained with the same semi-analytical model presented in Chapter V. These expressions can then be substituted into the Eqs. (6.15) & (6.42) to analytically derive the time-independent ISD of the AC and CH bicontinuous structures already examined in this dissertation. As a note, the expression for $\langle v \rangle_{\kappa_1,\kappa_2}$ for the AC structure in terms of the principal curvatures is simply $-M(\kappa_1 + \kappa_2)/2$, where M is a proportionality constant. The predicted ISD from the solution of Eq. (6.15) should be compared with the calculated ISD to validate the continuity equation for complex microstructures. This work is still ongoing.

6.3 Morphological Evolution of a Rod Undergoing Pinching

Topological singularities play an important role in microstructural evolution during coarsening. As discussed in Chapter IV, a bicontinuous structure can decrease its overall interfacial area during coarsening by reducing the total net curvature or undergoing topological singularities. In the case of dendritic mixtures, topological singularities occur in the form of coalescence or pinching [96] while in bicontinuous structures, they occur in the form of pinching only [42]. The topological singularities present in complex microstructures alter their topologies. The most common measure of topology is the genus, which is a measure of number of handles in a structure. Past experiment and simulation results have shown that the scaled genus, $g_v S_v^{-3}$, where g_v is the genus per unit volume, remains constant for both dendrites and bicontinuous structures that evolve self-similarly [42, 96].

While the overall evolution of the bicontinuous structures has been carefully examined in the previous two chapters, our understanding of the evolution of the topological singularities present in these structures is still limited because of the difficulties involved in observing and quantitatively characterizing the details of the processes associated due to its rarity and short timescale. To focus our attention to topological singularity, we simulate pinching of a rod via conserved dynamics and nonconserved dynamics. The morphological evolution of the rod is examined locally using the isosurfaces colored with the mean and Gaussian curvatures and statistically using the interfacial shape distribution. The analysis can help identify general similarities and differences in morphologies and their evolution of the pinch-off of a rod simulated via different dynamics. Furthermore, as stated in Section 6.2, tracking the temporal evolution of ISD of a rod undergoing pinching should illustrate the discontinuous changes in interfacial curvatures during topological singularities.

6.3.1 Numerical Method

6.3.1.1 Structures

The initial morphology of the rod is defined using the hyperbolic tangent function. For a rod with the center axis parallel to the x-axis in a Cartesian grid system, the discretized order parameter, ϕ_{ijk}, where i, j, and k denote the indices for the position, can be constructed as

$$\phi_{ijk} = \frac{1}{2} + \frac{1}{2}\tanh\left[\frac{\sqrt{(i-x_c)^2 + (j-y_c)^2} - \left(R + \cos\left(\frac{2\pi x}{L}\right)\right)}{\frac{1}{2}\delta_{tanh}}\right] \quad , \tag{6.43}$$

where the variables x_c and y_c represent the Cartesian coordinates of the center of the rod, and x and L represent the x-coordinate and the length of the domain in the x-axis, respectively. The term $R + \cos(2\pi x/L)$ determines the radius of the rod, which varies with position along the x-axis. For $R = 15$, the maximum radius of the rod is 16 at the ends of the rod ($x = 0$ and $x = L$) while the minimum radius is 14 in the middle of the rod ($x = L/2$). The order parameter defined by Eq. (6.43) will have a bulk value of 0 inside of the rod and 1 outside. The variable δ_{tanh} represents the nondimensional interfacial thickness, which is defined as the region where the value of ϕ smoothly transitions between the two bulk values. Here, we use $\delta_{tanh} = 4.0$, which results in about four grid points across the interface, which is typical of phase-field simulations and is consistent with the parameters of the phase-field model employed.

6.3.1.2 Phase-field Simulation

The evolution of the rod is simulated using the phase-field method via conserved dynamics, Eq. (2.12), as well as nonconserved dynamics, Eq. (2.13). The order parameter from Eq. (6.43) is used as the initial condition in both simulations. From here onward, the rod simulated via Allen-Cahn dynamics is termed "the AC rod"

while the rod simulated via Cahn-Hilliard dynamics is termed "the CH rod." The simulation is carried out in a Cartesian grid system with domain size $[100, 60, 60]$ and a periodic boundary condition along the x-axis and no-flux boundary conditions along the y and z axes. The same values of parameters for the phase-field simulations of the AC structure (Chapter IV) and the CH structures (Chapter V) are employed to simulate the AC rod and the CH rod, respectively. The simulations are carried out until the initially continuous rods are pinched off and the remnants of the pinching have retracted.

6.3.1.3 Calculation of Interfacial Properties

To accurately calculate various curvatures, we apply the level-set smoothing method. We characterize the interfacial morphology of the rod and its remnant with the mean and the Gaussian curvatures, H and K, respectively, using the level-set approach presented in Chapter III. The two principal curvatures, $\kappa_1 = H - \sqrt{H^2 - K}$ and $\kappa_2 = H + \sqrt{H^2 - K}$, used in the calculation of ISD, are then evaluated based on the values of H and K.

6.3.2 Procedure for Analysis

6.3.2.1 Analysis of Local Morphologies and Their Evolution

The morphologies of the rods undergoing topological singularities are examined by generating the isosurfaces, which represent the interface, colored with the mean and Gaussian curvature values. All interfacial properties presented in this section are scaled by the characteristic length scale, S_v^{-1}.

6.3.2.2 Analysis of Overall Morphologies and Their Evolution

The overall morphologies of the rods and their evolution is examined by the ISD. Details of the ISD and its calculation procedure can be found in Section 2.1.2. The

range of the color bar is saturated at $P(\kappa_1, \kappa_2) = 0.2$ to better observe the curvature evolution of the area of interfaces having the largest magnitude of curvatures in the middle of the rod, which are rapidly evolving during the pinching event.

6.3.3 Results & Discussion

6.3.3.1 Local Morphological Evolution of the Rods

Figure 6.2 shows the morphology of the CH rod undergoing topological singularity via conserved dynamics colored with the mean and Gaussian curvatures at select nondimensional times. The isosurfaces representing the interface show that the narrowest region in the middle of the rod shrinks to the point of singularity at some simulation time between $t = 500,000$ (the last output prior to pinching) and $t = 510,000$ (the first output after pinching). After pinching, the caps that remain from pinching retract.

The interfacial morphology also reveal that the CH rod possesses positive mean curvatures throughout the structure at all simulation times, both before and after pinching. In terms of Gaussian curvatures, the CH rod prior to pinching possesses positive Gaussian curvatures (elliptic-shape) at the ends of the rod and of negative Gaussian curvatures (saddle-shape) in the middle of the rod. Once the CH rod pinches off, the spherical caps, which are remnants of pinching, have positive Gaussian curvatures (elliptic-shape). Since the CH rod is simulated via conserved dynamics, as the middle region of the rod shrinks away, the end regions of the rod must expand in order to conserve the overall volume fractions. This retraction, as well as the expansion, is shown in Fig. 6.2a and c, where the value of mean curvature increases in the middle of the CH rod while it decreases in the ends of the rod as the structure approaches singularity. After pinching, the initially cone-shaped caps retract to the ends of the domain and become more spherical, as evidenced by the decrease in the value of mean curvature at the tips of the caps shown in Fig. 6.2e and g.

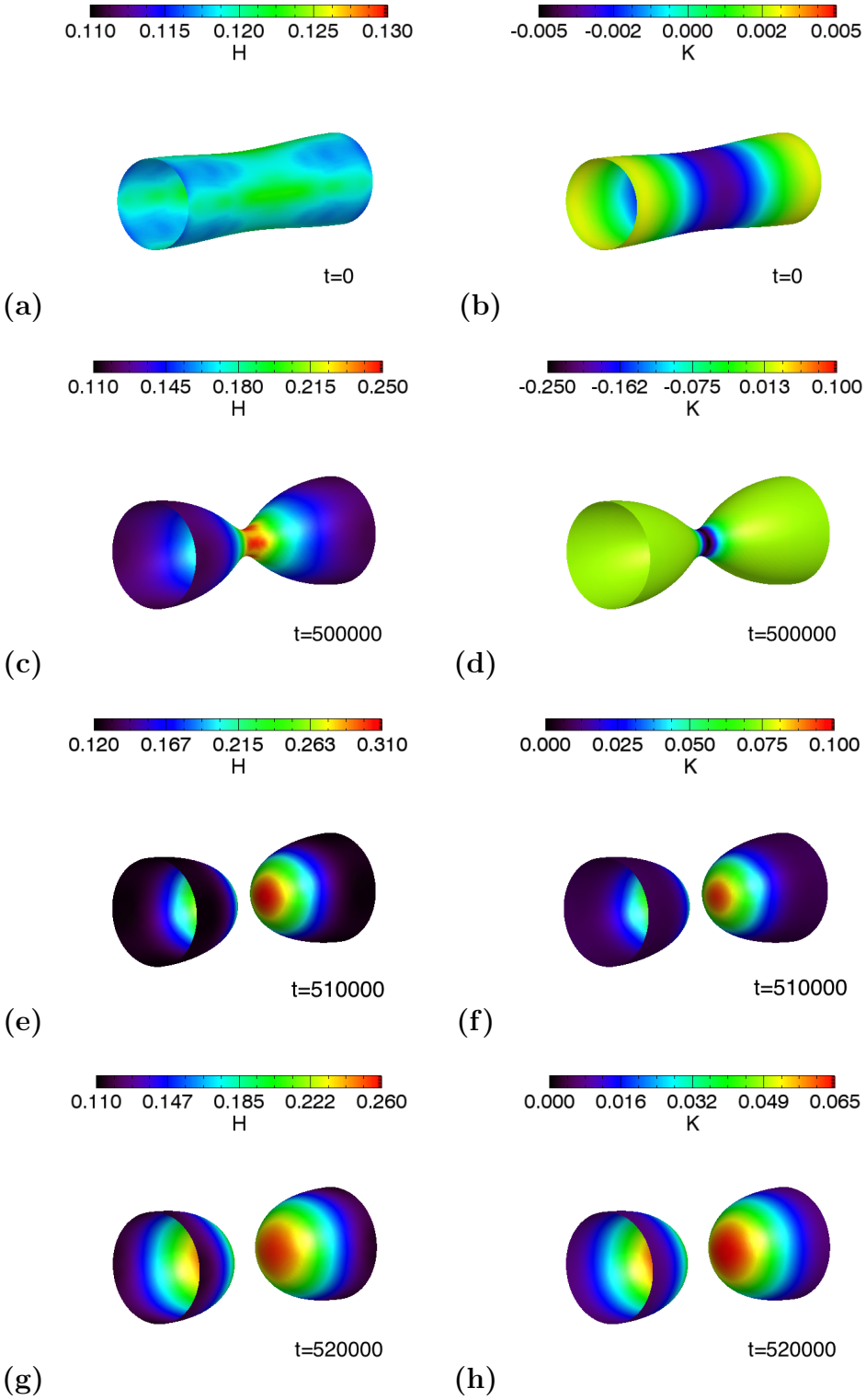

Figure 6.2: Morphologies of the rod undergoing topological singularity via conserved dynamics, with the interface colored with the mean and Gaussian curvatures at nondimensional time of (a) & (b) $t = 0$, (c) & (d) $t = 500,000$, (e) & (f) $t = 510,000$, and (g) & (h) $t = 520,000$.

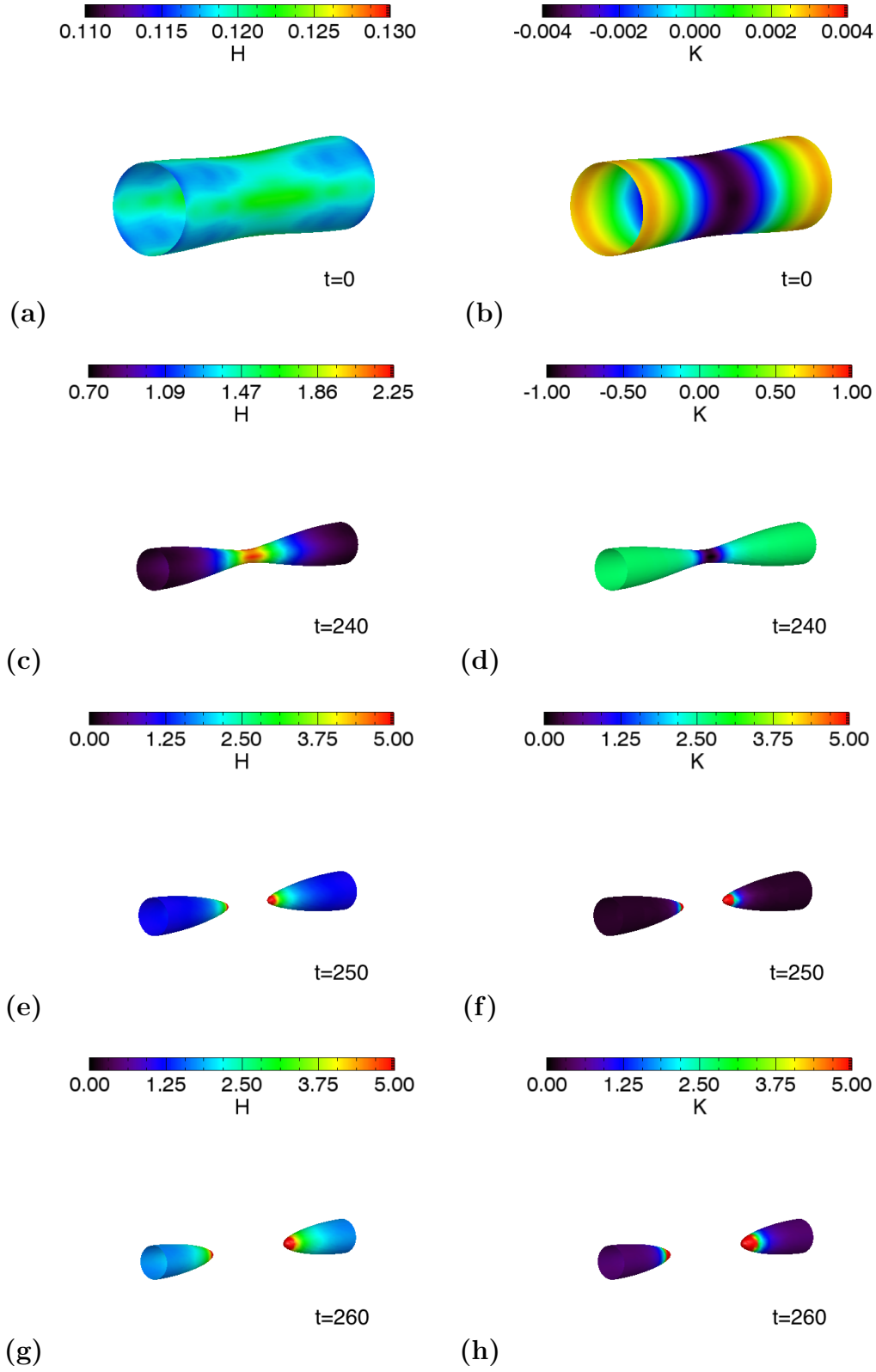

Figure 6.3: Morphologies undergoing topological singularity via nonconserved dynamics, with the interface colored with the mean and Gaussian curvatures at nondimensional time of (a) & (b) $t = 0$, (c) & (d) $t = 240$, (e) & (f) $t = 250$, and (g) & (h) $t = 260$.

The morphological evolution of the AC rod undergoing topological singularity via nonconserved dynamics is also examined, as presented in Fig. 6.3. The isosurfaces representing the interface show that the AC rod pinches off at some simulation time between $t = 240$ (the last output prior to pinching) and $t = 250$ (the first output after pinching). At $t = 260$ (the second output after pinching) the caps that remain from pinching retract. Clearly, there are some general similarities between the evolution of the AC rod and the CH rod. For example, both rods possess positive mean curvatures at all times. Both have negative Gaussian curvature in the middle of the rod and positive Gaussian curvature at the edges of the rod before pinching and only positive Gaussian curvature after pinching.

The key difference between the evolution of the CH rod and the AC rod is that, in the latter case, the rod shrinks almost uniformly over its length without preserving the volume fraction. As a result, the mean curvature of the AC rod at the onset of pinching is much larger than that of the CH rod at a similar evolution time, as shown in Figs. 6.2d & 6.3d, respectively. This difference in evolution is also evident after pinching when the cone-shaped caps in the AC rod maintain their general shape, unlike the ends of the CH rod that become more spherical as they retract.

The above results indicate that the primary difference between Cahn-Hilliard and Allen-Cahn dynamics in this example is the change in the volume fraction in the latter case. To test this conjuncture, we apply the modified Allen-Cahn equation,

$$\frac{\partial \phi}{\partial t} = -L_\phi \left(\frac{dg}{d\phi} - \epsilon^2 \nabla^2 \phi + \frac{1}{|\Omega|} \int_\Omega \frac{dg}{d\phi} \, dV \right) \quad , \tag{6.44}$$

where Ω is the overall domain of the problem [128], in which volume fraction change is prohibited. The rod simulated via the modified Allen-Cahn equation is referred to as the volume-conserving AC rod. The results are shown in Fig. 6.4, in which the volume-conserving AC rod undergoes pinching at some simulation time between

$t = 4,800$ (the last output prior to pinching) and $t = 5,000$ (the first output after pinching). At $t = 5,200$ (the second output after pinching) the caps that remain from pinching retract. It is evident that the morphological evolution for volume-conserving Allen-Cahn dynamics is closely resembles that of the CH case shown in Figs. 6.2. This supports our conjecture that the volume fraction change in the Allen-Cahn dynamics is the main source of the difference in the morphological evolution. The similarity between the morphology of the CH rod and the volume-conserving AC rod will be quantified in the latter part of this section using the ISD.

6.3.4 Evolution of the Interfacial Shape Distributions of the Rods

The statistical description of the morphology of the CH rod at select times is represented by the ISD in Fig. 6.5. At $t = 0$, the ISD is centered as a point along $\kappa_1 = 0$ (cylindrical shape), which indicates small variations in curvature of the initial geometry of the CH rod, as shown in Fig. 6.2a and b. At the onset of pinching, as shown in Fig. 6.5b, the ISD is located in the first and second quadrants of the ISD map. The ISD in the first quadrant ($\kappa_1 > 0, \kappa_2 > 0$) represents interfaces at the ends of the rod that have elliptic shapes. On the other hand, the ISD in the second quadrant ($\kappa_1 < 0, \kappa_2 > 0$) represents interfaces in the middle of the rod that have saddle shapes, which can be seen in Fig. 6.2c and d. This finding is consistent with the thinnest part of the still connected rod having negative Gaussian curvatures (saddle-shapes). After pinching at $t = 510,000$, the ISD is only present in the first quadrant, as shown in Fig. 6.5c. The discontinuous change in the interfacial curvature during topological singularity is evident when we compare the principal curvatures of the interfaces with the largest net curvatures (furthest from the origin on the ISD map) at $t = 500,000$ and at $t = 510,000$. Before pinching, interfaces with the largest net curvature have principal curvatures with opposite signs, which belong to the second quadrant of the ISD map (Fig. 6.5b). In contrast, after pinching, interfaces with the

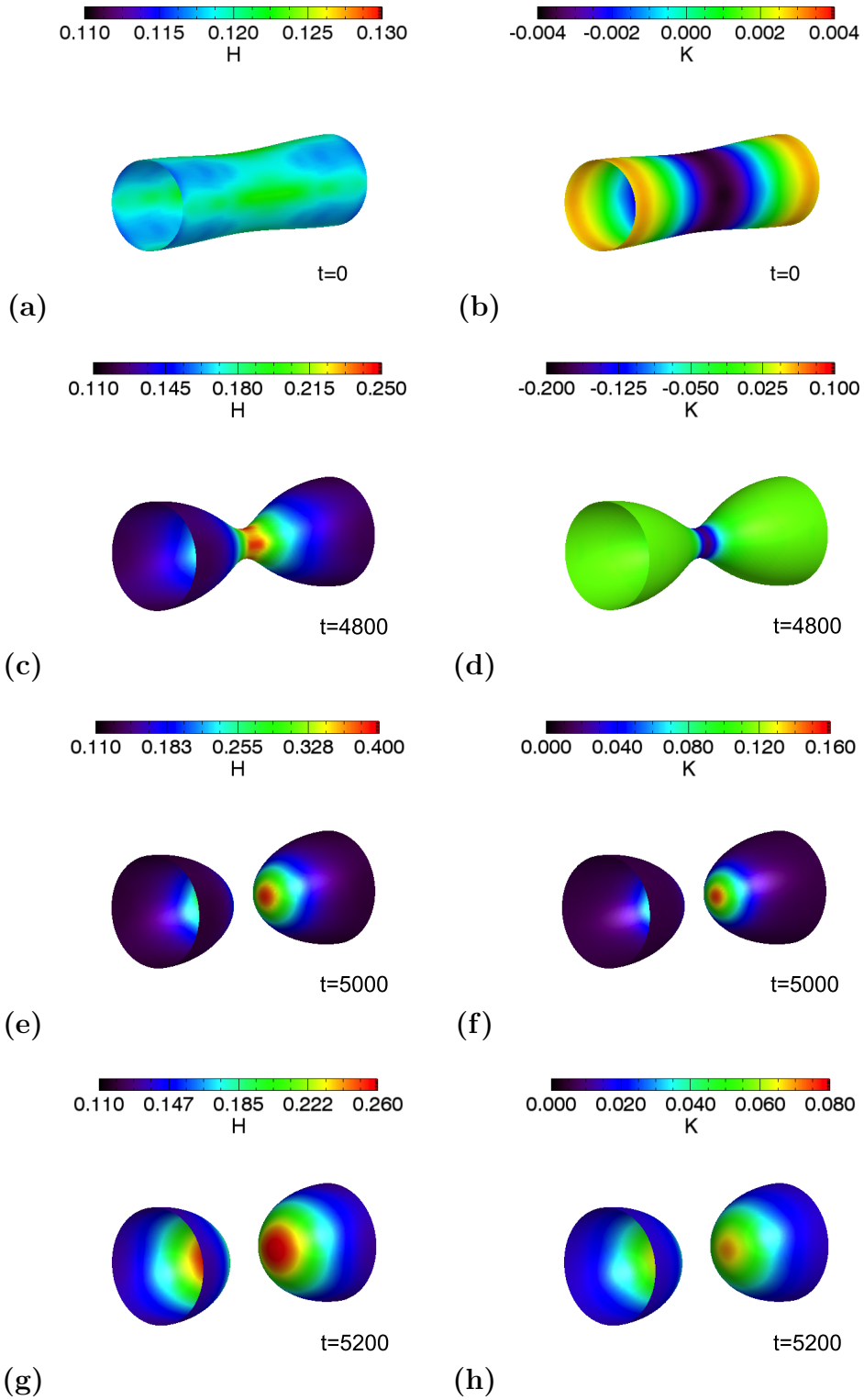

Figure 6.4: Morphologies undergoing topological singularity via volume-conserving Allen-Cahn dynamics, Eq. (6.44), with the interface colored with the mean and Gaussian curvatures at nondimensional time of (a) & (b) $t = 0$, (c) & (d) $t = 4800$, (e) & (f) $t = 5000$, and (g) & (h) $t = 5200$.

largest net curvature have principal curvatures with same sign, which belong to the first quadrant (Fig. 6.5c). This change is the result of the pinching, which generates two caps (belonging to the first quadrant) from a narrow neck of the rod (belonging to the second quadrant). At $t = 520,000$, the ISD (colored in red) is located closer to the origin of the ISD map compared to that at $t = 510,000$, indicating that the net curvatures of the caps decrease as they retract.

We also examine the overall morphology of the AC rod at select times using the ISD, which is shown in Fig. 6.6. Similar to the ISD of the CH rod, the ISD of the AC rod shows distributions located in the first and second quadrants before pinching and in only the first quadrant after pinching. Furthermore, the discontinuous change in the interfacial curvature during topological singularity is also evident in the AC rod. At $t = 240$, interfaces with largest net curvature have principal curvatures with opposite signs (second quadrant of the ISD map), as shown in Fig. 6.6b. In contrast, at $t = 250$, interfaces with largest net curvature have principal curvatures with same sign (first quadrant of the ISD map), as shown in Fig. 6.6c. However, the values of the net curvatures of the interfaces of the two rods are very different. In general, the interfaces of the AC rod have larger net curvature than those of the CH rod as a result of uniform shrinkage during pinching.

We have also examined the ISDs of the volume-conserving AC rod at select times, as shown in Fig. 6.7. As evidenced by the isosurface plots, the results are similar to the ISDs of the CH rod shown in Fig. 6.5. For ease of comparison, the ISDs of the CH rod (green) and that of the volume-conserving AC rod (red) are overplotted, as shown in Fig. 6.8. The ISDs are capped at $P(\kappa_1, \kappa_2) = 0.1$. Surprisingly, the ISDs of the two rods at similar evolution times are both qualitatively and quantitatively similar, as indicated by the overlapping ISD. The difference between the two ISDs seen in Fig. 6.8b is likely due to the different state in the evolution, as the outputs were not available at the exact match. This finding demonstrates that the conserved dynamics

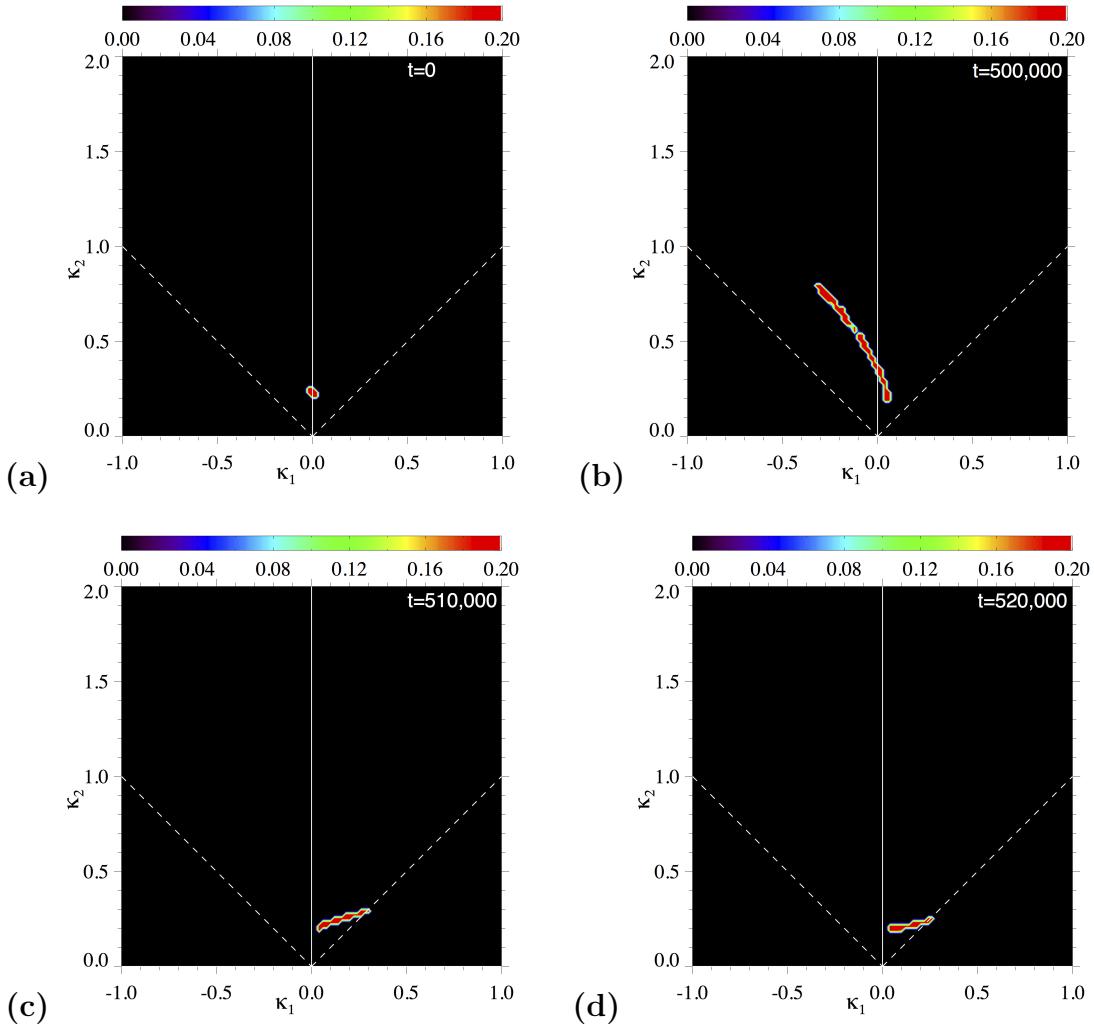

Figure 6.5: Interfacial shape distribution of the rod undergoing topological singularity via conserved dynamics at nondimensional time of (a) $t = 0$, (b) $t = 500,000$, (c) $t = 510,000$, and (d) $t = 520,000$. The maximum of the color bar range is set at $P(\kappa_1, \kappa_2) = 0.2$ to highlight the curvature evolution of the interfaces that are involved in pinching and have large magnitudes of curvatures. The rod pinches off at some simulation time between (b) $t = 500,000$ and (c) $t = 510,000$.

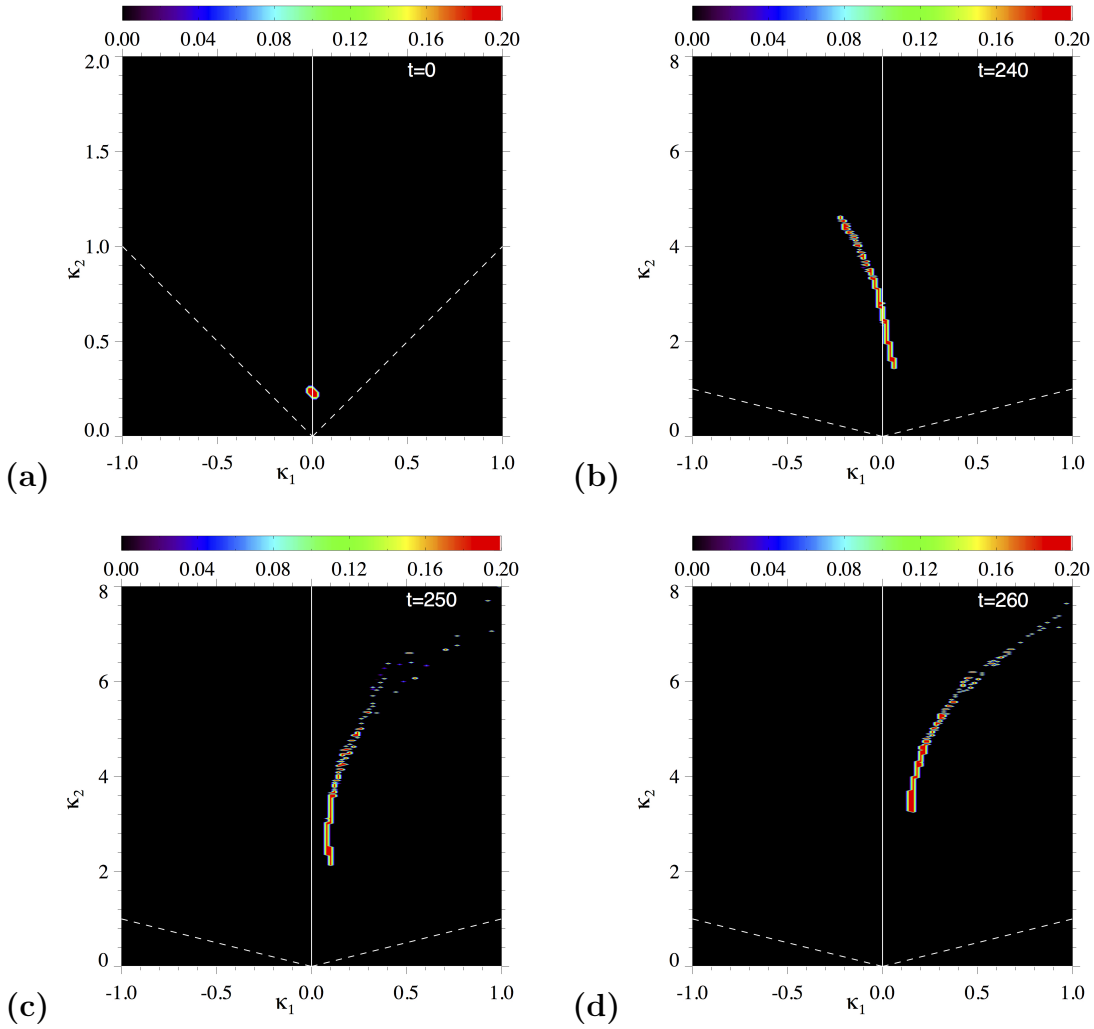

Figure 6.6: Interfacial shape distribution of the rod undergoing topological singularity via nonconserved dynamics at nondimensional time at (a) $t = 0$, (b) $t = 240$, (c) $t = 250$ and (d) $t = 260$. The maximum of the color bar range is set at $P(\kappa_1, \kappa_2) = 0.2$ to highlight the curvature evolution of the interfaces that are involved in pinching and have large magnitudes of curvatures. The rod pinches off at some simulation time between (b) $t = 240$ and (c) $t = 250$.

and the modified Allen-Cahn dynamics yield similar morphological evolution but have different rate of evolution, at least when pinching is considered. Whether this similarity holds for evolution in general should be examined by simulating coarsening using the volume-conserving Allen-Cahn dynamics with an initial condition obtained from the Cahn-Hilliard dynamics.

Finally, the temporal evolution of the ISD verifies the discontinuous changes in the interfacial curvatures during topological singularity, which gives rise to the source term Q_s in the continuity equation in terms of the ISD presented in the previous section. Detailed analysis of these simulations can provide the form of Q_s, which is left for future work.

6.4 Conclusion

This chapter described preliminary work that is still on going. In the first part of the chapter, a general continuity equation of interfacial area is derived to develop the theory of coarsening. As in the LSW theory, we can predict the overall morphology of complex structures by solving the continuity equation in terms of the ISD to obtain the time-independent ISD. We find that the key difference between the continuity equation in terms of the particle size distribution based on number density (presented in the LSW theory) and in terms of the curvature distribution based on area density (presented in this chapter) is the existence of the source/sink term. The source/sink term accounts for the rate of generation/loss of surface area during the evolution.

In order to validate the derived continuity equation, we apply the equation to a system of spherical particles undergoing coarsening and solve for the time-independent curvature distribution based on area density, employing the same assumptions as the LSW theory. We find that the continuity equation can accurately describe the evolution of the curvature distribution based on area density of spherical particles. To further validate the continuity equation, it must be applied to coarsening of complex

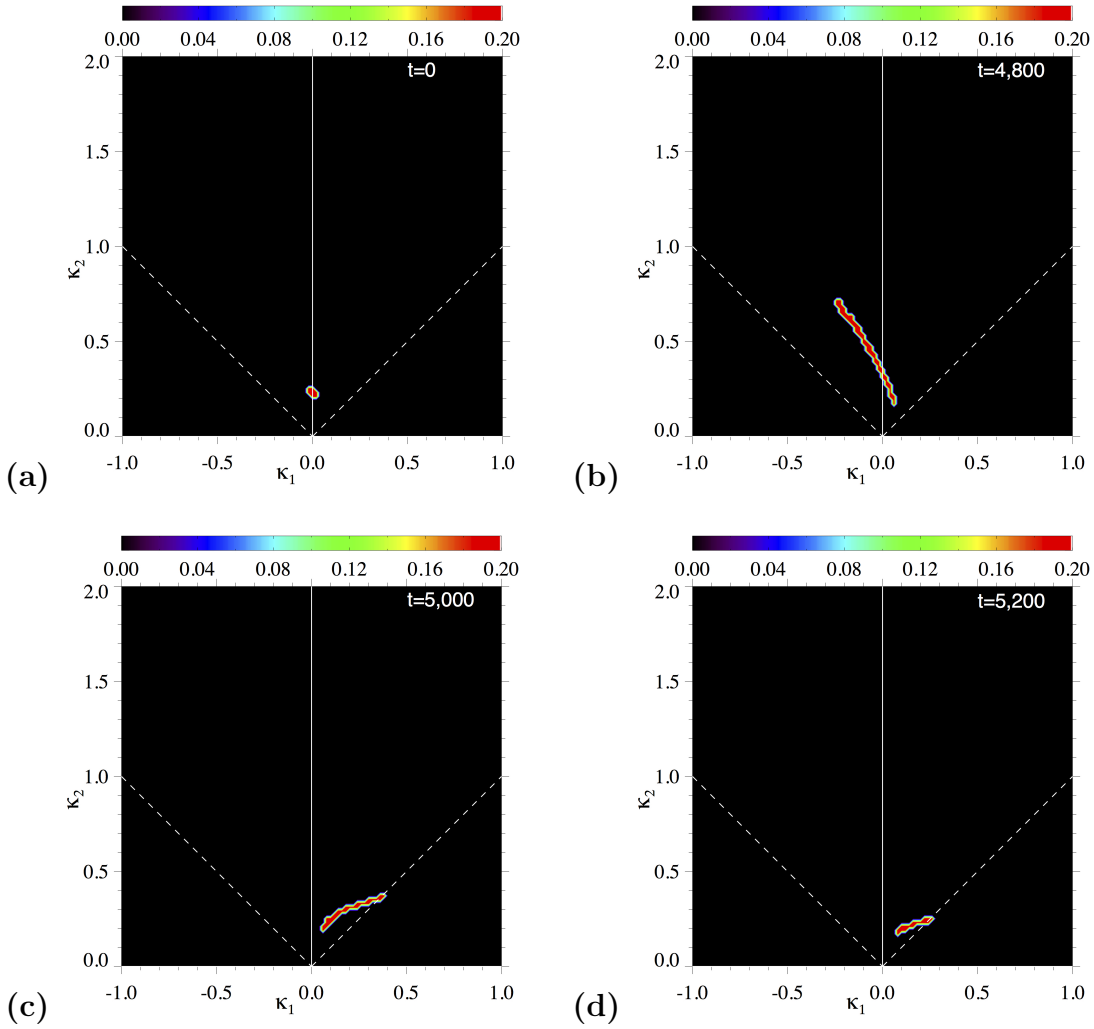

Figure 6.7: Interfacial shape distribution of the rod undergoing topological singularity via volume-conserving Allen-Cahn dynamics, Eq. (6.44), at nondimensional time at (a) $t = 0$, (b) $t = 4,800$, (c) $t = 5,000$ and (d) $t = 5,200$. The maximum of the color bar range is set at $P(\kappa_1, \kappa_2) = 0.2$ to highlight the curvature evolution of the interfaces that are involved in pinching and have large magnitudes of curvatures. The rod pinches off at some simulation time between (b) $t = 4,800$ and (c) $t = 5,000$.

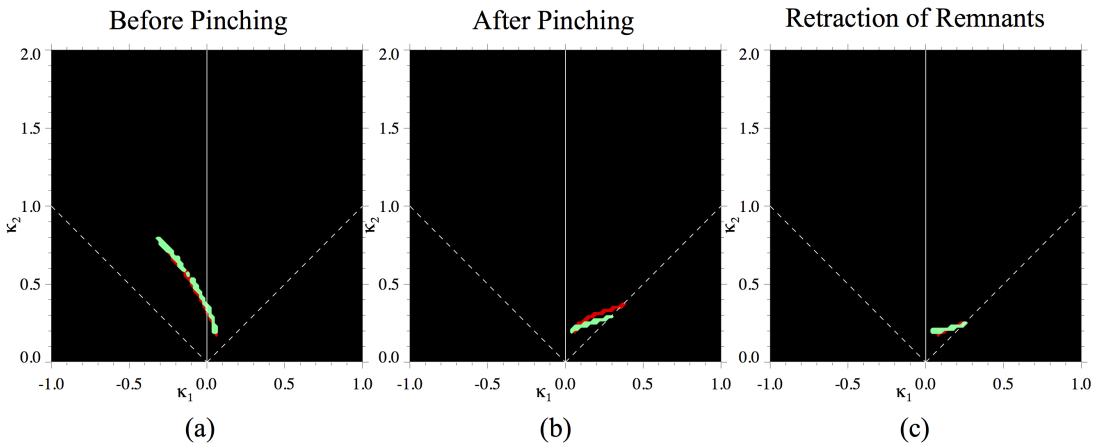

Figure 6.8: Interfacial shape distributions of the volume-conserving AC rod (red) and the CH rod (green) at nondimensional time at (a) $t = 4,800$ and $t = 500,000$, respectively, (b) $t = 5,000$ and $t = 510,000$, respectively, and (c) $t = 5200$ and $t = 520,000$, respectively. The ISD is drawn based on the contour of $P(\kappa_1, \kappa_2) = 0.1$.

microstructures, where the kinetics is more complex. This work is ongoing and is discussed further as a future work in the next chapter.

In the second part of this chapter, we examined the morphological evolution of a rod undergoing pinching, which is simulated via conserved and nonconserved dynamics. We find that the rod evolving via nonconserved dynamics possess larger net curvature than that evolving via conserved dynamics because the former shrinks almost uniformly over its long axis without preserving the volume fraction. On the other hand, when volume-conserving AC dynamics was employed to evolve the rod, the morphologies of the rod become remarkably similar to the CH rod. The result demonstrates that the conserved dynamics and the volume-conserving Allen-Cahn dynamics yield similar morphological evolution but have different rate of evolution. The ISDs of the simulated rods at different evolution times shows the discontinuous changes in the interfacial curvatures during topological singularity, which gives rise to the source/sink term that account for topological singularities, Q_s, in the continuity equation. The results can be further analyzed to develop the functional form of Q_s that could be used in the continuity equation.

CHAPTER VII

Summary, Potential Application, and Future work

7.1 Summary

In this dissertation, we investigated the morphological evolution of complex structures undergoing coarsening in an effort to develop a general theory of coarsening for microstructures with intricate morphologies. We begin with a simplified mathematical description of the coarsening process, based solely on the thermodynamic driving force from interfacial free energy. Computational approaches can then be used to simulate the coarsening dynamics in order to gain insights into the process. We simulated coarsening of bicontinuous structures via conserved and nonconserved dynamics using the phase-field method.

Development of the theory of coarsening requires accurate quantification of morphological evolution, which is obtained from the calculation of various interfacial properties. In Chapter III, we present an algorithm, "level-set smoothing," that smoothes voxel-based data describing the interfaces with minimal shift in the interfaces so that interfacial properties can be accurately calculated. The level-set smoothing method is a set of sequential data-processing schemes that consists of first generating the signed distance function for the given microstructure using the level-set method, followed by smoothing via diffusion. We also present numerical algorithms to calculate various types of interfacial properties, such as the curvatures and their rate of changes, the

latter of which can be calculated by either the convective or the advective method. Detailed error analysis shows that the advective method yields more accurate results for rate of change of curvatures than the convective method. With the development of the level-set smoothing method and the advective method, we proceed to investigate the morphological evolution in complex structures.

As a framework for theory development, we propose to consider the interfacial evolution during coarsening as a consequence of (i) the interfacial velocity induced by diffusion and (ii) the resulting evolution of the interfacial curvatures. In Chapter IV, we have used the AC structure simulated via nonconserved dynamics as a test bed to investigate the evolution of curvatures, (ii). We find that the evolution proceeds with some interfaces evolving toward topological singularities (pinching) while the majority of interfaces flatten. These two processes were also illustrated through the evolution equation for the mean curvature, which has a term that depends solely on the local curvatures, as well as a term that is proportional to the surface Laplacian of the mean curvature. The first term causes increase in the magnitude of the mean curvature, while the second term causes smoothing of the mean curvature in a manner similar to diffusion of chemical species on a surface. The second term causes a large dispersion in the values of rate of change of the mean curvature at various locations in the structure. The origin of the dispersion is nonlocal, and it cannot be characterized by the local curvatures or shape of a patch of interface.

Chapter V extends the analyses to the coarsening of the three CH structures simulated via conserved dynamics. This dynamics is more complex than nonconserved dynamics since long-range diffusion dictates the kinetics. We find general correlations between interfacial velocity and the mean curvature, as well as between interfacial velocity and the surface Laplacian of mean curvature. Furthermore, we discover that the normal velocities of interfaces with the same local principal curvatures have a Gaussian distribution, independent of the principal curvature values and the volume

fractions of the structures. Based on the correlations obtained, we develop a semi-analytical model in order to predict the rate of change of the mean curvature.

Chapter VI discusses preliminary work that require further investigation. In the first half of the chapter, we derive a general continuity equation of interfacial area in terms of the interfacial shape distribution. The validation of the continuity equation is still ongoing. In the second half of the chapter, we examine the morphological evolution of a rod undergoing pinching, resulting in a topological singularity. The analysis confirms that there are discontinuous changes in interfacial curvatures during topological singularities, which gives rise to a source term in the continuity equation.

7.2 Potential Application

With advances in experimental and computational techniques, three-dimensional microstructural data have become more accessible for analysis [89, 90, 91]. Regardless of the technique employed to obtain the microstructure, the reconstructed data often require processing before any analysis can be done. The level-set smoothing method presented in this dissertation is a computationally efficient data processing algorithm that can be applied to any three-dimensional microstructure. The algorithm is designed to smooth the interfaces with minimal shifts in the interfacial location to preserve the original morphology. Thus, the method can be widely utilized in the analysis of microstructures that requires accurate calculation of various interfacial quantities.

In addition, the characterization techniques presented in this dissertation can also be employed to examine the dynamics of the evolution in other complex microstructures. The correlations between dynamic interfacial quantities, such as interfacial velocity or rate of change of curvature, and static interfacial properties, such as curvatures, must be understood in order to elucidate the complex dynamics of coarsening. This can be achieved by employing both statistical and local analysis; the statisti-

cal analysis shows the general relationship among the static and dynamic interfacial quantities, while the examination of local morphologies and their evolution can be used to confirm these relationships and identify any outliers. Furthermore, since the semi-analytical model adopted to predict curvature evolution is based on differential geometry, the approach is not limited to the coarsening kinetics presented in this dissertation. For example, such an approach can be applied to solidification.

7.3 Future Work

The work presented in this dissertation represents significant progress in the development of theory of coarsening in complex structures. This section highlights possible future work that can further advance the theory development.

As discussed in Chapter VI (preliminary works), the continuity equation of interfacial area must be validated with microstructures with complex morphologies, in particular the bicontinuous structures analyzed in this dissertation. A valid continuity equation in terms of the ISD will enable the prediction of the evolution of the overall morphology of a microstructure undergoing coarsening. The semi-analytical model presented in Chapter V provides the expressions for the average rate of changes of principal curvatures when the expressions can be numerically determined for the average velocity and for the surface Laplacian of velocity in terms of the principal curvatures. In addition, the functional form of the source/sink term that account for topological singularity, Q_s, also needs to be derived. As a next step, these expressions can be substituted into the continuity equation to predict ISD. This ISD should be compared with the calculated ISD to validate the continuity equation. Once the continuity equation is validated with the bicontinuous structures, the semi-analytical model and the continuity equation can be employed to investigate the morphological evolution of other types of microstructures with more complex kinetics, including those observed in experiments. Another topic of interest mentioned in Chapter VI

is to examine the morphological evolution complex structures during coarsening via volume-conserving Allen-Cahn dynamics with an initial condition obtained from the Cahn-Hilliard dynamics. This simulation should verify if the Cahn-Hilliard dynamics and the volume-conserving Allen-Cahn dynamics induce similar morphological evolution independent of the morphology of the initial condition as indicated by the evolution of pinching rods.

While the bicontinuous structures examined in this dissertation have constant mobility between the two phases, many of the two-phase alloys found in nature have different diffusion coefficients for each phase. Domain coarsening with unequal mobility between the two phases can be simulated with the phase-field method. To model microstructural evolution following spinodal decomposition with unequal mobility, the modified Cahn-Hilliard equation with concentration dependent mobility term is given by

$$\frac{\partial \phi}{\partial t} = \nabla \cdot \left(L_\phi(\phi)\, \nabla \frac{\delta G}{\delta \phi} \right) \ , \tag{7.1}$$

where $\delta G/\delta\phi$ is the variational derivative of the free energy functional, also known as the chemical potential, and $L_\phi(\phi)$ is the concentration dependent mobility term. This equation is identical to Eq. (2.13) except for the fact that L_ϕ is dependent on ϕ. In one of the earlier works that investigated the microstructural evolution with variable mobility, Sappelt et al. [129] have used

$$L_\phi(\phi) = \frac{1}{\exp\left[\alpha\left(\phi - \phi_g\right)\right] + 1} \ , \tag{7.2}$$

where α is a large positive constant and ϕ_g is the equilibrium value of the order parameter in the glass-forming phase (ϕ varies between -1 and 1). In this setup, provided that α is large enough, $L_\phi(\phi) \approx 1$ for $\phi < \phi_g$ and $L_\phi(\phi) \approx 0$ for $\phi > \phi_g$. In the two-dimensional simulations performed by Sappelt et al. using Eqs. (7.1) & (7.2), they found that the temporal growth law of $\langle R \rangle \propto t^{1/3}$ only holds if the volume

fraction of the phase with higher mobility is greater than 40%. In a similar work, Sheng et al. [130] have used

$$L_\phi(\phi) = \frac{1+\phi}{2} \ , \tag{7.3}$$

as the expression for the mobility coefficient, with $\phi = \pm 1$ as the equilibrium values, to examine the microstructural evolution following spinodal decomposition. In this setup, $L_\phi(\phi) = 1$ for $\phi = 1$ and $L_\phi(\phi) = 0$ for $\phi = -1$. With this setup, Sheng et al. have found that the growth law becomes $\langle R \rangle \propto t^{3/10}$. They tested five different expressions for $L_\phi(\phi)$, and found that the $\sim t^{1/3}$ growth law holds as long as the ratio of the smaller mobility coefficient to the larger one is greater than 0.2 regardless of the exact form of $L_\phi(\phi)$. These results demonstrate the introduction of the concentration dependent mobility can alter the coarsening rate from that reported by the LSW theory. However, it is still unclear how the morphology and its evolution is affected by the unequal mobility. As a first step, three-dimensional morphological evolution during coarsening with constant mobility, with unequal mobility which results in the $\sim t^{1/3}$ growth law, and with unequal mobility which does not result in the $\sim t^{1/3}$ growth law can be compared

Another complexity that can be added to the coarsening dynamics is the anisotropy in the interfacial energy. The anisotropy in the interfacial energy arises from the crystalline nature of solids, where the interfacial energy is a function of the crystallographic orientation. Coarsening of microstructures with anisotropy in interfacial energy can also be simulated with the phase-field method. Eggleston et al. have used the same free energy functional presented in Chapter II, Eq. (2.8), but with a gradient energy coefficient, $\epsilon(\theta)$, that depends on the orientation,

$$\epsilon(\theta) = \epsilon_0 \left(1 + \epsilon_4 \cos 4\theta\right) \ , \tag{7.4}$$

where θ is the angle between the normal to the surface and the x-axis, ϵ_0 and ϵ_4

are positive constants (the latter of which determines the degree of anisotropy), to describe the anisotropy in interfacial energy with four-fold symmetry [131]. With sufficiently large degree of anisotropy, there could be a range of interfacial orientations that are unstable, referred to as missing orientations, which give rise to sharp corners in the equilibrium particle shape. At these missing orientations, the evolution equation becomes ill-posed [131, 132]. These missing orientations can be determined by plotting the polar plot of $1/\epsilon$ and identifying the non-convex regions, as shown in Fig. 7.1. To convexify the polar plot, the common tangent approach can be applied [133]. Eggleston et al. modified the gradient energy coefficient as

$$\tilde{\epsilon} = \begin{cases} \epsilon(\theta_m) & \text{for non-missing orientations} \\ \dfrac{\epsilon(\theta)\cos\theta}{\cos\theta_m} & \text{for missing orientations} \end{cases} , \tag{7.5}$$

where θ_m is the angle at which the polar plot intersects the tangent plot, as shown in Fig. 7.1. With the regularized gradient energy coefficient $\tilde{\epsilon}$, the expression for the chemical potential in two dimensions is given by

$$\mu = \frac{dg}{d\phi} - \nabla \cdot \left(\tilde{\epsilon}^2 \nabla\phi\right) + \frac{\partial}{\partial x}\left(\tilde{\epsilon}\frac{d\tilde{\epsilon}}{d\theta}\frac{\partial\phi}{\partial y}\right) - \frac{\partial}{\partial y}\left(\tilde{\epsilon}\frac{d\tilde{\epsilon}}{d\theta}\frac{\partial\phi}{\partial x}\right) . \tag{7.6}$$

While the phase-field model presented by Eggleston et al. has accurately simulated equilibrium shapes of particles with highly anisotropic interfacial energy, Hausser et al. argue that convexifying the gradient energy coefficient prevents the model from capturing the nucleation of facets [134]. To circumvent this problem, Wise et al. introduced an extra regularization term in the free energy functional,

$$G = \int_{\Omega} \left\{ g\left(\phi\right) + \frac{\epsilon^2}{2}\left|\gamma(\vec{n})\nabla\phi\right|^2 + \frac{\delta^2}{2}\left(\nabla^2\phi\right)^2 \right\} dV , \tag{7.7}$$

where $\gamma\left(\vec{n}\right)$ is the interfacial energy as a function of normal to the surface (which

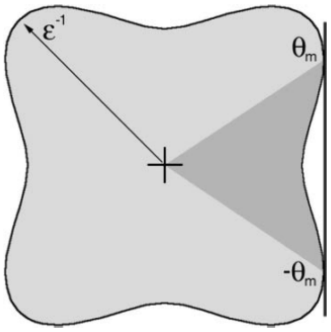

Figure 7.1: Polar plot of $1/\epsilon$ as a function of θ. The orientations corresponding to non-convexity are the missing orientations in the equilibrium particle shape. The vertical tangent line intersects the polar plot at angles $\pm\theta_m$. Adapted with permission from [131]. Copyright 2016 by Elsevier.

is not convexified) and δ is the regularization parameter [132]. The following free-energy functional leads to a nonlinear sixth-order evolution equation for ϕ, which can be numerically iterated using the implicit time-discretization scheme for computational efficiency. While Wise et al. have used the aforementioned model to simulate coarsening of corrugated surface via surface diffusion, a similar approach can be applied to simulate coarsening via bulk-diffusion with anisotropy in interfacial energy. With such a model, one can examine the morphological evolution of complex microstructure by applying the same set of statistical analysis techniques developed in this dissertation. Specifically, insights can be gained by comparing the morphological evolution of complex microstructures undergoing coarsening with constant mobility and isotropic interfacial energy, unequal mobility and isotropic interfacial energy, and equal mobility and anisotropic interfacial energy.

The evolution of experimental microstructures should also be examined and compared with that of the simulated structures under different dynamics. An example of an experimental microstructure that can be compared with the simulated CH structures presented in this dissertation is a dendritic mixture of Al-Cu alloys [96]. In general, the morphologies of dendrites are more complex than that of bicontinuous

structures because dendrites possess features with multiple length scales. Yet, the evolution of Al-Cu alloys and the simulated systems presented in Chapter V are both driven by long-range diffusion and have isotropic interfacial energies. Thus, it will be interesting to examine the correlations between the interfacial velocity and morphological characteristics for the dendritic mixtures and compare them with those of the simpler CH structures. Furthermore, it has been found that, similarly to the CH structures, the normal velocities of interfaces with the same principal curvatures in Al-Cu alloy also have a Gaussian distribution [135]. This is remarkable since dendrites and bicontinuous structures undergo fundamentally different type of evolution. The origin of the Gaussian distribution is still not clear and requires further investigation.

Although the CH structures and the dendritic mixtures of Al-Cu alloy have some general similarities in kinetics, the solid-liquid dendritic mixtures possess unequal mobility between the two-phases while the CH structures possess equal mobility. For a better comparison with dendritic microstructures of the Al-Cu alloy, a bicontinuous structure with unequal mobility in the two phases should be compared. The unequal mobility can be modeled with the concentration dependent mobility term, as described above.

Coarsening of simulated microstructure with the anisotropy in the interfacial energy can be compared with metallic alloys, such as Al-Si and Al-Ge, that also possess interfacial energies that are highly anisotropic [136, 137]. Many of the microstructures of metallic alloys with anisotropic interfacial energies often exhibit faceted surfaces [137, 138]. Building upon the work described in this dissertation, the correlations between static and dynamic interfacial quantities and the surface normal can be investigated, in addition to other interfacial quantities. Since the anisotropic interfacial energy introduces additional complexity to the kinetics of coarsening, it is likely that the semi-analytical model and the continuity equation presented here must be modified. However, the work presented in this dissertation provides a clear path toward

the understanding of coarsening of complex microstructures, such as dendritic and anisotropic microstructures.

APPENDICES

APPENDIX A

Expressions for Curvatures and Normal Velocity Presented in Chapter III

A.1 Level-Set Formulation of Curvatures and Normal Velocity

As discussed in Section 3.2.3, the following section describes the numerical schemes employed to calculate the mean and Gaussian curvatures and the interfacial velocity using the level-set approach. The two common mathematical descriptions of the curvatures of surfaces are the mean and the Gaussian curvatures, denoted by H and K, respectively. The analytical equation for the mean curvature in terms of the normal to the surface is

$$H = \frac{1}{2}(\nabla \cdot \boldsymbol{n}), \tag{A.1}$$

where $\boldsymbol{n}$ is the unit normal vector [116]. The Gaussian curvature can also be expressed in terms of the unit normal vector as

$$K = \boldsymbol{n} \cdot \mathrm{adj}(He(\varphi^D))\boldsymbol{n}, \tag{A.2}$$

where $He(\varphi^D)$ is the 3×3 Hessian matrix of the second derivative of the smoothed level-set function, and adj$(He(\varphi^D))$ is the adjoint of the Hessian matrix [116]. In the level-set approach, the unit normal vector in Eqs. (A.1) & (A.2) can be written in terms of the smoothed level-set function as

$$\boldsymbol{n} = \frac{\nabla \varphi^D}{|\nabla \varphi^D|}. \tag{A.3}$$

By substituting Eq. (A.3) into Eqs. (A.1) & (A.2), the mean and the Gaussian curvature can be calculated by taking the spatial derivatives of φ^D,

$$\begin{aligned} H =& \frac{1}{2({\varphi^D}_x^2 + {\varphi^D}_y^2 + {\varphi^D}_z^2)^{3/2}} \Big\{ {\varphi^D}_x^2({\varphi^D}_{yy} + {\varphi^D}_{zz}) + {\varphi^D}_y^2({\varphi^D}_{xx} + {\varphi^D}_{zz}) + \\ & {\varphi^D}_z^2({\varphi^D}_{xx} + {\varphi^D}_{yy}) - 2({\varphi^D}_x{\varphi^D}_y{\varphi^D}_{xy} + {\varphi^D}_y{\varphi^D}_z{\varphi^D}_{yz} + {\varphi^D}_x{\varphi^D}_z{\varphi^D}_{xz}) \Big\}, \end{aligned} \tag{A.4}$$

$$\begin{aligned} K =& \frac{1}{\left({\varphi^D}_x^2 + {\varphi^D}_y^2 + {\varphi^D}_z^2\right)^2} \Big\{ {\varphi^D}_x^2({\varphi^D}_{yy}{\varphi^D}_{zz} - {\varphi^D}_{yz}^2) + {\varphi^D}_y^2({\varphi^D}_{xx}{\varphi^D}_{zz} - {\varphi^D}_{xz}^2) \\ & {\varphi^D}_z^2({\varphi^D}_{xx}{\varphi^D}_{yy} - {\varphi^D}_{xy}^2) + 2\left[{\varphi^D}_x{\varphi^D}_y\left({\varphi^D}_{xz}{\varphi^D}_{yz} - {\varphi^D}_{xy}{\varphi^D}_{zz}\right)\right. \\ & \left. + {\varphi^D}_y{\varphi^D}_z\left({\varphi^D}_{xy}{\varphi^D}_{xz} - {\varphi^D}_{yz}{\varphi^D}_{xx}\right) + {\varphi^D}_x{\varphi^D}_z\left({\varphi^D}_{xy}{\varphi^D}_{yz} - {\varphi^D}_{xz}{\varphi^D}_{yy}\right)\right] \Big\} \end{aligned} \tag{A.5}$$

where the subscripts of φ^D denote the spatial derivatives in their respective directions [116].

The first and second derivatives of the smoothed level-set function shown in Eqs. (A.4) & (A.5) are calculated with the central differencing scheme. For example, the numerical stencils for the spatial derivatives along the x-direction is defined as

$$\varphi_x^D = \frac{\varphi_{i+1,j,k}^D - \varphi_{i-1,j,k}^D}{2\Delta x} \tag{A.6}$$

$$\varphi^D_{xx} = \frac{-\varphi^D_{i+2,j,k} + 16\varphi^D_{i+1,j,k} - 30\varphi^D_{i,j,k} + 16\varphi^D_{i-1,j,k} - \varphi^D_{i-2,j,k}}{12\Delta x^2} \tag{A.7}$$

where i, j, and k denote the indices for x, y, and z positions, respectively. The first derivative is second-order accurate, and the second derivative is fourth-order accurate. The mixed partial derivative stencil is

$$\begin{aligned}\varphi^D_{xy} = \frac{1}{144\Delta x\Delta y}[\quad & \varphi^D_{i+2,j+2,k} - 8\varphi^D_{i+2,j+1,k} + 8\varphi^D_{i+2,j-1,k} - \varphi^D_{i+2,j-2,k} \\ & -8\varphi^D_{i+1,j+2,k} + 64\varphi^D_{i+1,j+1,k} - 64\varphi^D_{i+1,j-1,k} + 8\varphi^D_{i+1,j-2,k} \\ & +8\varphi^D_{i-1,j+2,k} - 64\varphi^D_{i-1,j+1,k} + 64\varphi^D_{i-1,j-1,k} - 8\varphi^D_{i-1,j-2,k} \\ & -\varphi^D_{i-2,j+2,k} + 8\varphi^D_{i-2,j+1,k} - 8\varphi^D_{i-2,j-1,k} + \varphi^D_{i-2,j-2,k}],\end{aligned} \tag{A.8}$$

which is also fourth-order accurate [123]. The use of higher-order schemes can reduce the grid anisotropy effect.

The normal velocity, v, can be determined by [116]

$$v = -\frac{\partial\varphi^D}{\partial t} \Big/ \left|\nabla\varphi^D\right|, \tag{A.9}$$

where the time derivative can be discretized as

$$\frac{\partial\varphi^D_{ijk}(t_1)}{\partial t} = \frac{\varphi^D_{ijk}(t_2) - \varphi^D_{ijk}(t_1)}{\Delta t}. \tag{A.10}$$

Here, $\varphi^D(t_i)$ represents the smoothed level-set function for the microstructure at time t_i and $\Delta t = t_2 - t_1$. The denominator of Eq. (A.9) is evaluated at t_1; i.e., $|\nabla\varphi^D(t_1)|$. It is important to note that the discretization incurs a first order error, which is proportional to Δt.

APPENDIX B

Fit parameters Presented in Chapter V

B.1 Fit parameters for $\langle v \rangle_H$ and $\langle v \rangle_{\Delta_S H}$ in Section 5.4.1

The parameters for the cubic polynomial fit in the form of

$$\langle v \rangle_\alpha = c_{\alpha 0} + c_{\alpha 1}\alpha + c_{\alpha 2}\alpha^2 + c_{\alpha 3}\alpha^3 \tag{B.1}$$

where $\alpha = H$ or $\alpha = \Delta_S H$, to the plot of $\langle v \rangle_H$ and $\langle v \rangle_{\Delta_S H}$ in Fig. 5.2(a.2)-(c.3) and (a.3)-(c.3) for the three CH structures are presented in Table B.1.

Structure	Type of Fit	$c_{\alpha 0}$	$c_{\alpha 1}$	$c_{\alpha 2}$	$c_{\alpha 3}$
50:50 CH Structure	$\langle v \rangle_H$	0.02	4.67	-0.05	0.74
	$\langle v \rangle_{\Delta_S H}$	0.00	1.54	0.00	-0.03
40:60 CH Structure	$\langle v \rangle_H$	-1.17	3.99	-0.33	0.61
	$\langle v \rangle_{\Delta_S H}$	-0.01	1.29	0.01	-0.02
30:70 CH Structure	$\langle v \rangle_H$	-2.03	2.83	-1.31	0.49
	$\langle v \rangle_{\Delta_S H}$	-0.05	0.61	0.01	0.00

Table B.1: The parameters of the cubic polynomial fit of the plots and for the three CH structures.

		Fit Parameters for $\langle v \rangle_{H,d}$			
Structure	Coefficients of the Quadratic Fit (i)	a_{i0}	a_{i1}	a_{i2}	a_{i3}
50:50 CH Structure	0	0.17	−2.87	−0.32	−3.44
	1	−0.02	−1.28	0.43	5.19
	2	0.00	0.06	−0.14	−1.72
40:60 CH Structure	0	−0.81	−3.10	−1.47	−0.28
	1	−0.09	−0.28	1.37	−0.28
	2	−0.05	−0.19	−0.31	0.30
30:70 CH Structure	0	−1.51	0.31	7.81	7.71
	1	−0.25	−3.74	−14.0	−12.8
	2	−0.01	1.32	5.38	4.81

Table B.2: The parameters of the cubic polynomial fit of the plot $\langle v \rangle_{H,d}$ for the three CH structures.

B.2 Fit parameters for $\langle v \rangle_{H,d}$ and $\langle \Delta_S v \rangle_{H,d}$ in Section 5.4.4

The parameters for the cubic polynomial fit in the form of Eq. (5.10) of the coefficients of the quadratic fit to $\langle v \rangle_{H,d}$ and $\langle \Delta_S v \rangle_{H,d}$ are presented in Table B.2 and B.3, respectively. The parameters a_{i0}, a_{i1}, a_{i2}, and a_{i3} are for $\langle v \rangle_{H,d}$ while the parameters b_{i0}, b_{i1}, b_{i2}, and b_{i3} are for $\langle \Delta_S v \rangle_{H,d}$, where $i = 0$, 1 and 2 indicate the powers of d in the quadratic fit of $\langle v \rangle_{H,d}$ and $\langle \Delta_S v \rangle_{H,d}$.

		Fit Parameters for $\langle \Delta_S v \rangle_{H,d}$			
Structure	Coefficients of the Quadratic Fit (i)	b_{i0}	b_{i1}	b_{i2}	b_{i3}
50:50 CH Structure	0	-0.16	3.62	3.86	57.9
	1	0.15	-7.78	-5.78	-72.1
	2	-0.02	12.7	1.88	15.6
40:60 CH Structure	0	2.09	11.2	25.0	15.3
	1	-3.67	-17.3	-29.8	-7.14
	2	-3.51	14.1	6.94	-5.03
30:70 CH Structure	0	3.25	-16.5	-81.5	-77.6
	1	-2.96	36.0	153.8	138.3
	2	4.06	-12.8	-67.3	-58.6

Table B.3: The parameters of the cubic polynomial fit of the plot $\langle \Delta_S v \rangle_{H,d}$ for the three CH structures.

BIBLIOGRAPHY

BIBLIOGRAPHY

[1] A. J. Ardell and R. B. Nicholson. Coarsening of γ' in Ni-Al Alloys. *J. Phys. Chem. Solids*, 27(11-1):1793–1804, Nov 1966.

[2] T. Z. Kattamis, J. C. Coughlin, and M. C. Flemings. Influence of coarsening on dendrite arm spacing of aluminum-copper alloys. *Trans. TMS-AIME*, 239(10):1504–1511, 1967.

[3] H. A. Calderon, P. W. Voorhees, J. L. Murray, and G Kostorz. Ostwald ripening in concentrated alloys. *Acta Metall. Mater.*, 42(3):991–1000, Mar 1994.

[4] T.M. Pollock and A.S. Argon. Directional coarsening in nickel-base single crystals with high volume fractions of coherent precipitates. *Acta Metall. Mater.*, 42(6):1859–1874, Jun 1994.

[5] C. J. Kuehmann and P. W. Voorhees. Ostwald ripening in ternary alloys. *Metall. Mater. Trans. A*, 27(4):937–943, Apr 1996.

[6] D. Kammer and P. W. Voorhees. The morphological evolution of dendritic microstructures during coarsening. *Acta Mater.*, 54(6):1549–1558, Apr 2006.

[7] T. Philippe and P. W. Voorhees. Ostwald ripening in multicomponent alloys. *Acta Mater.*, 61(11):4237–4244, Jun 2013.

[8] P. Wiltzius and A. Cumming. Domain growth and wetting in polymer mixtures. *Phys. Rev. Lett.*, 66(23):3000–3003, Jun 1991.

[9] T. Hashimoto, M. Takenaka, and T. Izumitani. Spontaneous pinning of domain growth during spinodal decomposition of off-critical polymer mixtures. *J. Chem. Phys.*, 97(1):679–689, Jul 1992.

[10] G. Krausch, C. A. Dai, E. J. Kramer, J. F. Marko, and F. S. Bates. Interference of spinodal waves in thin polymer films. *Macromolecules (Washington, DC, U. S.)*, 26(21):5566–5571, Oct 1993.

[11] S.-W. Song and J. M. Torkelson. Coarsening effects on microstructure formation in isopycnic polymer solutions and membranes produced via thermally induced phase separation. *Macromolecules (Washington, DC, U. S.)*, 27(22):6389–6397, Oct 1994.

[12] H. Wang and R. J. Composto. Thin film polymer blends undergoing phase separation and wetting: Identification of early, intermediate, and late stages. *J. Chem. Phys.*, 113(22):10386–10397, Dec 2000.

[13] K. B. Glasner and T. P. Witelski. Coarsening dynamics of dewetting films. *Phys. Rev. E*, 67(1, 2), Jan 2003.

[14] J. Kim, M. K. Gray, H. Y. Zhou, S. T. Nguyen, and J. M. Torkelson. Polymer blend compatibilization by gradient copolymer addition during melt processing: Stabilization of dispersed phase to static coarsening. *Macromolecules (Washington, DC, U. S.)*, 38(4):1037–1040, Feb 2005.

[15] F. M. Ross, J. Tersoff, and R. M. Tromp. Coarsening of self-assembled Ge quantum dots on Si(001). *Phys. Rev. Lett.*, 80(5):984–987, Feb 1998.

[16] O. Kienzle, F. Ernst, M. Ruhle, O. G. Schmidt, and K. Eberl. Germanium "quantum dots" embedded in silicon: Quantitative study of self-alignment and coarsening. *Appl. Phys. Lett.*, 74(2):269–271, Jan 1999.

[17] F. Liu, A. H. Li, and M. G. Lagally. Self-assembly of two-dimensional islands via strain-mediated coarsening. *Phys. Rev. E*, 87(12), Sep 2001.

[18] P. Liu, Y. W. Zhang, and C. Lu. Coarsening kinetics of heteroepitaxial islands in nucleationless Stranski-Krastanov growth. *Phys. Rev. B*, 68(3), Jul 2003.

[19] Y. Tu and J. Tersoff. Coarsening, mixing, and motion: The complex evolution of epitaxial islands. *Phys. Rev. E*, 98(9), Mar 2007.

[20] Ch. Heyn, A. Stemmann, A. Schramm, H. Welsch, W. Hansen, and Á. Nemcsics. Regimes of GaAs quantum dot self-assembly by droplet epitaxy. *Phys. Rev. B*, 76(7), Aug 2007.

[21] R. W. Balluffi, S. Allen, and W. C. Carter. *Kinetics of Materials*. John Wiley & Sons, 2005.

[22] K. P. Young and D. H. Kerkwood. The dendrite arm spacings of aluminum-copper alloys solidified under steady-state conditions. *Metall. Trans. A*, 6(1):197–205, Jan 1975.

[23] D. G. McCartney and J. D. Hunt. Measurements of cell and primary dendrite arm spacings in directionally solidified aluminium alloys. *Acta Metall.*, 29(11):1851–1863, Nov 1981.

[24] J. Alkemper, R. Mendoza, and P. W. Voorhees. Morphological evolution of dendritic microstructures. *Adv. Eng. Mater.*, 4(9):694–697, Sep 2002.

[25] R. Mendoza, I. Savin, K. Thornton, and P. W. Voorhees. Topological complexity and the dynamics of coarsening. *Nat. Mater.*, 3(6):385–388, Jun 2004.

[26] J. L. Fife and P. W. Voorhees. The morphological evolution of equiaxed dendritic microstructures during coarsening. *Acta Mater.*, 57(8):2418–2428, May 2009.

[27] W. R. Osorio, P. R. Goulart, A. Garcia, G. A. Santos, and C. M. Neto. Effect of dendritic arm spacing on mechanical properties and corrosion resistance of al 9 wt pct si and zn 27 wt pct al alloys. *Metall. Mater. Trans. A*, 37(8):2525–2538, Aug 2006.

[28] P. R. Goulart, W. R. Osório, J. E. Spinelli, and A. Garcia. Dendritic microstructure affecting mechanical properties and corrosion resistance of an Al-9 wt% Si alloy. *Mater. Manuf. Processes*, 22(3):328–332, Jan 2007.

[29] P. Tanasini, M. Cannarozzo, P. Costamagna, A. Faes, J. Van Herle, A. Hessler-Wyser, and C. Comninellis. Experimental and theoretical investigation of degradation mechanisms by particle coarsening in sofc electrodes. *Fuel Cells*, 9(5):740–752, Jan 2009.

[30] H.-Y. Chen, H.-C. Yu, J. S. Cronin, J. R. Wilson, S. A. Barnett, and K. Thornton. Simulation of coarsening in three-phase solid oxide fuel cell anodes. *J. Power Sources*, 196(3):1333–1337, Feb 2011.

[31] R. Davis, F. Abdeljawad, J. Lillibridge, and M. Haataja. Phase wettability and microstructural evolution in solid oxide fuel cell anode materials. *Acta Mater.*, 78:271–281, Oct 2014.

[32] L. Ratke and P. W. Voorhees. *Growth and coarsening: Ostwald ripening in material processing*. Springer, Berlin, 2002.

[33] D. A. Porter and K. E. Easterling. *Phase transformations in metals and alloys*. CRC Press, Boca Raton, FL, 3rd edition, 2009.

[34] V. A. Snyder, J. Alkemper, and P. W. Voorhees. The development of spatial correlations during Ostwald ripening: A test of theory. *Acta Mater.*, 48(10):2689–2701, Jun 2000.

[35] I. M. Liftshitz and V. V. Slyozov. The kinetics of precipitation from supersaturated solid solutions. *J. Phys. Chem. Solids*, 19(1-2):35–50, Jan 1961.

[36] C. Wagner. Theorie der alterung von niederschlägen durch umlösen (ostwald-reifung). *Zeitschrift für Elektrochemie*, 65(7-8), Sep 1961.

[37] T. F. Bower, H. D. Brody, and M. C. Flemings. Measurements of solute redistribution in dendritic solidification. *Trans. Metall. Soc. AIME*, 236(5):624–628, May 1966.

[38] H. Jinnai, Y. Nishikawa, T. Koga, and T. Hashimoto. Direct observation of three-dimensional bicontinuous structure developed via spinodal decomposition. *Macromolecules (Washington, DC, U. S.)*, 28(13):4782–4784, Jun 1995.

[39] H. Jinnai, Y. Nishikawa, H. Morimoto, T. Koga, and T. Hashimoto. Geometrical properties and interface dynamics: Time evolution of spinodal interface in a binary polymer mixture at the critical composition. *Langmuir*, 16(9):4380–4393, May 2000.

[40] Y. Kwon. *Morphology and topology of interfaces during coarsening via nonconserved and conserved dynamics*. PhD thesis, Northwestern University, 2007.

[41] R. Mendoza, J. Alkemper, and P. W. Voorhees. The morphological evolution of dendritic microstructures during coarsening. *Metall. Mater. Trans. A*, 34(3):481–489, Mar 2003.

[42] Y. Kwon, K. Thornton, and P. W. Voorhees. Morphology and topology in coarsening of domains via non-conserved and conserved dynamics. *Philos. Mag.*, 90(1-4):317–335, Jan 2010.

[43] J. L. Fife, J. W. Gibbs, E. Gulsoy, C.-L. Park, K. Thornton, and P. W. Voorhees. The dynamics of interfaces during coarsening in solid–liquid systems. *Acta Mater.*, 70:66–78, May 2014.

[44] C.-L. Park, P. W. Voorhees, and K. Thornton. Evolution of interfacial curvatures of a bicontinuous structure generated via nonconserved dynamics. *Acta Mater.*, 90:182–193, Jan 2015.

[45] P. W. Voorhees. Ostwald ripening of 2-phase mixtures. *Annu. Rev. Mater. Sci.*, 22:197–215, Aug 1992.

[46] P. W. Voorhees and R. J. Schaefer. In-situ observation of particle motion and diffusion interactions during coarsening. *Acta Metall.*, 35(2):327–339, Feb 1987.

[47] S. C. Hardy and P. W. Voorhees. Ostwald ripening in a system with a high volume fraction of coarsening phase. *Metall. Mater. Trans. A*, 19(11):2713–2721, Nov 1988.

[48] P. W. Voorhees, G. B. McFadden, R. F. Boisvert, and D. I. Meiron. Numerical-simulation of morphological development during Ostwald ripening. *Acta Metall.*, 36(1):207–222, Jan 1988.

[49] A. D. Brailsford and P. Wynblatt. The dependence of Ostwald ripening kinetics on particle volume fraction. *Acta Metall.*, 27(3):489–497, Mar 1979.

[50] J. A. Marqusee and J. Ross. Theory of Ostwald ripening - competitive growth and its dependence on volume fraction. *J. Chem. Phys.*, 80(1):536–543, Jan 1984.

[51] P. W. Voorhees and M. E. Glicksman. Solution to the multi-particle diffusion problem with applications to Ostwald ripening—II. Computer simulations. *Acta Metall.*, 32(11):2013–2030, Nov 1984.

[52] M. Marder. Correlations and Ostwald ripening. *Phys. Rev. A*, 36(2):858, Jul 1987.

[53] Y. Enomoto, K. Kawasaki, and M. Tokuyama. Computer modeling of Ostwald ripening. *Acta Metall.*, 35(4):907–913, Apr 1987.

[54] J. A. Horwath and L. F. Mondolfo. Dendritic growth. *Acta Metall.*, 10(11):1037–1042, Nov 1962.

[55] M. Kahlweit. On ageing of dendrites. *Scripta Metall.*, 2(5):251–254, May 1968.

[56] A. A. Chernov. *Kristallografiya*, 1(5):583–587, 1956.

[57] J. J. Reeves and T. Z. Kattamis. Model for isothermal dendritic coarsening. *Scripta Metall.*, 5(3):223–229, Jan 1971.

[58] A. Papapetrou. Untersuchungen über dendritisches Wachstum von Kristallen. *Zeitschrift Fur Kristallographie*, 92(1/2):89–129, Oct 1935.

[59] S. C. Huang and M. E. Glicksman. Fundamentals of dendritic solidification .2. Development of sidebranch structure. *Acta Metall.*, 29(5):717–734, May 1981.

[60] S. P. Marsh and M. E. Glicksman. Overview of geometric effects on coarsening of mushy zones. *Metall. Mater. Trans. A*, 27(3):557–567, Mar 1996.

[61] M. Fialkowski and R. Holyst. Morphological changes during the order-disorder transition in the two- and three-dimensional systems of scalar nonconserved order parameters. *Phys. Rev. E*, 66:046121, Oct 2002.

[62] O. Hellwig, A. Berger, and E. E. Fullerton. Domain walls in antiferromagnetically coupled multilayer films. *Phys. Rev. Lett.*, 91(19):197203, Nov 2003.

[63] O. Gutfleisch, K.-H. Müller, K. Khlopkov, M. Wolf, A. Yan, R. Schafer, T. Gemming, and L. Schultz. Evolution of magnetic domain structures and coercivity in high-performance SmCo 2:17-type permanent magnets. *Acta Mater.*, 54(4):997–1008, Feb 2006.

[64] J. Erlebacher and K. Sieradzki. Pattern formation during dealloying. *Scr. Mater.*, 49(10):991–996, Nov 2003.

[65] C.-Y. Kuo, S.-L. Su, H.-A. Tsai, Y.-S. Su, D.-M. Wang, and J.-Y. Lai. Formation and evolution of a bicontinuous structure of PMMA membrane during wet immersion process. *J. Membr. Sci.*, 315(1-2):187–194, May 2008.

[66] V. Z. H. Chan, J. Hoffman, V. Y. Lee, H. Iatrou, A. Avgeropoulos, N. Hadjichristidis, R. D. Miller, and E. L. Thomas. Ordered bicontinuous nanoporous and nanorelief ceramic films from self assembling polymer precursors. *Science*, 286(5445):1716–1719, Nov 1999.

[67] Y. F. Shi, Y. Meng, D. H. Chen, S. J. Cheng, P. Chen, T. F. Yang, Y. Wan, and D. Y. Zhao. Highly ordered mesoporous silicon carbide ceramics with large surface areas and high stability. *Adv. Funct. Mater.*, 16(4):561–567, Mar 3 2006.

[68] Y. C. Chou and W. I. Goldburg. Phase separation and coalescence in critically quenched isobutyric-aicd-water and 2,6-lutidine-water mixtures. *Phys. Rev. A*, 20(5):2105–2113, Nov 1979.

[69] A. Cumming, P. Wiltzius, F. S. Bates, and J. H. Rosedale. Light-scattering experiments on phase-separation dynamics in binary fluid mixtures. *Phys. Rev. A*, 45(2):885–897, Jan 15 1992.

[70] A. K. Khandpur, S. Forster, F. S. Bates, I. W. Hamley, A. J. Ryan, W. Bras, K. Almdal, and K. Mortensen. Polyisoprene-polystyrene diblock copolymer phase diagram near the order-disorder transition. *Macromolecules (Washington, DC, U. S.)*, 28(26):8796–8806, Dec 18 1995.

[71] H. Jinnai, T. Hashimoto, D. Lee, and S.-H. Chen. Morphological characterization of bicontinuous phase-separated polymer blends and one-phase microemulsions. *Macromolecules (Washington, DC, U. S.)*, 30(1):130–136, Jan 13 1997.

[72] Y. Kwon, K. Thornton, and P. W. Voorhees. Coarsening of bicontinuous structures via nonconserved and conserved dynamics. *Phys. Rev. E*, 75(2, 1):021120, Feb 2007.

[73] A. Genau and P. W. Voorhees. Spatial correlations in symmetric and asymmetric bicontinuous structures. *Acta Mater.*, 57:6226–6233, Jan 2009.

[74] L.-Q. Chen. Phase-field models for microstructure evolution. *Annu. Rev. Mater. Res.*, 32:130–140, Jan 2002.

[75] S. Yip. *Handbook of materials modeling*. Springer, Dordrecht, 2005.

[76] Y. Wang, Z.-K. Liu, and L.-Q. Chen. Thermodynamic properties of Al, Ni, NiAl, and Ni3Al from first-principles calculations. *Acta Mater.*, 52(9):2665 – 2671, May 2004.

[77] S.-L. Shang, B.-C. Zhou, W. Y. Wang, A. J. Ross, X. L. Liu, Y.-J. Hu, H.-Z. Fang, Y. W., and Z.-K. Liu. A comprehensive first-principles study of pure elements: Vacancy formation and migration energies and self-diffusion coefficients. *Acta Mater.*, 109:128–141, May 2016.

[78] G. Kresse and J. Furthmüller. Efficiency of ab-initio total energy calculations for metals and semiconductors using a plane-wave basis set. *Comput. Mat. Sci.*, 6(1):15 – 50, Jul 1996.

[79] J.J. Hoyt, M. Asta, and A. Karma. Atomistic and continuum modeling of dendritic solidification. *Mater. Sci. Eng., R*, 41(6):121 – 163, Sep 2003.

[80] P. Kollman. Free-energy calculations - applications to chemical and biochemical phenomena. *Chem. Rev. (Washington, DC, U. S.)*, 93(7):2395–2417, Nov 1993.

[81] A. Van der Ven, G. Ceder, M. Asta, and P. D. Tepesch. First-principles theory of ionic diffusion with nondilute carriers. *Phys. Rev. B*, 64(18), Nov 1 2001.

[82] C. P. Wang, X. Chen, X. J. Liu, F. S. Pan, and K. Ishida. Thermodynamic modeling of the Ce-Zn and Pr-Zn systems. *J. Alloys Compd.*, 458(1-2):166–173, Jun 30 2008.

[83] S. H. Zhou, Y. Wang, L.-Q. Chen, Z. K. Liu, and R. E. Napolitano. Solution-based thermodynamic modeling of the Ni-Al-Mo system using first-principles calculations. *CALPHAD: Comput. Coupling Phase Diagrams Thermochem.*, 46:124–133, Sep 2014.

[84] S. M. Allen and J. W. Cahn. Microscopic theory for antiphase boundary motion and its application to antiphase domain coarsening. *Acta Metall.*, 27(6):1085–1095, Jun 1979.

[85] J. W. Cahn and J. E. Hilliard. Free energy of a nonuniform system. I. interfacial free energy. *J. Chem. Phys.*, 28(2):258–267, Feb 1958.

[86] J. W. Cahn. On spinodal decomposition. *Acta Metall.*, 9(9):795–801, Sep 1961.

[87] C. Grossmann and H. Roos. *Numerical Treatment of Partial Differential Equations: Translated and revised by Martin Stynes*. Springer-Verlag Berlin Heidelberg, 2007.

[88] W. H. Press, B. P. Flannery, S. A. Teukolsky, and W. T. Vetterling. *Numerical recipes. The art of scientific computing (FORTRAN version)*. Cambridge University Press, 1990.

[89] E. A. Holm and P. M. Duxbury. Three-dimensional materials science. *Scr. Mater.*, 54(6):1035–1040, Mar 2006.

[90] G. Spanos. Foreword: Scripta Materialia viewpoint set on 3D characterization and analysis of materials. *Scr. Mater.*, 55(1):3, Jul 2006.

[91] K. Thornton and H. F. Poulsen. Three-dimensional materials science: An intersection of three-dimensional reconstructions and simulations. *MRS Bull.*, 33(6):587–595, Jun 2008.

[92] J. Alkemper and P. W. Voorhees. Quantitative serial sectioning analysis. *J. Microsc.*, 201:388–394, Jan 2001.

[93] D. Rowenhorst, A. Gupta, C. Feng, and G. Spanos. 3D crystallographic and morphological analysis of coarse martensite: combining EBSD and serial sectioning. *Scr. Mater.*, 55:11–16, Jan 2006.

[94] N. Limodin, L. Salvo, M. Suéry, and M. DiMichiel. In situ investigation by X-ray tomography of the overall and local microstructural changes occurring during partial remelting of an Al-15.8 wt.% Cu alloy. *Acta Mater.*, 55(9):3177–3191, May 2007.

[95] W. Ludwig, S. Schmidt, E. M. Lauridsen, and H. F. Poulsen. X-ray diffraction contrast tomography: a novel technique for three-dimensional grain mapping of polycrystals. I. Direct beam case. *J. Appl. Crystallogr.*, 41(2):302–309, Apr 2008.

[96] J. L. Fife and P. W. Voorhees. Self-similar microstructural evolution of dendritic solid-liquid mixtures during coarsening. *Scr. Mater.*, 60(10):839–842, May 2009.

[97] S. Terzi, L. Salvo, M. Suery, A. Dahle, and E. Boller. In situ microtomography investigation of microstructural evolution in Al-Cu alloys during holding in semi-solid state. *Trans. Nonferrous Met. Soc. China*, 20(3):S734–S738, Sep 2010.

[98] U. Lienert, S. Li, C. Hefferan, J. Lind, R. M. Suter, J. V. Bernier, N. R. Barton, M. C. Brandes, M. J. Mills, M. P. Miller, B. Jakobsen, and W. Pantleon. High-energy diffraction microscopy at the advanced photon source. *JOM*, 63(7):70–77, Jul 2011.

[99] J. R. Wilson, W. Kobsiriphat, R. Mendoza, H.-Y. Chen, J. M. Hiller, D. J. Miller, K. Thornton, P. W. Voorhees, S. B. Adler, and S. A. Barnett. Three-dimensional reconstruction of a solid-oxide fuel-cell anode. *Nat. Mater.*, 5(7):541–544, Jun 2006.

[100] J. R. Smith, A. Chen, D. Gostovic, D. Hickey, D. Kundinger, K. L. Duncan, R. T. DeHoff, K. S. Jones, and E. D. Wachsman. Evaluation of the relationship between cathode microstructure and electrochemical behavior for SOFCs. *Solid State Ionics*, 180:90–98, Jan 2009.

[101] S. J. Dillon and G. S. Rohrer. Characterization of the grain-boundary character and energy distributions of Yttria using automated serial sectioning and EBSD in the FIB. *J. Am. Ceram. Soc.*, 92(7):1580–1585, Jul 2009.

[102] J. R. Wilson, J. S. Cronin, S. A. Barnett, and S. J. Harris. Measurement of three-dimensional microstructure in a $LiCoO_2$ positive electrode. *J. Power Sources*, 196(7):3443–3447, Jan 2011.

[103] A. Karma and W. J. Rappel. Quantitative phase-field modeling of dendritic growth in two and three dimensions. *Phys. Rev. E*, 57(4):4323–4349, Jan 1998.

[104] L. K Aagesen, J. L Fife, E. M. Lauridsen, and P. W. Voorhees. The evolution of interfacial morphology during coarsening: A comparison between 4d experiments and phase-field simulations. *Scr. Mater.*, 64(5):394–397, Jan 2011.

[105] G. Russo and P. Smereka. A level-set method for the evolution of faceted crystals. *SIAM J. Sci. Comput.*, 21(6):2073–2095, Jun 2000.

[106] Y. Xiang, L.-T. Cheng, D. J. Srolovitz, and W. E. A level set method for dislocation dynamics. *Acta Mater.*, 51(18):5499–5518, Oct 2003.

[107] L. Tan and N. Zabaras. A level set simulation of dendritic solidification of multi-component alloys. *J. Comput. Phys.*, 221(1):9–40, Jan 2007.

[108] M. Zhihong, C. Guo, M. Yanzhao, and K. Lee. Curvature estimation for meshes based on vertex normal triangles. *Computer-Aided Design*, 43(12):1561–1566, Dec 2011.

[109] B Hamann. Curvature approximation for triangulated surfaces. In G. Farin, H. Noltemeier, H. Hagen, and W. Knödel, editors, *Geometric Modelling*, volume 8 of *Computing Supplementum*, pages 139–153. Springer Vienna, Vienna, Austria, Jan 1993.

[110] J. Goldfeather and V. Interrante. A novel cubic-order algorithm for approximating principal direction vectors. *ACM Transactions on Graphics*, 23(1):45–63, Jan 2004.

[111] E. Magid, O. Soldea, and E. Rivlin. A comparison of Gaussian and mean curvature estimation methods on triangular meshes of range image data. *Computer Vision and Image Understanding*, 107(3):139–159, Sep 2007.

[112] D. S. Meek and D. J. Walton. On surface normal and Gaussian curvature approximations given data sampled from a smooth surface. *Computer Aided Geometric Design*, 17(6):521–543, Jul 2000.

[113] N. Meyer, M. Desbrun, P. Schroder, and A. H. Barr. Discrete differential-geometry operators for triangulated 2-manifolds. In Hege, H. C. and Polthier, K, editor, *Visualization and Mathematics III*, pages 35–57, Berlin, Germany, 2003. Springer-Verlag Berlin.

[114] X. Chen and F. Schmitt. Intrinsic surface properties from surface triangulation. In Sandini, G, editor, *Computer Vision — ECCV'92*, volume 588 of *Lecture Notes in Computer Science*, pages 739–743, Berlin, Germany, 1992. Springer Berlin Heidelberg.

[115] K. Watanabe and A. G. Belyaev. Detection of salient curvature features on polygonal surfaces. *Computer Graphics Forum*, 20(3):C385–C392, 2001.

[116] J. A. Sethian. *Level Set Methods and Fast Marching Methods: Evolving Interfaces in Computational Geometry, Fluid Mechanics, Computer Vision, and Materials Science.* Cambridge University Press, Cambridge, UK, second edition, 1999.

[117] S. Osher and J. A. Sethian. Fronts propagating with curvature-dependent speed: algorithms based on hamilton-jacobi formulations. *J. Comput. Phys.*, 79:12–49, Nov 1988.

[118] J. W. Bullard, E. J. Garboczi, W. C. Carter, and E. R. Fuller Jr. Numerical methods for computing interfacial mean curvature. *Comput. Mat. Sci.*, 4(2):103–116, Jul 1995.

[119] O. I. Frette, G. Virnovsky, and D. Silin. Estimation of the curvature of an interface from a digital 2D image. *Comput. Mat. Sci.*, 44(3):867–875, Jan 2009.

[120] Y.-T. Kim, N. Goldenfeld, and J. Dantzig. Computation of dendritic microstructures using a level set method. *Phys. Rev. E*, 62(2, B):2471–2474, Aug 2000.

[121] K. A. Smith, F. J. Solis, L. Tao, K. Thornton, and M. O. de la Cruz. Domain growth in ternary fluids: A level set approach. *Phys. Rev. Lett.*, 84(1):91–94, Jan 2000.

[122] M. Sussman, P. Smereka, and S. Osher. A level set approach for computing solutions to incompressible two-phase flow. *J. Comput. Phys.*, 114(1):146–159, Sep 1994.

[123] L. K. Aagesen. *Phase-field simulation of solidification and coarsening in dendritic microstructures.* PhD thesis, Northwestern University, 2010.

[124] D. A. Drew. Evolution of geometric statistics. *SIAM J. Appl. Math.*, 50(3):649–666, JUN 1990.

[125] C. L. Park, P. W. Voorhees, and K. Thornton. Application of the level-set method to the analysis of an evolving microstructure. *Comput. Mat. Sci.*, 85:46–58, APR 1 2014.

[126] J. Xu and H. Zhao. An eulerian formulation for solving partial differential equations along a moving interface. *J. Sci. Comput*, 19(1-3):573–594, 2003.

[127] P. Grinfeld. Hamiltonian dynamic equations for fluid films. *Stud. Appl. Math.*, 125(3):223–264, 2010.

[128] J. Rubinstein and P. Sternberg. Nonlocal reaction-diffusion equations and nucleation. *J. Inst. Math. Its Appl.*, 48(3):249–264, 1992.

[129] D Sappelt and J Jäckle. Spinodal decomposition with formation of a glassy phase. *Europhysics Letters (EPL)*, 37:13–18, 2007.

[130] G. Sheng, T. Wang, Q. Du, K. G. Wang, Z. K. Liu, and L. Q. Chen. Coarsening kinetics of a two phase mixture with highly disparate diffusionmobility. *Communications in Computational Physics*, 8(2):249–264, 2010.

[131] J. J. Eggleston, G. B. McFadden, and P. W. Voorhees. A phase-field model for highly anisotropic interfacial energy. *Physica D*, 150(1-2):91–103, 2001.

[132] S. Wise, J. Kim, and J. Lowengrub. Solving the regularized, strongly anisotropic Cahn-Hilliard equation by an adaptive nonlinear multigrid method. *J. Comput. Phys.*, 226(1):414–446, Sep 2007.

[133] Wulff G. Zur frage dee geschwindigkeit des wachstums und der auflösung de krystallflächen. *Zeitschrift für Kristallographie und Mineralogie*, 34:449–530, 1901.

[134] F. Hausser and A. Voigt. Facet formation and coarsening modeled by a geometric evolution law for epitaxial growth. In *J. Cryst. Growth*, volume 275, 2005.

[135] J. W. Gibbs. *Interfacial Dynamics in Liquid-Solid Mixtures: A Study of Solidification and Coarsening.* PhD thesis, Northwestern University, 2014.

[136] K. Kaneko, K. Inoke, K. Sato, K. Kitawaki, H. Higashida, I. Arslan, and P.A. Midgley. TEM characterization of Ge precipitates in an Al–1.6 at% Ge alloy. *Ultramicroscopy*, 108(3):210 – 220, 2008. Proceedings of the Sixteenth International Microscopy Congress.

[137] A. J. Shahani, E. B. Gulsoy, V. J. Roussochatzakis, J. W. Gibbs, J. L. Fife, and P. W. Voorhees. The dynamics of coarsening in highly anisotropic systems: Si particles in Al-Si liquids. *Acta Mater.*, 97:325–337, Sep 2015.

[138] D. Chatain. Anisotropy of wetting. *Annu. Rev. Mater. Res.*, 38:45–70, 2008.